CHALMERS
UNIVERSITY OF TECHNOLOGY

Integrated Fast Battery Charger Using an Electrically Excited Synchronous Machine-Based Drive System

Master's thesis in Sustainable Electric Power Engineering and Electromobility

XINYU MA

DEPARTMENT OF ELECTRICAL ENGINEERING
CHALMERS UNIVERSITY OF TECHNOLOGY
Gothenburg, Sweden 2026
www.chalmers.se

MASTER'S THESIS 2026

Integrated Fast Battery Charger Using an Electrically Excited Synchronous Machine-Based Drive System

Xinyu Ma

Department of Electrical Engineering
Division of Sustainable Electric Power Engineering and Electromobility
CHALMERS UNIVERSITY OF TECHNOLOGY
Gothenburg, Sweden 2026

Integrated Fast Battery Charger Using an Electrically Excited Synchronous Machine-Based Drive System

Xinyu Ma

Supervisor: LUCA BOSCAGLIA, Sustainable electric power engineering and electromobility
Examiner: YUJING LIU, Sustainable electric power engineering and electromobility

Master's Thesis 2026
Department of Electrical Engineering
Division of Sustainable Electric Power Engineering and Electromobility

Chalmers University of Technology
SE-412 96 Gothenburg
Telephone +46 31 772 1000

Typeset in LaTeX
Printed by Chalmers Reproservice
Gothenburg, Sweden 2026

Integrated Fast Battery Charger Using an Electrically Excited Synchronous Machine-Based Drive System
XINYU MA
Department of Electrical Engineering
Chalmers University of Technology

Abstract

This thesis investigates an integrated off-board fast battery charging system utilizing an Electrically Excited Synchronous Machine (EESM)-based drive topology. The aim is to reuse the existing traction inverter and machine windings as part of a DC/DC boost converter, thereby reducing system cost, volume, and component redundancy. To achieve this goal, three levels of simulation were carried out. First, an excitation-based Finite Element Analysis (FEA) in ANSYS Maxwell was performed to determine losses and inductances of the EESM under various operating conditions. Second, a system-level co-simulation between Maxwell and ANSYS Simplorer/Simulink was conducted, in which the electromagnetic model of the machine interacted dynamically with the converter and control system. This enabled real-time calculation of inductances and losses under variations in both shift angle and rotor position.

Finally, a Simulink-based system simulation was carried out to analyze current ripple, torque generation, and efficiency across different frequencies. The results show that phase-shift modulation predominantly affects the current waveform and ripple behavior, while the magnetic coupling and inductance remain almost constant. Increasing the switching frequency reduces stator core losses but has minimal impact on copper losses. Overall, the proposed integrated EESM-based fast charger demonstrates high feasibility and efficiency. It achieves compact system integration, stable electromagnetic performance, and effective control of current ripple and core losses—offering a sustainable approach for future electric vehicle charging architectures.

Keywords: Electrically Excited Synchronous Machine (EESM); Integrated Charger; DC/DC Boost Converter; PWM Phase Shift; Co-simulation; Finite Element Analysis (FEA); Losses

Acknowledgements

I would like to begin by expressing my sincere gratitude to Prof. Yujing Liu, my examiner, for his insightful comments, constructive suggestions, and valuable time devoted to reviewing my thesis. His expertise and guidance have greatly improved the quality and depth of this work.

I would also like to extend my heartfelt thanks to my supervisor, Dr. Luca Boscaglia, for his continuous support, patient guidance, and encouragement throughout the research process. His knowledge, enthusiasm, and attention to detail have been a constant source of inspiration and learning.

I am equally grateful to all the professors and staff of the Sustainable Electric Power Engineering and Electromobility program for creating a supportive and stimulating academic environment.

Finally, I would like to thank my family and friends for their unwavering support, understanding, and encouragement, which have accompanied me through every step of this journey.

Xinyu Ma, Gothenburg, December 2025

Nomenclature

Below is the nomenclature of indices, sets, parameters, and variables that have been used throughout this thesis.

Glossary

AC	Alternating Current
DC	Direct Current
$EESM$	Electrically Excited Synchronous Machine
FEA	Finite Element Analysis
MMF	MagnetoMotive Force

Contents

List of Figures

List of Tables

1

Introduction

1.1 Background

In recent years, with the rapid development of the electric vehicle (EV) industry, the voltage platform of traction batteries has been continuously increasing. The 800 V high-voltage battery is gradually becoming a trend, aiming to achieve higher power density and shorter charging time[1]. However, most of the existing public DC fast-charging infrastructures are still based on 400 V systems, which creates a mismatch in voltage levels. As a result, an additional DC/DC converter is usually required to enable energy transfer from 400 V chargers to 800 V batteries.

Traditional solutions often rely on a separate DC/DC converter together with the on-board charger (OBC). This not only increases system cost and hardware volume but also reduces energy efficiency and space utilization of the vehicle. It is worth noting that the key components of a boost converter—inductors, power switches, and diodes—are already present in the traction inverter and motor system. This brings a new idea for building a highly integrated charging architecture, where the DC/DC function can be realized by reusing the inductance of the stator windings of an Electrically Excited Synchronous Machine (EESM) together with the semiconductor devices in the inverter, without adding extra power components. This solution can reduce cost and weight, improve compactness and efficiency, and has therefore attracted increasing attention in recent years[2].

However, reusing the motor and inverter as an integrated charger also introduces several challenges. First, the inductance of the EESM is strongly affected by current magnitude and core saturation, and its nonlinear characteristics may increase current ripple, which could reduce charging efficiency and shorten battery life. Second, strong electromagnetic coupling between the stator and rotor may generate additional torque and undesired rotor movement during charging, which could threaten system stability. In addition, different modulation and control strategies (such as the phase shift of PWM carriers) may have complex impacts on inductance, losses, and current ripple[3]. Therefore, it is of great theoretical and engineering significance to carry out systematic modeling and simulation to understand the mechanisms of such integrated systems.

Against this background, this thesis focuses on the integrated DC fast-charging architecture based on an EESM drive system. By combining Finite Element Method (FEM) electromagnetic simulations with system-level co-simulation, this work investigates the variation of inductance, the loss mechanism, and the influence of modulation strategies under different operating conditions, so as to provide theoretical support and optimization guidelines for the design of efficient and reliable integrated charging systems[4].

1.2 Scope

The scope of this work covers both electromagnetic modeling and system-level analysis of the integrated charging system. The main aspects include:

- **Inductance Estimation:** Evaluation of the inductance of the EESM under various operating conditions using Finite Element Method (FEM) simulations.
- **High-Frequency and High-Current Analysis:** Electromagnetic FEM simulations to assess machine performance in high-frequency and high-current applications, including iron and copper losses.
- **System-Level Simulation:** Co-simulation of the complete charging circuit (machine + converter + controller) to assess feasibility, with a particular focus on current ripple behavior.
- **Harmonic Losses and Modulation Strategies:** Investigation of the impact of modulation carrier phase shifting on harmonic losses and current ripple.

1.3 Limitations

The limitations of this study are as follows:

- Lack of Experimental Validation: The work mainly relies on FEM modeling and system-level simulations, without validation through hardware prototypes. The conclusions therefore need to be further confirmed by experiments in future research.
- Motor Type Restriction: The study is based on a specific topology of the Electrically Excited Synchronous Machine (EESM). The applicability of the results to other motor types, such as Permanent Magnet Synchronous Machines (PMSMs) or Induction Machines (IMs), requires further investigation.
- Limited Control Strategy: Only typical PWM carrier phase-shift strategies and PI control are studied in this thesis. More advanced control algorithms, such as Model Predictive Control or nonlinear control, are not covered.
- Thermal and Reliability Factors Not Considered: The research focuses on electromagnetic and circuit characteristics. Issues such as thermal management, long-term reliability, and safety of the motor and power devices are not deeply discussed.

2

Theory

2.1 Boost Converter

A boost converter is a common DC/DC topology used to step up the input voltage to a higher DC output voltage. Its basic components include an inductor L, a power switch (typically a MOSFET or IGBT), a diode, and an output filter capacitor C. By periodically storing energy in the inductor and releasing it to the load, the converter achieves voltage amplification[5].

2.1.1 Operating Principle

The operation of the boost converter can be divided into two main states within a switching period T_s:

1. Switch ON (Energy Storage Phase): When the switch is turned on, the input voltage source V_{in} is directly applied to the inductor L. The inductor current increases linearly according to

   $$\frac{di_L}{dt} = \frac{V_{in}}{L} \tag{2.1}$$

   During this interval, the diode is reverse-biased and the load is supplied by the output capacitor.
2. Switch OFF (Energy Transfer Phase): When the switch is turned off, the inductor releases its stored energy. The inductor current flows through the diode to the capacitor and load, increasing the output voltage. The inductor current decreases as

   $$\frac{di_L}{dt} = \frac{V_{\text{in}} - V_{\text{out}}}{L} \quad [6] \tag{2.2}$$

2.1.2 Voltage Conversion Ratio

In continuous conduction mode (CCM), the average voltage across the inductor over a switching period must be zero (volt-second balance). Applying this principle yields the ideal voltage conversion ratio:

$$V_{out} = \frac{V_{in}}{1 - D} \tag{2.3}$$

where D is the duty cycle defined as the fraction of the period for which the switch is ON. Since $0 < D < 1$, the output voltage is always greater than the input voltage.

In discontinuous conduction mode (DCM), where the inductor current falls to zero within a switching cycle, the conversion ratio depends on the load current and is more complex. Nevertheless, CCM is often preferred in high-power applications due to reduced current stress and lower ripple.

2.1.3 Inductor Current and Capacitor Voltage

The inductor current ripple is expressed as

$$\Delta I_L = \frac{V_{in} D}{L f_s} \tag{2.4}$$

where f_s is the switching frequency.
The output voltage ripple is mainly determined by the capacitor:

$$\Delta V_{out} = \frac{I_{out} D}{C f_s} \tag{2.5}$$

These relations highlight the importance of inductor and capacitor sizing in achieving stable operation[7].

2.1.4 Non-Idealities and Efficiency

In practice, parasitic resistances, diode forward voltage drop, and switching losses reduce the efficiency of the converter. The output voltage then becomes:

$$V_{out} = \frac{V_{in} - V_{sw} - D V_d}{1 - D} - I_{out} R_{loss} \tag{2.6}$$

where V_{sw} is the switch voltage drop, V_d is the diode forward voltage, and R_{loss} represents equivalent parasitic resistances[8].
Despite these losses, the boost converter remains one of the most widely used step-up topologies due to its simplicity, high efficiency, and suitability for renewable energy systems, electric vehicles, and portable electronics[9].

2.2 Electrically Excited Synchronous Machine (EESM)

An Electrically Excited Synchronous Machine (EESM) is a synchronous machine in which the rotor magnetic field is produced by a DC field winding, as opposed to permanent magnets or reluctance effects. The EESM provides operational flexibility in terms of power factor adjustment, torque production and field weakening due to its controllable excitation. This makes it suitable for a range of applications, including electric vehicles, wind turbines and industrial drives[10].

2.2.1 Operating Principle

The stator of an EESM is typically a three-phase winding supplied by an AC voltage source, while the rotor contains a DC-excited field winding. When the rotor field

is energized by a direct current, it produces a constant magnetic flux Φ_f. The stator windings generate a rotating magnetic field with synchronous speed ω_s, which interacts with the rotor flux to produce torque.
The synchronous speed is determined by the grid or inverter frequency f:

$$\omega_s = \frac{2\pi f}{p} \tag{2.7}$$

where p is the number of pole pairs.
To maintain synchronous operation, the rotor must rotate at the same angular velocity $\omega_r = \omega_s$[11].

2.2.2 Voltage Equations

For a three-phase EESM in the rotor-oriented dq reference frame, the stator voltage equations are expressed as:

$$v_d = R_s i_d - \omega_s L_q i_q + \frac{d\psi_d}{dt} \tag{2.8}$$

$$v_q = R_s i_q + \omega_s L_d i_d + \frac{d\psi_q}{dt} \tag{2.9}$$

where v_d, v_q are the dq-axis voltages, i_d, i_q are the dq-axis currents, L_d, L_q are the dq-axis inductances, and R_s is the stator resistance[12].
The flux linkages are given by:

$$\psi_d = L_d i_d + \psi_f \tag{2.10}$$

$$\psi_q = L_q i_q \tag{2.11}$$

where ψ_f is the rotor field flux linkage, proportional to the field current i_f[12].

2.2.3 Electromagnetic Torque

The electromagnetic torque is expressed as:

$$T_e = \frac{3}{2} p \left(\psi_d i_q - \psi_q i_d\right) \tag{2.12}$$

Substituting the flux linkage expressions, the torque equation becomes:

$$T_e = \frac{3}{2} p \left(\psi_f i_q + (L_d - L_q) i_d i_q\right) \tag{2.13}$$

This shows two contributions:

- A field excitation torque term ($\psi_f i_q$), dependent on the field flux and quadrature current.
- A reluctance torque term ($(L_d - L_q) i_d i_q$), significant in salient-pole machines[4, 13].

2.2.4 Power Factor and Field Control

One of the main advantages of the EESM is its controllable field current i_f, which directly influences ψ_f and therefore the air-gap flux. By adjusting i_f, the machine can operate at different power factors:

- Over-excited mode: Produces leading reactive power.
- Under-excited mode: Produces lagging reactive power.
- Unity power factor: Achieved when excitation matches load requirements[10].

This makes the EESM particularly useful

2.3 Harmonics

2.3.1 Harmonic Analysis

In power electronic converters and motor drive systems, harmonics are high-frequency components generated by the nonlinear characteristics of switching devices and PWM modulation techniques. Ideally, voltage and current would be pure sine waves. However, practical systems contain multiple high-frequency components due to the switching actions of inverters, carrier frequencies and modulation strategies. These high-frequency harmonics are the main reason for waveform distortion.

Harmonics are fundamentally generated by periodic discontinuous changes in voltage or current. Under PWM modulation, the periodic switching on and off of conductive devices causes the output voltage to exhibit pulsed variations. Although the average value approximates the goal voltage over one cycle, the spectrum still contains significant high-frequency components. When these harmonics enter the motor windings, they induce additional magnetic flux changes and extra losses[14].

2.3.2 Effects of Harmonics on Systems

Harmonics impact system performance in multiple ways:

Increased energy losses: High-frequency harmonic currents induce the skin effect in conductors, raising the equivalent resistance and increasing copper losses. Simultaneously, high-frequency magnetic flux variations in the iron core exacerbate eddy current and hysteresis losses.

Electromagnetic noise and vibration: Harmonic magnetic fields cause fluctuations in electromagnetic torque, inducing additional mechanical vibration and noise during motor operation.

Control and measurement errors: Harmonic interference may degrade the sampling accuracy of current sensors or control systems, compromising system stability.

Electromagnetic interference (EMI): High-frequency harmonics can easily couple with other circuits via wiring or radiation, causing electromagnetic compatibility issues.

Harmonics affect not only motor smoothness, but also directly alter loss distribution. For example, when the PWM shifting angle changes, interference between the carrier waves of adjacent phases redistributes harmonic energy. This results in fluctuations in the amplitude of the local magnetic fields within the stator and rotor, which affects iron losses and current ripple[15, 16].

2.4 Losses in a EESM

In the operation of electric machines and their integrated charging systems, losses play a decisive role in efficiency, thermal management, and reliability. According to their physical mechanisms, they are generally classified into three main categories: core losses, copper losses, and other losses. In this project, the analysis focuses on six specific types: Eddy Current Loss Rotor, Eddy Current Loss Stator, Core Loss Rotor, Core Loss Stator, Stranded Loss, and Solid Loss. The following sections explain them based on electromagnetic principles[17].

2.4.1 Core Losses

Core losses occur in the stator and rotor cores, mainly caused by alternating magnetic fields. They usually consist of hysteresis losses and eddy current losses. Under high-frequency PWM switching, the share of core losses in the total loss becomes significant, making them a key factor in evaluating integrated charging performance. A commonly used core-loss model is the Steinmetz equation:

$$P_{\text{core}} = k_h f B_{\max}^{\alpha} + k_e f^2 B_{\max}^2 \quad [18] \tag{2.14}$$

2.4.1.1 Core Loss – Rotor

The total core loss in the rotor, including both hysteresis and eddy currents. Due to the rotor's complex geometry and the variation of flux density with rotor angle and excitation current, losses are particularly high around pole shoes and bridges. Excessive rotor core loss may lead to extra heating and reduced efficiency during integrated charging[4].

2.4.1.2 Core Loss – Stator

The total stator core loss, which is often the dominant component in the overall losses. The tooth tips and yoke regions are the main flux paths, where alternating flux is most intense under high-frequency switching, leading to higher losses than in the rotor[4].

2.4.1.3 Hysteresis Loss

During alternating magnetization, the repeated reversal of magnetic domains consumes energy. This loss depends on the hysteresis loop area, operating frequency, and magnetic flux density. An approximation for hysteresis loss is:

$$P_{\text{hyst}} = k_h f B_{\max}^{\alpha} \tag{2.15}$$

It is directly related to material properties such as coercivity and hysteresis coefficient, and is usually dominant at lower frequencies[19].

2.4.1.4 Eddy Current Loss

Alternating magnetic flux induces circulating currents inside the conductive core, generating Joule heat. Eddy current losses are proportional to the flux variation rate and are strongly influenced by the electrical conductivity, lamination thickness, and frequency. For laminated sheets of thickness t, a classical eddy current model is:

$$P_{\text{eddy}} = k_e f^2 B_{\max}^2 = \frac{\pi^2 t^2}{6\rho} f^2 B_{\max}^2 \tag{2.16}$$

- **Eddy Current Loss – Rotor:** This separates the eddy current component from the total rotor core loss, highlighting additional losses caused by frequency and geometric effects. At high switching frequencies, rotor eddy current loss rises sharply and must be carefully considered in design. In regions approximated as solid steel, the loss follows:

  $$P_{\text{eddy,solid}} \propto \frac{B_{\max}^2}{\rho\,\delta} \tag{2.17}$$

  where $\delta = \sqrt{2\rho/(\mu\omega)}$ is the skin depth[20].
- **Eddy Current Loss – Stator:** Eddy current losses in the stator, concentrated in the teeth and yoke regions, contribute significantly to temperature rise and efficiency reduction. By comparing with the total stator core loss, the relative contribution of hysteresis and eddy currents can be identified more clearly[20].

2.4.2 Copper Losses

Copper losses mainly originate from the I^2R losses in the windings when current flows through the conductors. In integrated charging, the current contains not only a DC component but also high-frequency AC components. Therefore, copper losses can be divided into DC and AC parts[19].

2.4.2.1 DC Copper Loss

Produced by the winding resistance and the DC current component. Although not explicitly shown in the simulation results, it varies with the charging current magnitude and forms a stable background loss.

$$P_{\text{DC}} = I_{\text{DC}}^2 R_{\text{DC}} \quad [19] \tag{2.18}$$

2.4.2.2 AC Copper Loss

High-frequency currents cause skin effect (current crowding near the conductor surface, reducing effective cross-section) and proximity effect (magnetic coupling between adjacent conductors leading to uneven current distribution). These increase the effective resistance and generate additional losses. The AC resistance may be expressed as:

$$R_{\text{AC}} = R_{\text{DC}}\,(1 + Y_{\text{skin}} + Y_{\text{prox}}) \tag{2.19}$$

thus the AC loss becomes:

$$P_{\mathrm{AC}} = I_{\mathrm{AC}}^2 R_{\mathrm{AC}} \quad [21] \tag{2.20}$$

2.4.2.3 Stranded Loss

In the simulations, this output directly represents additional winding losses caused by AC effects. It reflects the impact of high-frequency PWM components on winding copper losses. Its magnitude depends on switching frequency, duty cycle, and current amplitude, making it an important indicator for evaluating different PWM strategies[21].

2.4.3 Other Losses

Apart from core and copper losses, there are additional losses caused by structural and parasitic effects in the motor and power electronics system[22].

2.4.3.1 Solid Loss

This occurs in non-laminated metallic parts, such as the shaft, solid rotor regions, busbars, or power module pins. Without laminated design to restrict eddy currents, these components can develop large circulating currents under alternating fields, leading to significant Joule heating. Solid eddy current losses follow:

$$P_{\mathrm{solid}} \propto \frac{B^2}{\rho\,\delta} \tag{2.21}$$

Solid losses are often localized, potentially creating hot spots that reduce efficiency and reliability[22].

2.4.4 Summary

In summary, the three categories of losses (core losses, copper losses, and other losses) form the fundamental basis for evaluating the efficiency of the integrated charging system. Their distribution and sensitivity to switching frequency, modulation strategies, and machine design parameters provide essential insights for improving thermal management, enhancing reliability, and optimizing the overall energy performance of the electric drive and charging process[17].

3

Modelling and simulation

The present study proposes a methodology for the systematic analysis of the effects of PWM carrier phase shift angle, rotor position, and switching frequency on the performance of electrically excited synchronous motors. To this end, a finite element model of the motor was established on the ANSYS Maxwell platform. A time-stepped transient simulation method was utilised in order to investigate variations in electromagnetic characteristics under different operating conditions[23].

The model incorporates the stator and rotor cores, excitation windings, and three-phase armature windings, with geometric dimensions and material parameters configured based on the actual structure. By varying the phase shift angle, rotor position, and frequency, the current waveforms, loss distributions, and inductance characteristics under different modulation strategies and operating states can be observed[24].

In all simulations, end effects and mechanical losses were neglected in order to highlight the impact of electromagnetic quantity variations. In order to enhance computational efficiency, the model solves only the 1/8 symmetrical portion of the motor. This ensures a significant reduction in simulation time while maintaining the same level of result accuracy[11].

This modelling and simulation workflow effectively reveals the relationship between modulation parameters and motor electromagnetic performance, providing theoretical support for subsequent system optimisation and improvement to control strategy[25].

3.1 Finite element analysis

The core analytical method employed in this study is Finite Element Analysis (FEA), utilised throughout the entire simulation system to precisely determine the magnetic field distribution and electromagnetic characteristics within the motor[11].

The finite element method is a numerical technique that is utilised to discretise the complex electromagnetic field region into a multitude of finite elements, thereby approximating the solution to Maxwell's equations within each element. This process consequently yields the spatial distribution results for magnetic flux density, current density, and losses[4].

In comparison with conventional analytical models, the finite element method (FEA) simultaneously accounts for material nonlinearity, geometric complexity, and time-varying excitation factors. This provides distinct advantages when investigating the impact of PWM shifting angle, rotor position, and switching frequency variations on electromagnetic performance[26].

3.2 Machine—Standalone Simulation

In order to accurately reproduce the electromagnetic response of the motor using this modulation strategy within a finite element environment, avoiding the computational overhead of complex switch modelling, this study employs expression-defined triangular wave current excitation. This approach allows ideal current sources to be applied directly in Maxwell without the need to establish control loops and power electronic switches, thus facilitating the investigation of steady-state magnetic fields and loss characteristics under different modulation conditions[27].

3.2.1 Current Waveform

Compared to the current variation patterns in actual PWM control, triangular wave currents exhibit similar linear rise and fall characteristics. This means they effectively reflect the flux variation trends induced by carrier modulation[28].

From a circuit mechanism perspective, phase-shifted PWM inverters cause the phase current to exhibit near-linear variation within a carrier cycle due to the conduction and switching of switching devices. The waveform corresponds to the processes of energy storage and release during the rising and falling phases, respectively[11]. Therefore, using an ideal triangular current for excitation can effectively simulate motor current dynamics under PWM drive in finite element analysis, eliminating the need for complex power electronic switch model construction[4].

Triangular wave currents offer the following advantages:

- Smooth waveform and computational stability: It gets rid of spike currents and high-frequency noise problems that come with PWM square wave excitation, which helps to get numerical convergence in finite element solutions.
- Ease of parametric control: Current characteristics can be conveniently scanned across different frequencies and phase angles by adjusting the frequency and amplitude of the waveform.
- Maintain periodic steady-state behaviour. The continuous differentiability of the triangular wave over time enables the analysis of steady-state losses, magnetic flux density variations and inductive characteristics[27].

In summary, selecting triangular wave current excitation preserves physical consistency with the actual PWM drive, ensuring the stability and accuracy of finite element simulations. This approach lays the foundation for subsequent investigations into the effects of phase shift angle, rotor position and frequency variations on loss characteristics[28].

3.2.2 Three-Phase Excitation Expressions

To model a three-phase system with 120° time shifts between the phases, the excitation currents for Phases A, B, and C are defined in ANSYS Maxwell using the following expressions:

$$I_A(t) = 170 + 4I_{\text{rip}}f\left(\left|\operatorname{mod}\left(t + \frac{0.25}{f}, \frac{1}{f}\right) - \frac{0.5}{f}\right| - \frac{0.25}{f}\right) \tag{3.1}$$

$$I_B(t) = 170 + 4I_{\text{rip}}f\left(\left|\operatorname{mod}\left(t + \frac{0.25}{f} + \frac{1}{3f}, \frac{1}{f}\right) - \frac{0.5}{f}\right| - \frac{0.25}{f}\right) \tag{3.2}$$

$$I_C(t) = 170 + 4I_{\text{rip}}f\left(\left|\operatorname{mod}\left(t + \frac{0.25}{f} + \frac{2}{3f}, \frac{1}{f}\right) - \frac{0.5}{f}\right| - \frac{0.25}{f}\right) \tag{3.3}$$

These expressions ensure perfectly balanced three-phase triangular current waveforms centered at 170 A, with phase B and C lagging phase A by 120° and 240°, respectively.

3.2.3 Simulation Setup

3.2.3.1 Parameters

The finite element analysis was conducted on an electrically excited synchronous machine (EESM) using an 1/8-symmetry model to reduce computational cost while maintaining magnetic accuracy. The full machine consists of 48 stator slots and 4 rotor poles, corresponding to a three-phase distributed winding configuration. Table 3.1 lists the key geometrical parameters used in the simulation.

Table 3.1: Main mechanical and geometrical parameters of the EESM.

Parameter	**Value**	**Unit**
Number of slots	48	–
Number of poles	4	–
Number of phases	3	–
Stator outer diameter	220	mm
Rotor outer radius	72.55	mm
Tooth height (H_{sw})	46.6	mm
Slot opening height (H_{sh})	5.8	mm
Pole height (H_{ph})	36	mm
Pole width (H_{pw})	22	mm
Number of winding layers	8	–
Slot fill factor ($FillFactor_s$)	0.68	–
Rotor fill factor ($FillFactor_r$)	0.40	–

The listed parameters define the basic geometry and magnetic structure of the model. The stator dimensions and slot design determine the available winding space and influence copper losses, while the rotor geometry affects the magnetic flux path and field excitation characteristics. The selected fill factors ensure a realistic balance between conductor packing and insulation requirements, maintaining adequate thermal margins during operation[27].

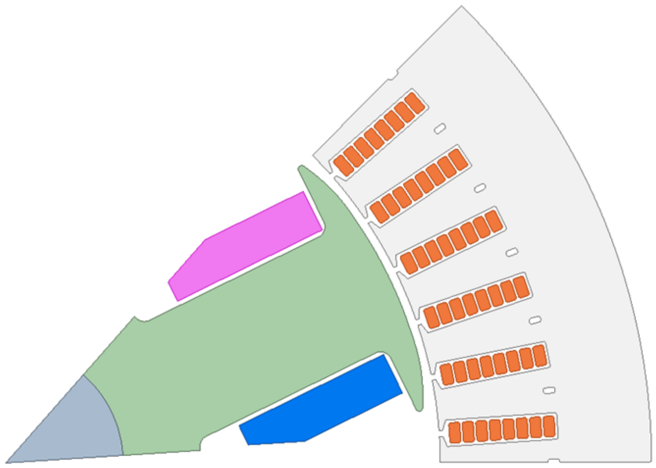

Figure 3.1: One-eighth symmetry model of the electrically excited synchronous machine used in ANSYS Maxwell.

The geometry was modelled with an 1/8-symmetry sector, as shown in Fig. This configuration effectively reduces the mesh size and computation time while preserving the full electromagnetic field distribution. The stator employs a 48-slot, three-phase distributed winding, and the rotor contains four salient poles with field windings supplied by DC excitation. A moderate slot fill factor of 0.68 ensures good copper utilisation without excessive thermal loading. These parameters remained constant for all excitation and frequency sweeps presented in the following sections.

3.2.3.2 Excitation

To generate a balanced three-phase system, the phase currents were shifted by 120° in time. The excitation expressions implemented in ANSYS Maxwell are as follows (using I_{rip} for the ripple current amplitude and f for the ripple frequency):

- **Phase A:**
  ```
  170 + (4*I_rip*f)*(abs(mod(time + 0.25/f, 1/f) - 0.5/f) - 0.25/f)
  ```
- **Phase B:**
  ```
  170 + (4*I_rip*f)*(abs(mod(time + 0.25/f + 1/(3*f), 1/f) - 0.5/f) - 0.25/f)
  ```
- **Phase C:**
  ```
  170 + (4*I_rip*f)*(abs(mod(time + 0.25/f + 2/(3*f), 1/f) - 0.5/f) - 0.25/f)
  ```

Here, the DC offset of 170 A represents the average current, while the ripple amplitude I_{rip} and the ripple frequency f determine the current variation and switching condition[11].

3.2.3.3 Time Step Setup

A transient magnetic solver was employed to capture the electromagnetic response of the machine under time-varying excitation. The simulation time step and total simulation duration were defined as functions of the excitation frequency to maintain consistent temporal resolution across all cases[4]. The stop time was set to two ripple current periods, while the time step corresponded to one hundred and eighty divisions per period, as expressed below:

$$t_{\text{stop}} = \frac{2}{f}, \qquad \Delta t = \frac{1}{180f}$$

where f denotes the ripple current frequency.
For the frequencies considered in this study (1 kHz, 10 kHz, and 20 kHz), the corresponding time-step settings are listed in Table 3.2.

Table 3.2: Transient solver setup for different excitation frequencies.

Frequency (Hz)	Stop time (s)	Time step (s)
1 000	2.00×10^{-3}	5.56×10^{-6}
10 000	2.00×10^{-4}	5.56×10^{-7}
20 000	1.00×10^{-4}	2.78×10^{-7}

This setup ensures that each simulation includes at least two complete current ripple cycles, providing adequate temporal resolution to capture high-frequency variations while maintaining numerical stability. The same configuration was applied for all excitation and frequency sweep cases presented in the following sections[27].

3.3 Simplorer-based Co-Simulation

3.3.1 Co-Simulation Framework

The inverter, controller, and motor model are coupled in Simplorer–Maxwell co-simulation. This dynamic interaction enables accurate analysis of current, losses, and torque under different modulation strategies, reflecting realistic electromagnetic behavior.

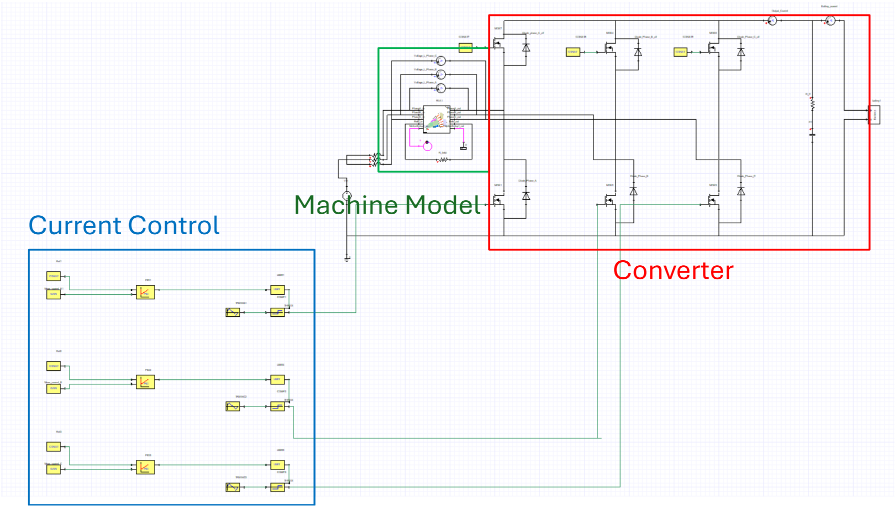

Figure 3.2: Simplorer–Maxwell co-simulation framework

3.3.2 Boost Converter Circuit

The boost converter is realized by reusing the inverter power switches together with the motor stator inductance. This allows energy transfer from a 400 V source to an 800 V battery, avoiding the need for additional large inductors. Current and voltage sensors are integrated to support control and monitoring[29].

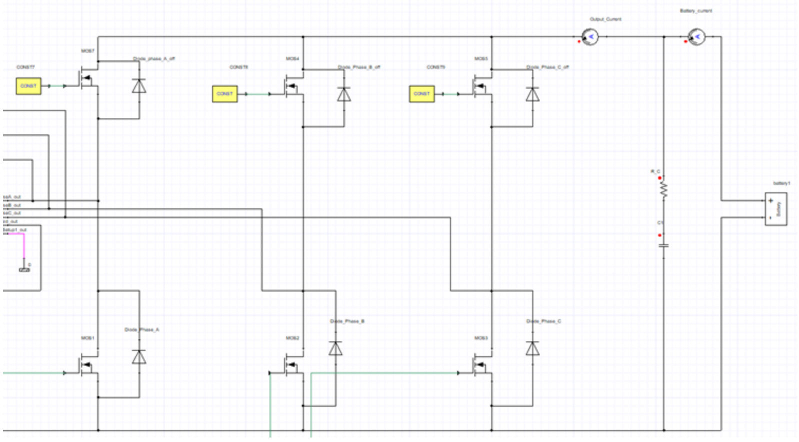

Figure 3.3: Boost Converter constructed from inverter and motor windings

3.3.3 Current Control and PWM Modulation

A PI controller is combined with a carrier-based PWM modulation strategy to regulate the stator current. By setting a current reference, the control system generates PWM signals for the inverter switches, ensuring stable charging current while reducing ripple under different phase-shift strategies[17].

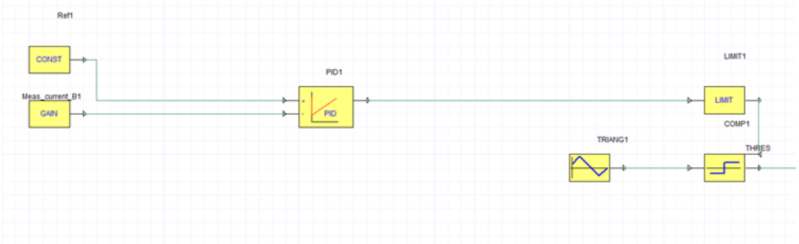

Figure 3.4: Current control loop with PI regulator and PWM generation

3.4 Simulink-based System Simulation

To verify the converter control strategy and evaluate the overall dynamic performance of the drive, a system-level simulation was established in MATLAB/Simulink. The model integrates both the control and power stages, allowing analysis of current regulation, switching behavior, and DC-link stability[30].
As shown in Fig. 3.5, the system employs a three-phase bidirectional boost converter topology. Each leg is independently controlled by a PWM signal, enabling

bidirectional power flow between the DC source and the machine. The converter maintains the DC-link voltage and regulates the inductor current of each phase[31].

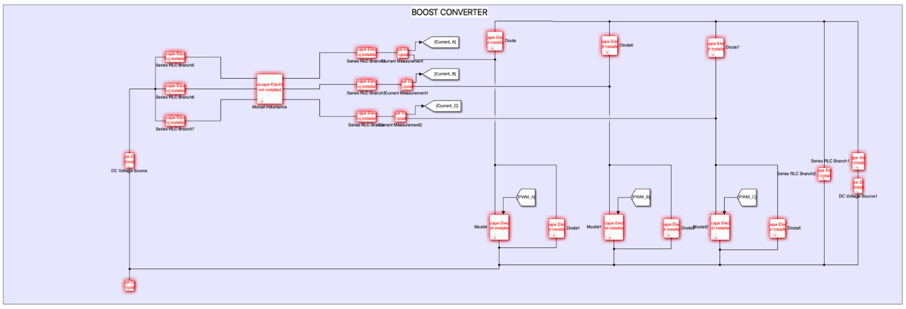

Figure 3.5: Three-phase bidirectional boost converter implemented in Simulink.

For the current regulation, a standard PI control loop was applied to each converter phase, as illustrated in Fig. 3.6. The reference current i_{ref} is compared with the measured inductor current i_L, and the error is processed by the proportional–integral controller:

$$u(t) = K_p[i_{\text{ref}}(t) - i_L(t)] + K_i \int_0^t [i_{\text{ref}}(\tau) - i_L(\tau)] \, d\tau$$

The resulting voltage command $u(t)$ determines the PWM duty ratio of the corresponding switching leg. This closed-loop control maintains the desired inductor current waveform, minimizes steady-state error, and ensures symmetrical operation among the three phases[17].

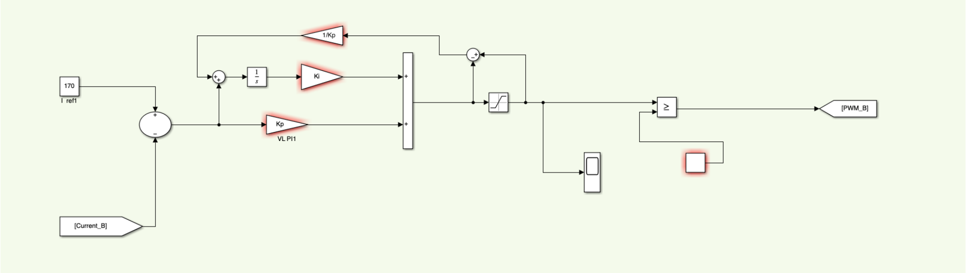

Figure 3.6: PI current controller for one converter phase in Simulink.

During simulation, the DC-link voltage, inductor current, and PWM duty ratio were monitored to assess converter efficiency and transient response. A fixed-step solver with a time step of $1/(180f)$ was employed to synchronize with the switching frequency and ensure numerical stability[30].

4

Results

4.1 Machine—Standalone Simulation

In this section, finite element simulations were performed on the Electrically Excited Synchronous Machine (EESM) in standalone mode, with the aim of evaluating its electromagnetic performance in terms of core losses, inductance and torque. Two parametric analyses were conducted at three excitation frequencies: 1 kHz, 10 kHz, and 20 kHz. In the first study, both the excitation frequency and the ripple amplitude were varied, while in the second study, the ripple amplitude was fixed at 5 A and the phase-shifting angle between the stator currents and the rotor mechanical position was adjusted. These results clearly demonstrate how switching frequency, current ripple and phase displacement influence the machine's magnetic field behaviour and torque production[32].

4.1.1 Parametric Sweep of Frequency and Ripple

Parameter scans were conducted at frequencies of 1 kHz, 10 kHz and 20 kHz for different current ripple amplitudes, in order to analyse the effects of frequency and ripple current on motor losses, inductance and torque. The results show that, as the current ripple amplitude increases, core and additional losses rise significantly, while changes in inductance are negligible and torque decreases slightly. These results suggest that current ripple primarily affects energy losses by altering the rate of change and distribution characteristics of magnetic flux density, while having a relatively minor impact on electromagnetic coupling relationships.

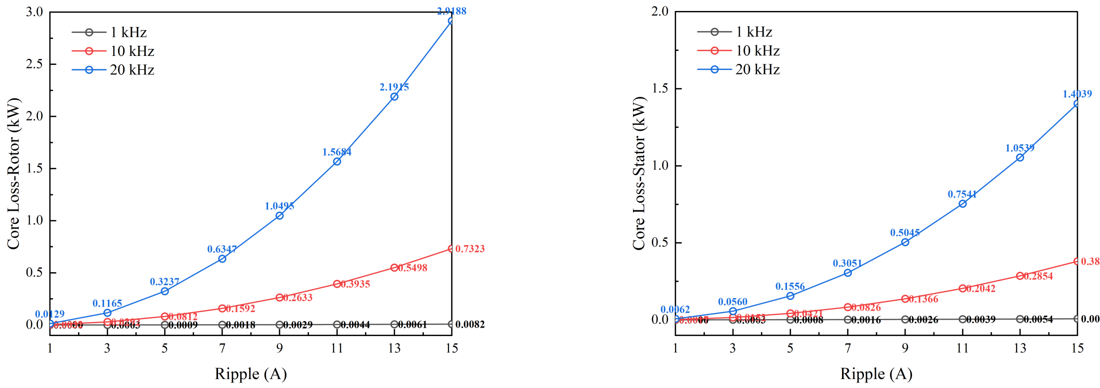

(a) Rotor core losses

(b) Stator core losses

Figure 4.1: Machine Standalone—Core losses vs. current ripple

The trend of variation in rotor core loss is more sensitive to frequency. At 20 kHz, the rotor core loss increases significantly compared to 10 kHz, exhibiting a quadratic growth trend alongside ripple amplitude. This is due to the pole shoe area of the rotor having a higher magnetic flux density and thicker geometry, which makes it difficult to suppress local eddy current loops. Consequently, the additional loss caused by flux variation becomes more pronounced in high-frequency ripple conditions, rendering the rotor core the primary source of loss as both frequency and ripple increase[33].

Stator core loss increases significantly with both ripple amplitude and frequency, particularly at higher frequencies. At 20 kHz, the stator core loss is about two to three times higher than at 10 kHz, while at 1 kHz it is almost negligible. This trend is primarily due to two factors: firstly, the magnetic flux reversal rate (dB/dt) increases at higher frequencies, and secondly, a larger ripple amplitude increases the flux swing (ΔB) in the air gap. These effects combine to enhance both hysteresis and eddy current losses, resulting in nonlinear growth in total core loss. Additionally, the tooth tips and slot openings of the stator are the primary regions of energy dissipation due to magnetic flux concentration[34].

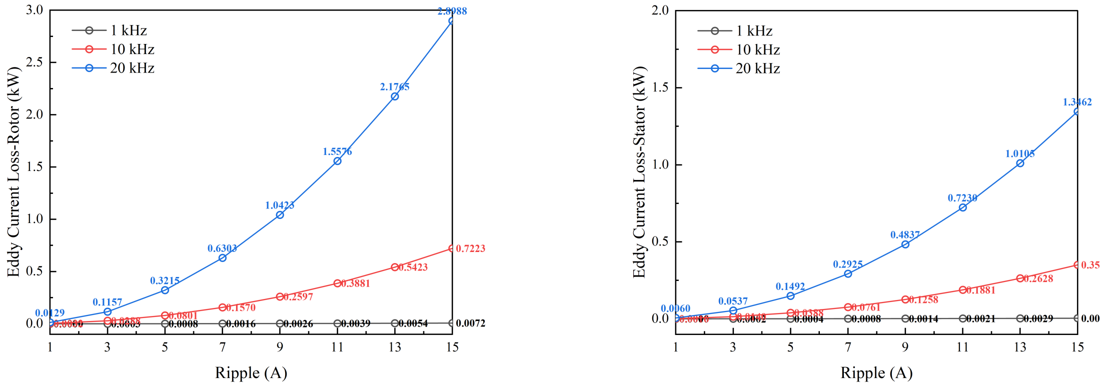

(a) Rotor eddy losses

(b) Stator eddy losses

Figure 4.2: Machine Standalone—Eddy current losses vs. current ripple

Rotor eddy current loss is much higher than stator loss and is highly sensitive to frequency and ripple amplitude. At 20 kHz, it increases almost exponentially with ripple amplitude. This is mainly due to the skin effect, which strengthens at higher frequencies and reduces the skin depth ($\delta = \sqrt{2\rho/(\mu\omega)}$). Consequently, the induced current becomes concentrated near the pole shoe surface, resulting in significant localised Joule heating. Furthermore, the greater thickness of the rotor pole structure increases the volume of energy dissipation. Therefore, rotor eddy current loss is one of the main sources of loss under high-frequency ripple conditions[35].

The stator eddy current loss increases gradually with frequency and ripple amplitude. Due to the stator's laminated structure, the insulation between layers effectively blocks circulating currents, keeping the overall loss level low. However, under high-frequency conditions (especially at 20 kHz), some surface current density concentration can occur near the tooth tips and slot openings, resulting in a slight increase in local energy dissipation. Nevertheless, the overall change remains limited.

4.1.1.1 Eddy Current Losses under Different Ripple Amplitudes

Figure 4.3 presents the magnetic flux density distribution for ripple amplitudes ranging from 3 A to 15 A. As the ripple amplitude increases, the magnetic field variation within each electrical period becomes more intense, and localized saturation is observed at the stator tooth tips. Since the instantaneous magnetic flux density is directly related to the excitation current through $B \propto \mu NI/l_m$, the enlarged current swing ΔI broadens the magnetic hysteresis loop and intensifies the alternating component of B.

From a physical viewpoint, the total core loss P_{core} consists of two components: hysteresis and eddy-current losses. The hysteresis loss depends linearly on frequency and on the width of the B–H loop ($P_{\text{hyst}} \propto fB^n$), while the eddy-current loss scales with the square of both the frequency and flux density amplitude ($P_{\text{eddy}} \propto f^2B^2$). Therefore, increasing the ripple amplitude enlarges the magnetic flux swing ΔB, which directly increases both components—particularly the eddy-current term, as stronger $\mathrm{d}B/\mathrm{d}t$ produces higher induced current density in the laminated core.

The field plots clearly demonstrate this effect: regions of high magnetic flux density appear more extended and intense as the ripple amplitude grows, confirming that the rise in eddy-current loss originates from enhanced magnetic flux variation rather than material properties. At large ripple values, local saturation also contributes to higher magnetic hysteresis loss, as indicated by the widening of the magnetic loop[35].

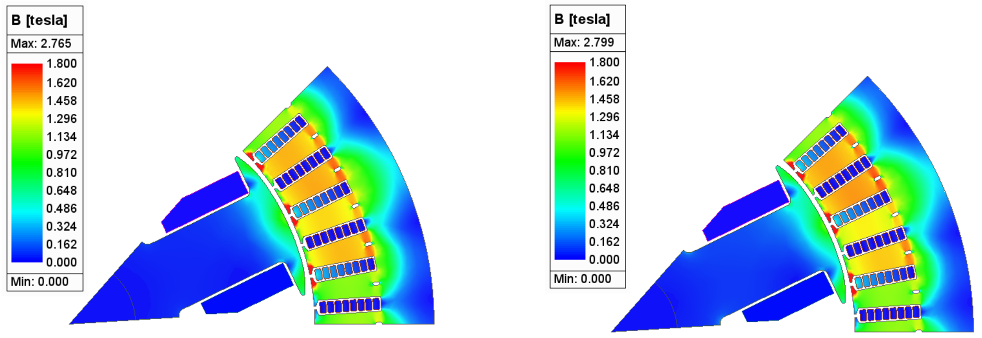

(a) Ripple = 3 A

(b) Ripple = 7 A

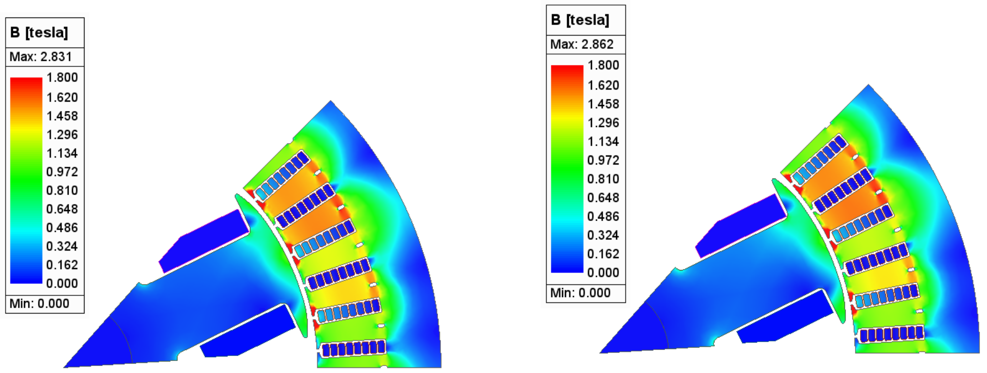

(c) Ripple = 11 A

(d) Ripple = 15 A

Figure 4.3: Magnetic flux density distribution under different current ripple amplitudes.

As the ripple amplitude increases from 3 A to 15 A, the magnetic flux variation ΔB becomes more pronounced, particularly near the stator tooth tips. This enhanced magnetic swing enlarges the hysteresis loop area and intensifies eddy-current formation in the laminated core, leading to increased core losses.

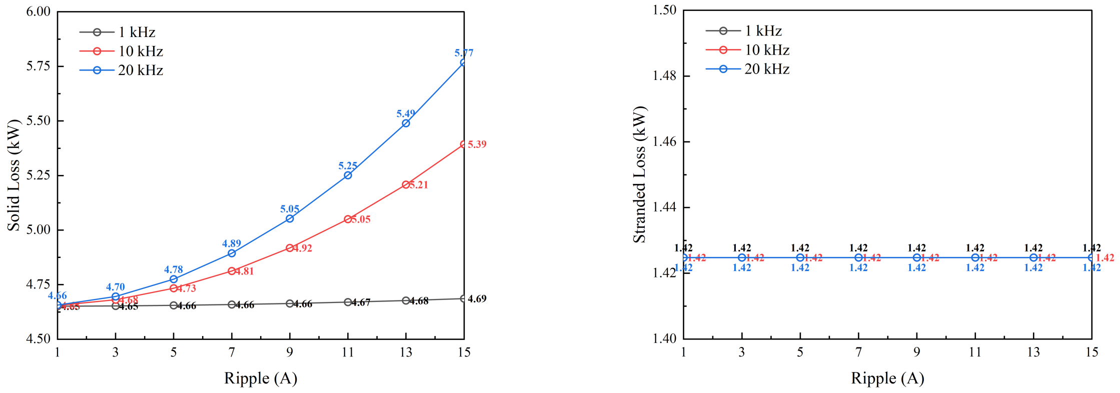

(a) Solid losses

(b) Stranded losses

Figure 4.4: Machine Standalone—Solid and stranded losses vs. current ripple

Solid loss refers to the current losses induced by high frequencies inside magnetic materials. These losses increase smoothly with both frequency and ripple amplitude, but remain smaller than core losses due to magnetic field disturbances inside the core material.

Stranded loss corresponds to additional copper losses in the windings caused by skin and proximity effects. At 1 kHz and 10 kHz, stranded loss remains nearly constant; however, at 20 kHz, it increases slightly with ripple. Due to the small wire diameter and moderate slot fill factor, current crowding is limited, resulting in only minor variations[36].

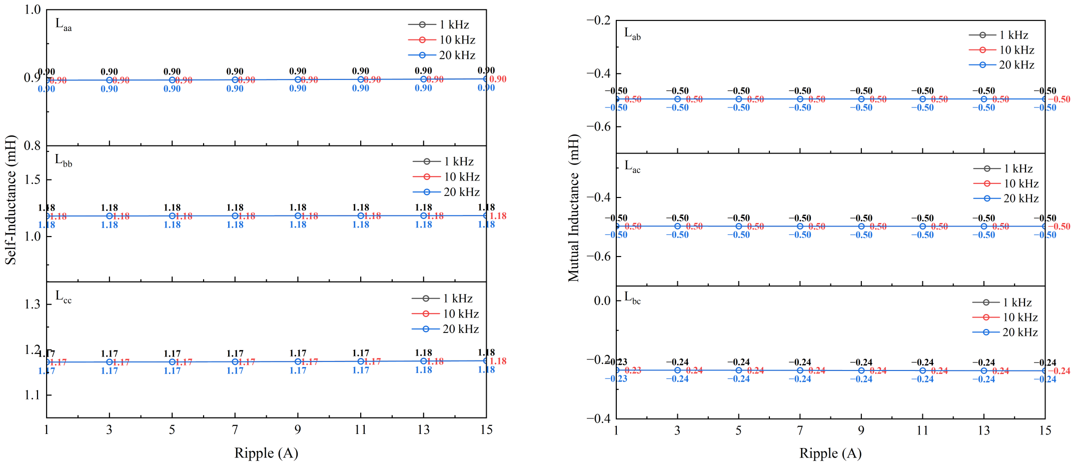

(a) Self inductance

(b) Mutual inductance

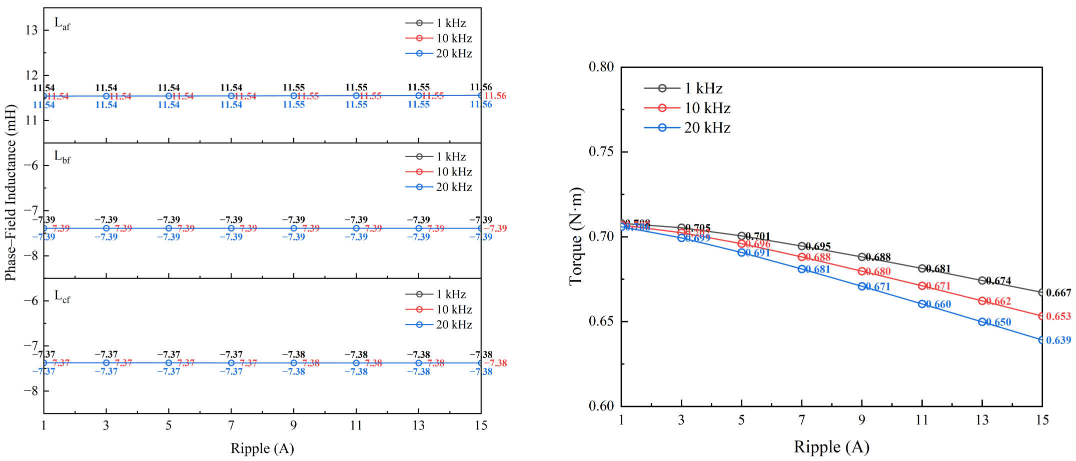

(c) Phase-field inductance

(d) Electromagnetic torque

Figure 4.5: Machine Standalone—Inductances and torque vs. current ripple

The self-inductances (L_{aa}, L_{bb} and L_{cc}), mutual inductances (L_{ab}, L_{ac} and L_{bc}), and excitation mutual inductances (L_{af}, L_{bf} and L_{cf}) remain almost constant across different frequencies and ripple amplitudes. This shows that, within the current analysis range, the magnetic circuit does not enter a clear saturation region and that the magnetic coupling remains stable. The current ripple primarily alters the transient magnetic field distribution rather than the average magnetic flux linkage[32].

The electromagnetic torque decreases slightly as the ripple amplitude increases, with a more noticeable reduction at higher frequencies. When the frequency increases from 1 kHz to 20 kHz, the average torque decreases by approximately 8–10%. This is primarily because high-frequency ripple introduces harmonic magnetic fields, which distort the air-gap flux density waveform and intensify torque ripple. Additionally, higher losses reduce energy conversion efficiency[37].

In general, the current ripple has little influence on inductance, but it slightly reduces the average torque and increases torque fluctuation. Furthermore, since the air-gap flux density is proportional to the current, the peak magnetic flux density increases almost linearly with the ripple amplitude.

4.1.2 Simulation under Fixed Ripple (5A) with Varying Shift Angle and Rotor Position

In this section, the ripple current amplitude is fixed at 5 A to analyze the influence of the phase-shifting angle and the rotor position on the machine's electromagnetic behavior. this section investigates how spatial and temporal phase relationships influence performance under identical excitation strength. Specifically, the analysis includes two aspects: the variation of the phase-shifting angle between stator currents; and the change in the rotor's mechanical position. Both studies are conducted at switching frequencies of 1 kHz, 10 kHz, and 20 kHz. The results obtained provide insight into how PWM phase displacement and rotor alignment affect magnetic coupling, losses and torque characteristics in the machine[38].

4.1.2.1 Shift Angle

This section investigates the influence of the phase-shifting angle between the three-phase stator currents under a fixed ripple amplitude of 5 A. This angle determines the phase displacement between the stator current waveforms, directly affecting the temporal distribution of the magnetic field and resulting electromagnetic losses. Sweeping the shift angle from 0° to 120° allows us to analyze the variations in core losses, eddy current losses, copper losses, inductances and electromagnetic torque at different excitation frequencies (1 kHz, 10 kHz and 20 kHz). The objective of this study is to clarify how the temporal phase difference of the excitation current modulates magnetic field dynamics and energy conversion efficiency in the machine[37].

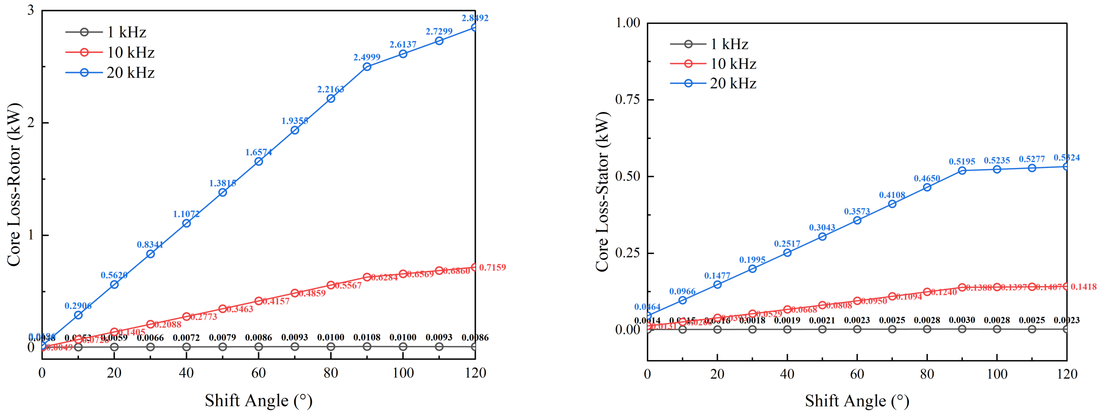

(a) Rotor core losses **(b)** Stator core losses

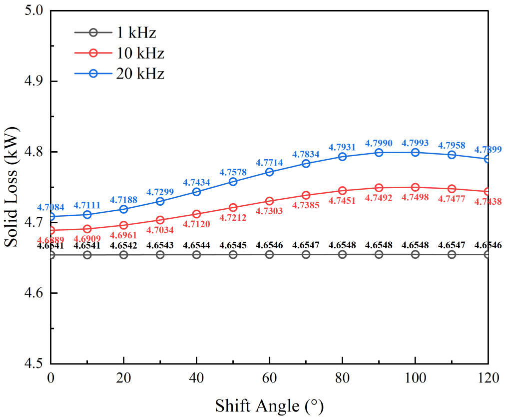

(c) Solid losses

Figure 4.6: Machine Standalone—Core and solid losses vs. shift angle

As shown in Figure 4.6, both the stator and the rotor core losses increase with the shift angle, particularly under high-frequency conditions. Stator loss grows moderately and tends to saturate after 60°, whereas rotor core loss rises almost linearly, reaching 2.8–2.9 kW at 20 kHz. This trend is explained by the increased temporal flux fluctuation caused by the phase displacement between the stator currents. As the phase shift increases, each rotor section experiences more frequent magnetic polarity reversals, thus intensifying hysteresis and eddy currents within the laminated rotor core. Meanwhile, the solid loss remains almost constant at around 4.7 kW, indicating that bulk iron energy conversion is less sensitive to phase variation[39].

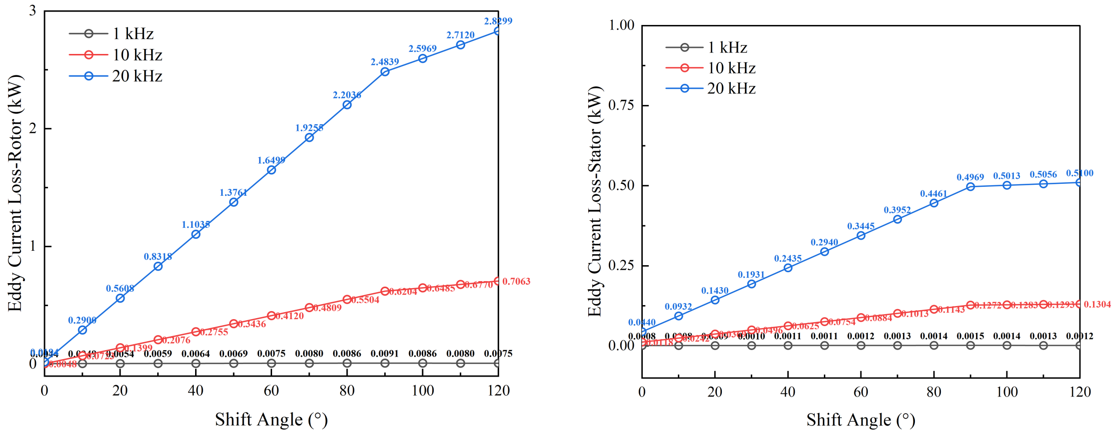

(a) Rotor eddy losses **(b)** Stator eddy losses

Figure 4.7: Machine Standalone—Eddy current losses vs. shift angle

It shows that both the stator and the rotor eddy losses increase significantly with the phase-shifting angle, especially at 10 kHz and 20 kHz. As the phase displacement increases, the resulting air-gap flux density becomes spatially imbalanced, intensifying its local time derivative (dB/dt), particularly along the rotor surface. Under such high-frequency, high-dB/dt conditions, the skin effect confines the induced current to the outermost conductive layers of the rotor. Meanwhile, the proximity effect further distorts the current distribution due to magnetic coupling between adjacent slots and poles. These effects collectively increase the local current density and Joule heating, resulting in the substantial growth in rotor eddy losses observed. In contrast, the stator core is laminated and thus less affected by variation in skin depth, showing only a moderate increase in loss[32].

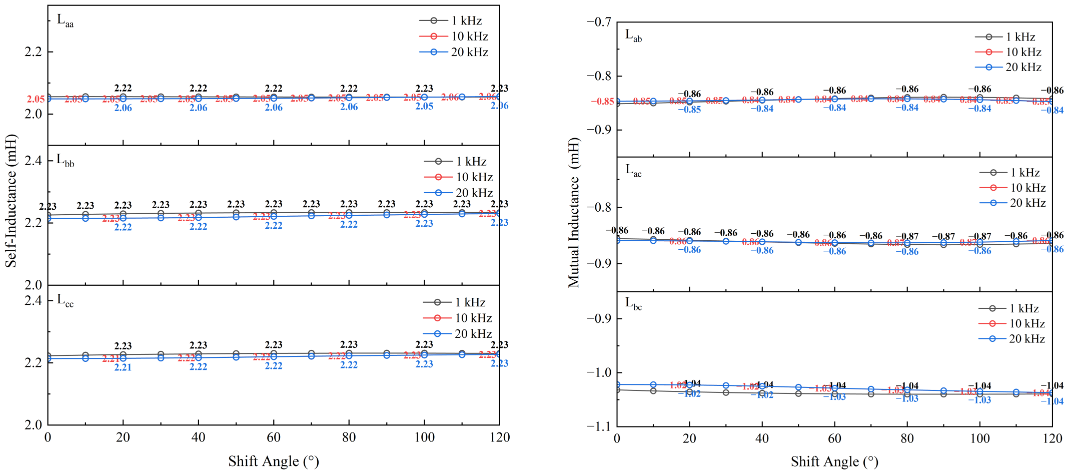

(a) Self inductance **(b)** Mutual inductance

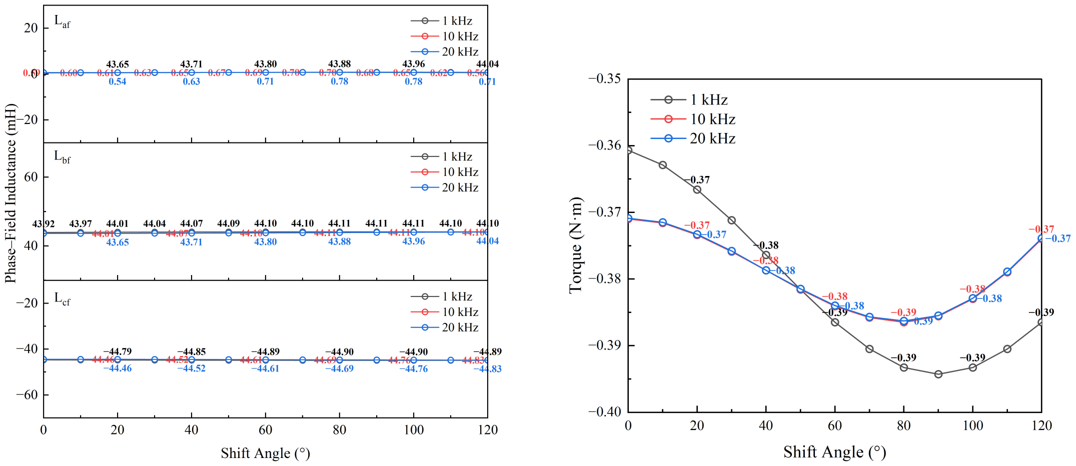

(c) Phase-field inductance **(d)** Electromagnetic torque

Figure 4.8: Machine Standalone—Inductance characteristics and torque vs. shift angle

The self, mutual and phase-field inductances remain almost constant across the entire shift-angle range. This suggests that the magnetic permeability and coupling between windings are not greatly affected by temporal current phase displacement. However, the electromagnetic torque shows a slight sinusoidal decrease as the shift angle increases, reaching a minimum at around 90°. This reduction stems from the partial misalignment of the phase between the magnetic flux and the stator current, which reduces the effective component that produces torque. Nevertheless, the variation is minor, indicating stable torque production despite the changing phase offset[17].

4.1.2.2 Rotor Position

The analysis in this section was carried out under a fixed current ripple of 5 A, while the rotor mechanical position was incrementally varied from 0° to 120°. The objective is to examine how rotor movement in space affects the distribution of magnetic flux, the inductance profile, and the resulting torque.

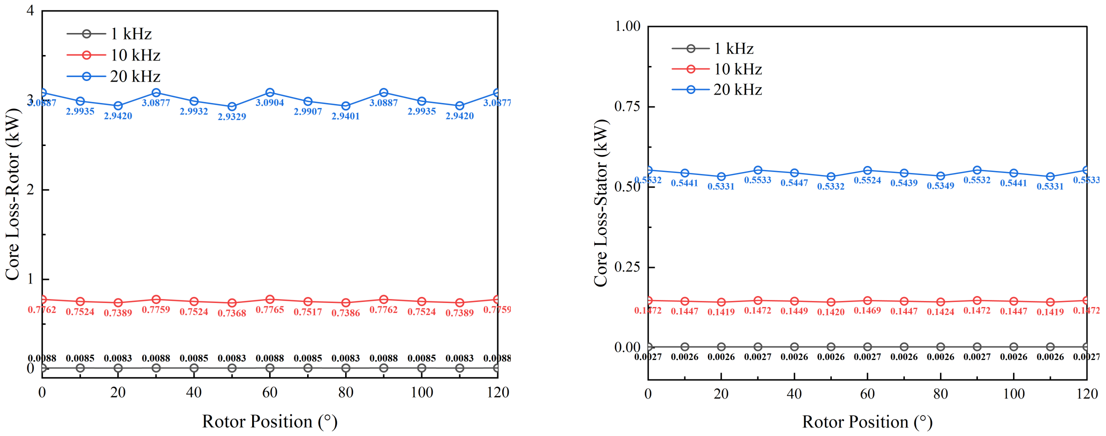

(a) Rotor core losses **(b)** Stator core losses

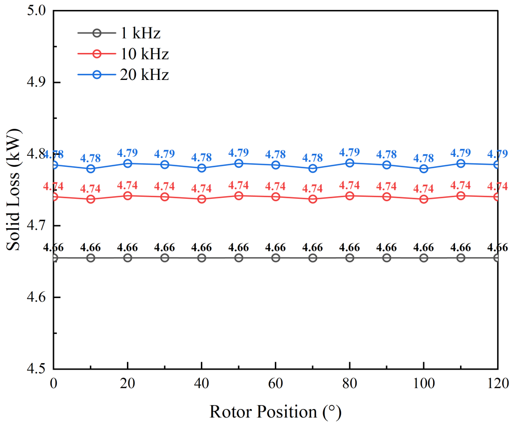

(c) Solid losses

Figure 4.9: Machine Standalone—Core and solid losses vs. rotor position

Both the stator and the rotor core losses remain almost constant throughout mechanical rotation. This steady trend indicates that loss behaviour is primarily governed by time-domain excitation, such as frequency and ripple amplitude, rather than spatial displacement. The slight air-gap field distortion at high frequency causes a weak fluctuation, but its magnitude is negligible. Similarly, the solid loss curve remains stable, confirming that the magnetic energy conversion inside the iron core does not significantly vary with rotor angle[39].

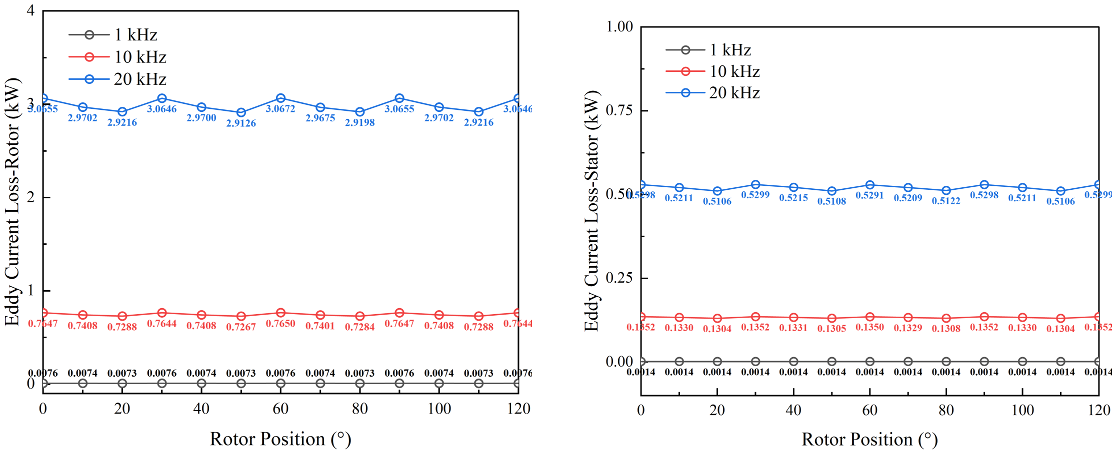

(a) Rotor eddy losses

(b) Stator eddy losses

Figure 4.10: Machine Standalone—Eddy current losses vs. rotor position

Both the stator and the rotor eddy losses demonstrate minimal dependence on the position of the rotor, remaining almost constant across all frequencies. This demonstrates that, once the frequency and ripple are fixed, the distribution of induced currents in the conductive paths is steady. Skin and proximity effects are still present at high frequency. However, their influence does not vary with rotor movement. This is because the excitation frequency remains unchanged. And thus the rate of magnetic field change stays the same[32].

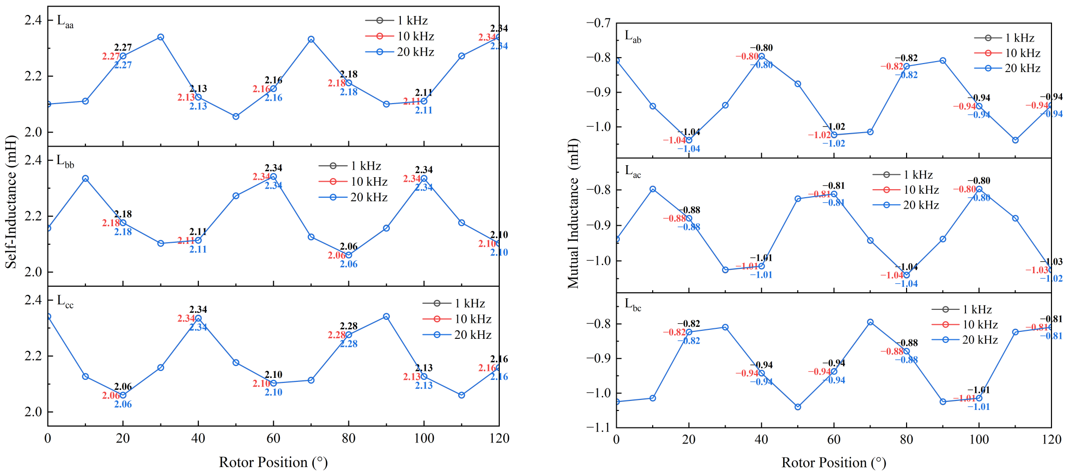

(a) Self inductance **(b)** Mutual inductance

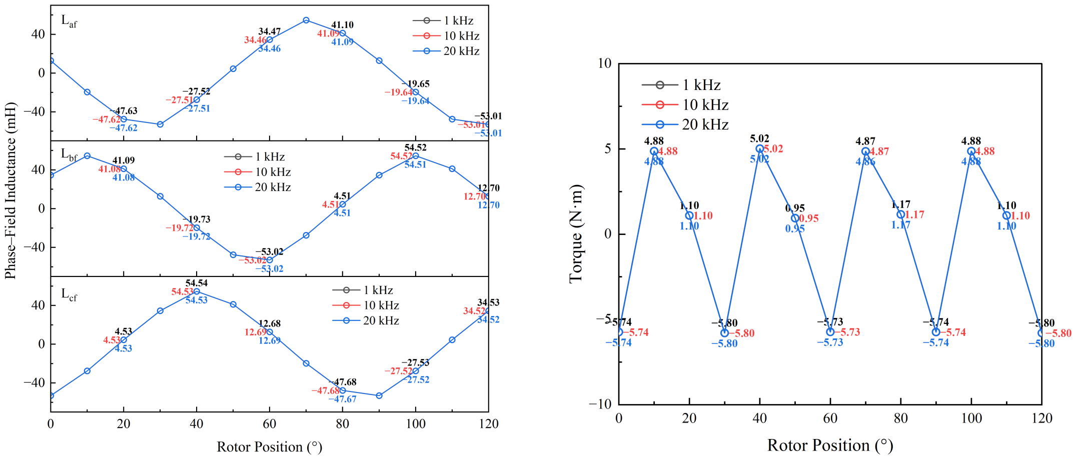

(c) Phase mutual inductance **(d)** Electromagnetic torque

Figure 4.11: Machine Standalone—Inductance characteristics and torque vs. rotor position

In contrast to the loss characteristics, the inductance components vary periodically with rotor position, reflecting the machine's inherent magnetic symmetry. The self- and mutual inductances exhibit spatial periodicity corresponding to one pole pitch. Meanwhile, the phase–field inductances follow a sinusoidal trend that mirrors the air-gap flux linkage. The electromagnetic interaction between the stator MagnetoMotive Force (MMF) and the rotor field is illustrated by the torque oscillating periodically between positive and negative peaks. These periodic variations are indicative of normal magnetic coupling behaviour rather than additional losses or instabilities[33].

4.2 Simplorer-based Co-Simulation

To further investigate the interaction between the machine and its charger system, a Simplorer–Maxwell co-simulation model was established. Unlike the previous standalone analyses in Maxwell, which focused on the electromagnetic behavior of the

machine under predefined excitations, the co-simulation enables the dynamic coupling between the electrical drive circuit, control strategy, and the finite-element machine model. This setup allows for a more realistic representation of the operating conditions, where inverter switching, current control, and machine back electromotive force (EMF) are fully coupled in the time domain[40].
In this section, the simulation focuses on the steady-state operation of the Electrically Excited Synchronous Machine (EESM) under controlled current excitation. By adjusting the inverter switching frequency and the current phase angle, the resulting current ripple, losses, inductances, and torque characteristics are analyzed. The results provide an important reference for validating the machine design under system-level excitation conditions and for assessing the influence of control and circuit parameters on electromagnetic performance[41].

4.2.1 Shift Angle

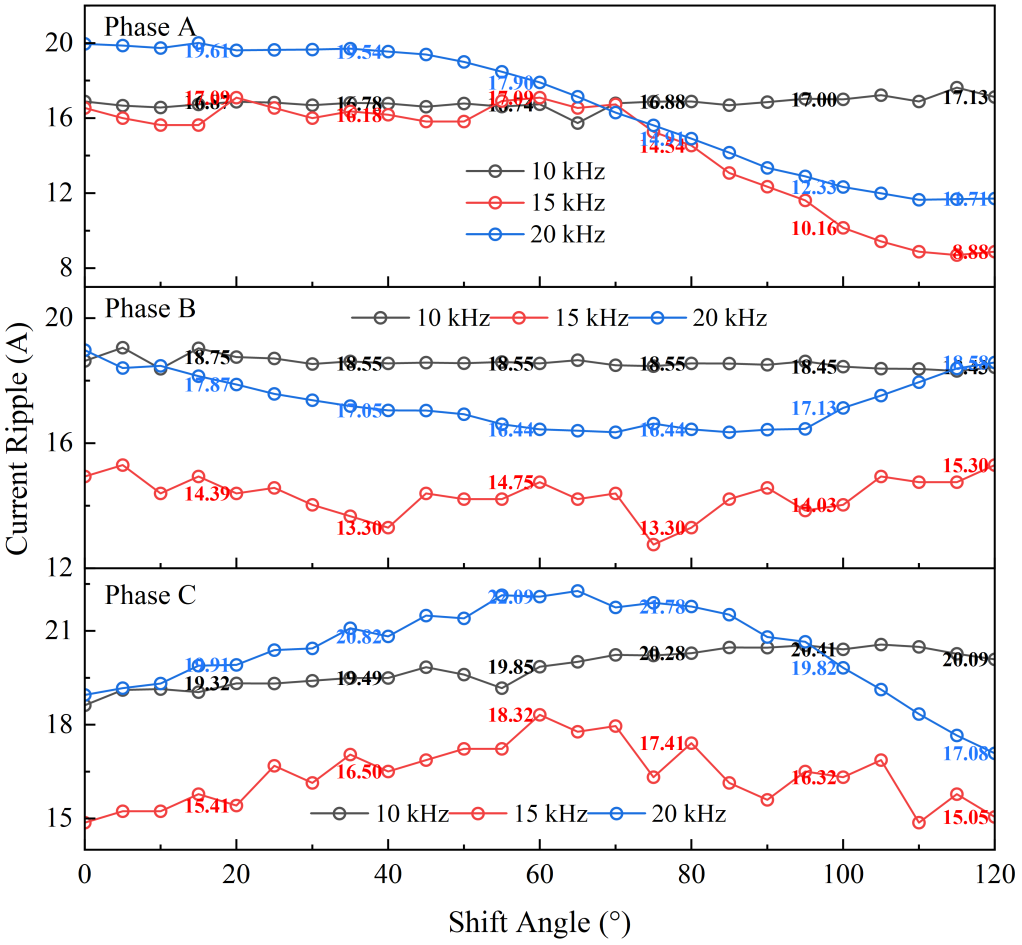

Figure 4.12: Simplorer-based Co-Simulation—Phase current ripple vs. shift angle

The phase current ripple of all three phases decreases noticeably as the shift angle increases. This is because phase-shifted PWM modulation distributes the carrier phases among the three phases, leading to partial cancellation of harmonic energy and a reduction in high-frequency current components. At 10 kHz, the ripple reaches its maximum, while at 20 kHz, it becomes the smallest, following the general inverse relationship between current ripple and carrier frequency.

Theoretically, the peak-to-peak current ripple ΔI can be approximated as:

$$\Delta I = \frac{V_{\mathrm{dc}} \cdot D(1 - D)}{L \cdot f_{\mathrm{s}}}$$

where V_{dc} is the DC-link voltage, D is the duty ratio, L is the equivalent phase inductance, and f_{s} is the switching frequency. This expression indicates that the current ripple is inversely proportional to the switching frequency and directly affected by the DC voltage and system inductance.

However, the reduction is not exactly proportional to the frequency ratio (i.e., the ripple at 20 kHz is not half of that at 10 kHz). This deviation arises from several non-ideal factors: (1) the effective voltage amplitude slightly decreases at higher switching frequencies due to dead-time and switching losses; (2) the stator inductance exhibits weak magnetic nonlinearity under time-varying excitation; (3) harmonic cancellation caused by phase shifting is not perfectly symmetrical across frequencies; and (4) numerical coupling between Simplorer and Maxwell introduces discretization and filtering effects. As a result, the observed ripple reduction trend aligns qualitatively with theory but not in a strictly linear proportion.

Overall, the combined optimization of carrier frequency and phase-shift angle significantly improves the electromagnetic and thermal performance of the machine system[40].

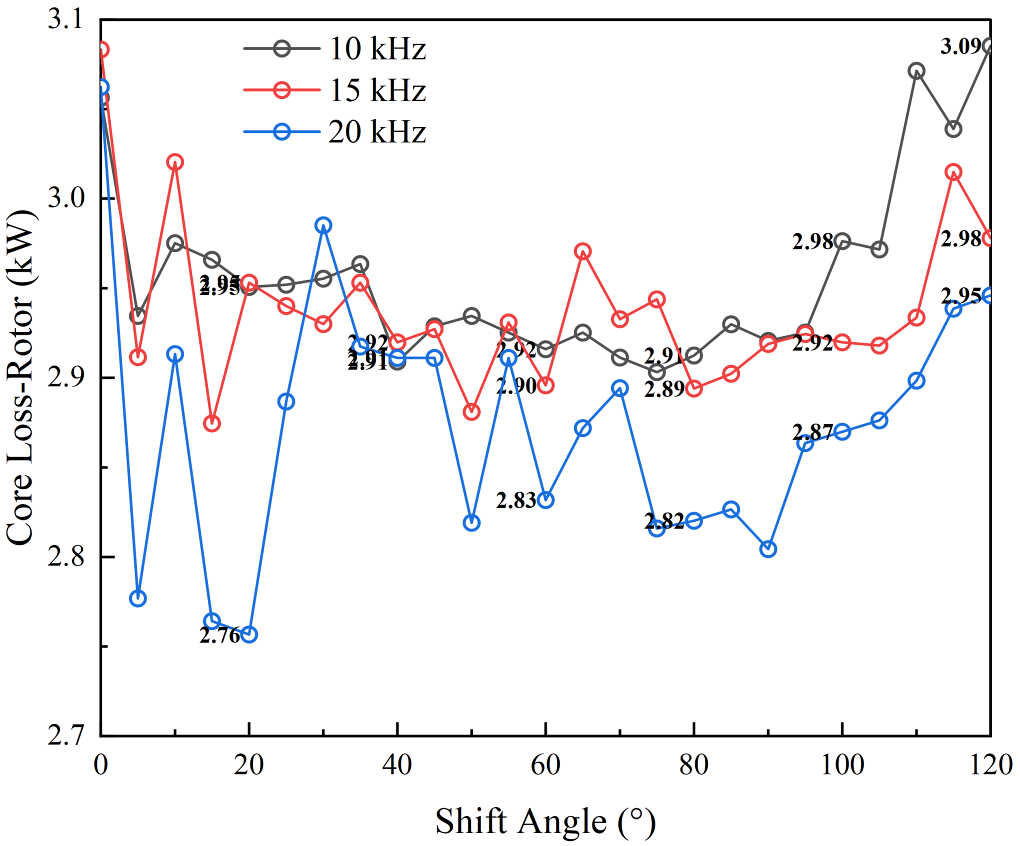

Figure 4.13: Simplorer-based Co-Simulation—Rotor core losses vs. shift angle

As shown in the figure, rotor iron losses vary minimally across the entire phase shift angle range and remain largely stable between 2.8 and 3.0 kW. The loss curves at different frequencies are closely aligned, with slightly higher losses at 10 kHz and slightly lower losses at 20 kHz. This indicates that rotor iron losses are insensitive to variations in the PWM phase angle. As the rotor section is primarily driven by the excitation magnetic field, it is less susceptible to stator voltage modulation. PWM phase shifting only partially alters the timing distribution of current harmonics, having little impact on the main magnetic flux component. From an electromagnetic loss perspective, iron losses comprise two components: hysteresis loss and eddy current loss. Hysteresis loss is proportional to the magnitude of the magnetic flux, while eddy current loss is proportional to the square of the rate of change of magnetic flux. Adjusting the phase shift angle alters the time-domain distribution of the stator composite magnetic potential. However, since the internal rotor flux is primarily generated by DC excitation, the resulting change is limited. This finding suggests that phase shift modulation primarily affects stator-side flux dynamics with little impact on energy losses in the rotor core[42].

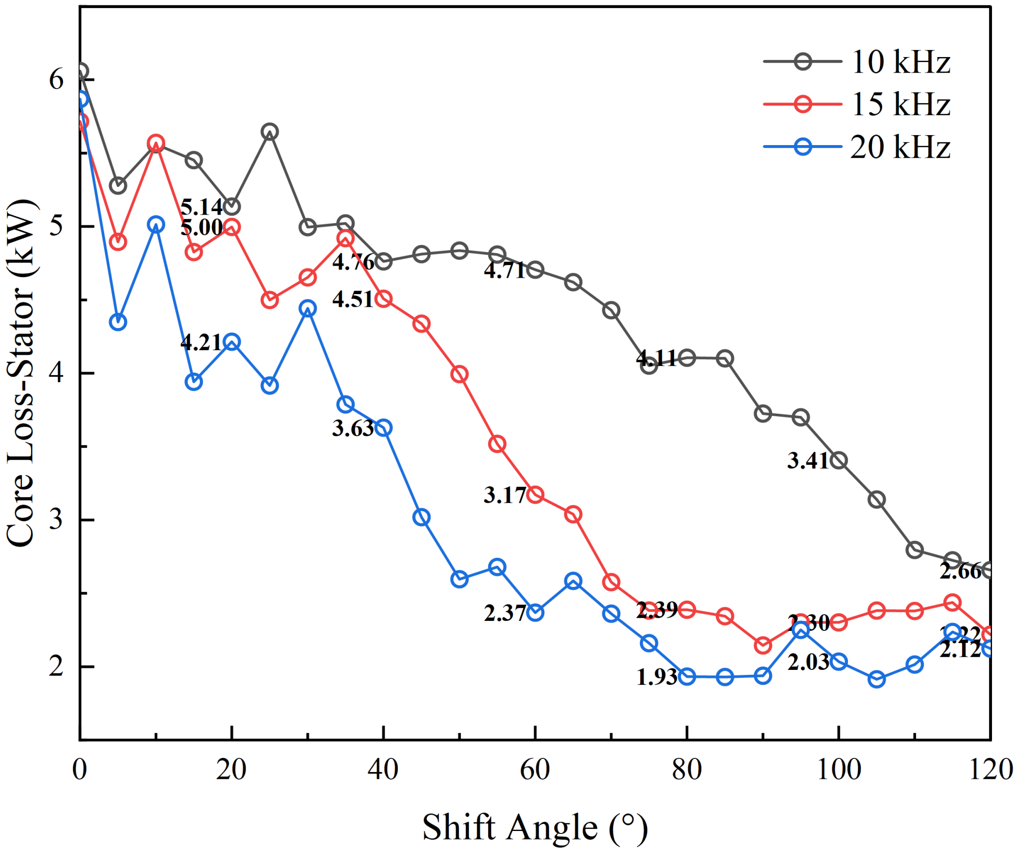

Figure 4.14: Simplorer-based Co-Simulation—Stator core losses vs. shift angle

The variation trend of stator core losses with respect to the shift angle is evident, showing an overall decreasing tendency. As the shift angle increases from 0° to 120°, the stator core losses are significantly reduced, with the highest value observed at 10 kHz and the lowest at 20 kHz.

This behavior occurs because the phase-shifted PWM modulation separates the carrier signals among the three phases in time, leading to partial cancellation of harmonic components in the phase voltage. Consequently, the flux density waveform becomes smoother, reducing both hysteresis and eddy-current losses. The core loss power can be expressed as:

$$P_{\text{core}} = k_h f B_{\max}^n + k_e f^2 B_{\max}^2 \tag{4.1}$$

where k_h and k_e are the hysteresis and eddy-current coefficients, f is the excitation frequency, and $B_{\max}$ is the maximum flux density.

As seen from the equation, the losses are closely related to both frequency and flux variation rate. Although higher frequencies increase the base frequency, the phase-shifted PWM significantly suppresses high-order harmonics, leading to a smoother flux waveform and consequently lower overall core losses.

This trend indicates that increasing the carrier phase shift can effectively improve the flux distribution within the stator core and enhance the overall efficiency of the machine system[40].

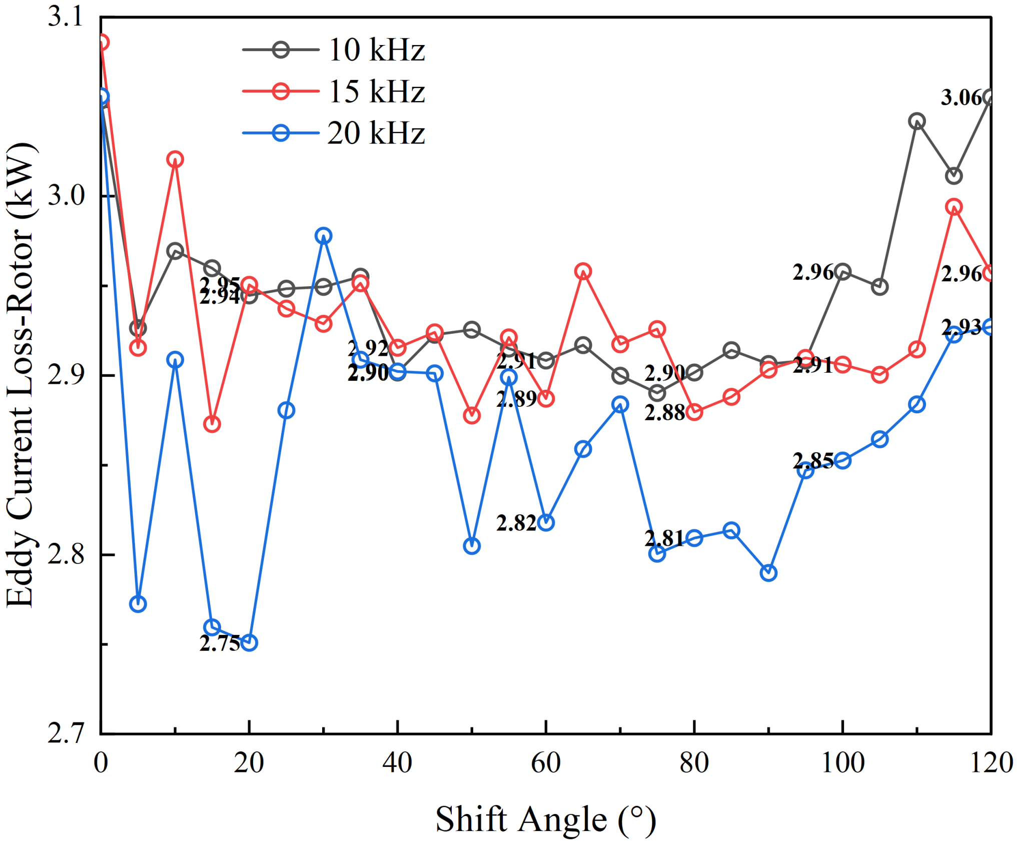

Figure 4.15: Rotor eddy losses vs. shift angle

The trend of eddy current losses in the rotor is similar to that of rotor iron losses, with the curve remaining relatively stable across the entire range and showing only a slight increase at small phase angles (0°–20°). At low phase angles, there is greater overlap of the three-phase pulse width modulated (PWM) carrier waves, where the high-frequency current components superimpose. This increases the rate of change in magnetic flux density, thereby inducing stronger eddy current circulation. As the phase angle increases, however, carrier phase separation reduces this superposition effect, decreasing the induced currents in the rotor's conductive materials and stabilising the losses. This suggests that phase-shift modulation effectively suppresses high-frequency harmonics. However, due to the relatively high conductivity of the rotor section, and because magnetic flux changes are primarily influenced by the main field, the overall losses remain within a stable range[42].

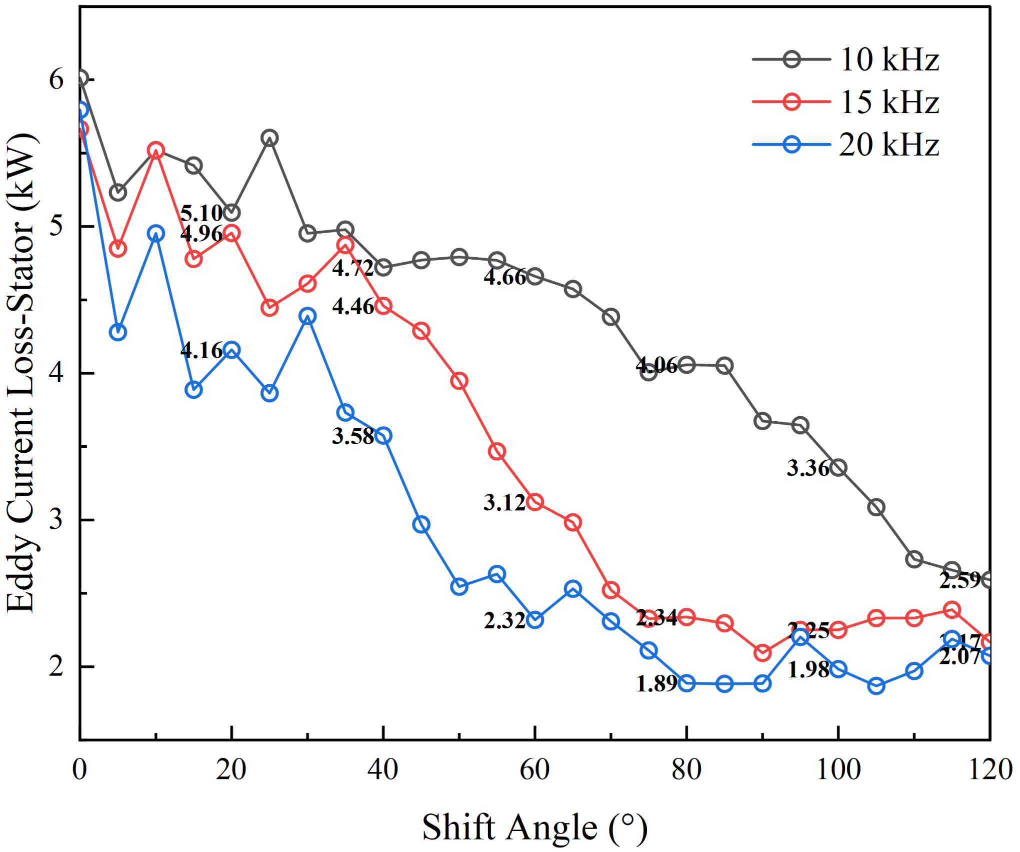

Figure 4.16: Simplorer-based Co-Simulation—Stator eddy losses vs. shift angle

Consistent with the pattern of stator iron losses, stator eddy current losses decrease significantly with increasing phase shift angle. This is primarily because the induced currents in the stator core are caused by changes in the magnetic flux, and phase shift modulation reduces the rate at which this flux varies. As the phase shift angle increases, the superimposed waveforms of the three-phase carriers become more uniform. This weakens fluctuations in the equivalent magnetic flux linkage and effectively reduces high-frequency magnetic flux density components. Consequently, eddy current losses peak at 10 kHz and are lowest at 20 kHz. These results clearly demonstrate that phase shift control improves the quality of the output voltage waveform and effectively reduces core losses caused by high-frequency magnetic fields. This supports efficient motor operation at high switching frequencies[40].

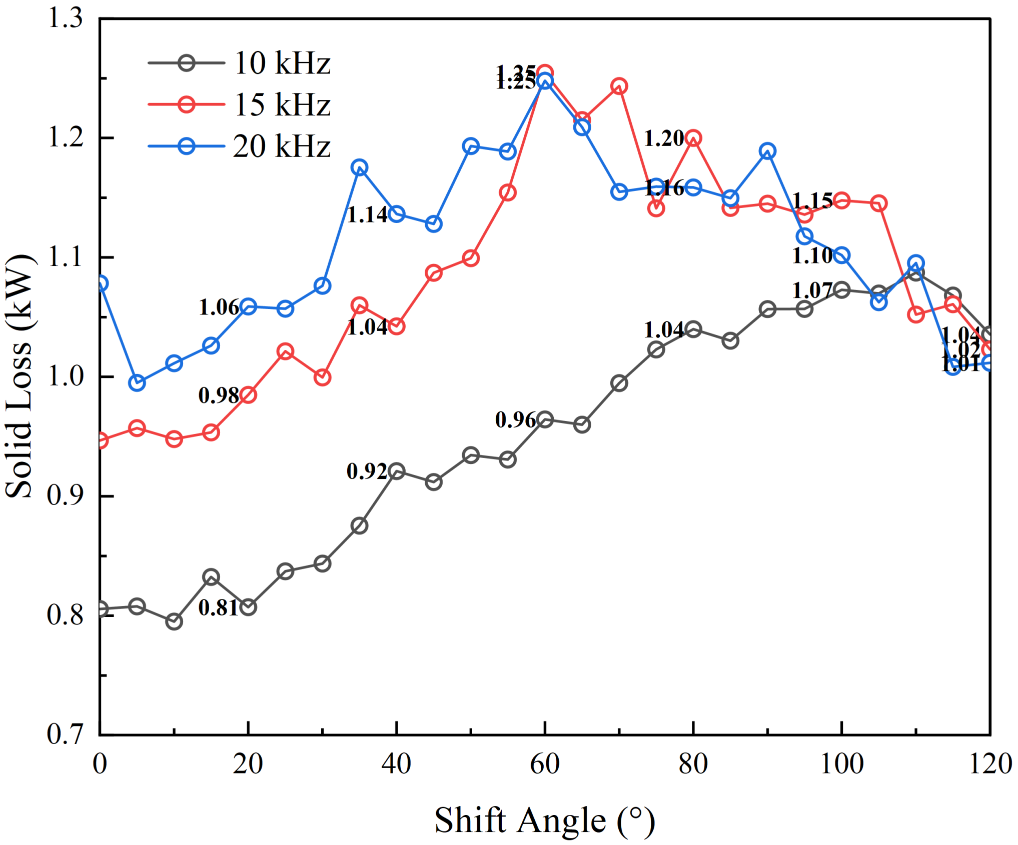

Figure 4.17: Simplorer-based Co-Simulation—Solid loss vs. shift angle

Solid loss primarily originates from eddy current losses in the conductive components of the structure or the surface layer of the iron core. As shown in the figure, there is a slight upward trend as the phase angle increases. It reaches a minimum at 10 kHz and a maximum at 20 kHz. Since eddy current losses are proportional to the square of the frequency, an increased frequency intensifies the induced current density within conductors, consequently elevating solid losses. Additionally, although the average magnetic flux distribution stabilises as the phase angle increases, periodic circulating currents persist within localised conductors, resulting in minor energy dissipation[40].

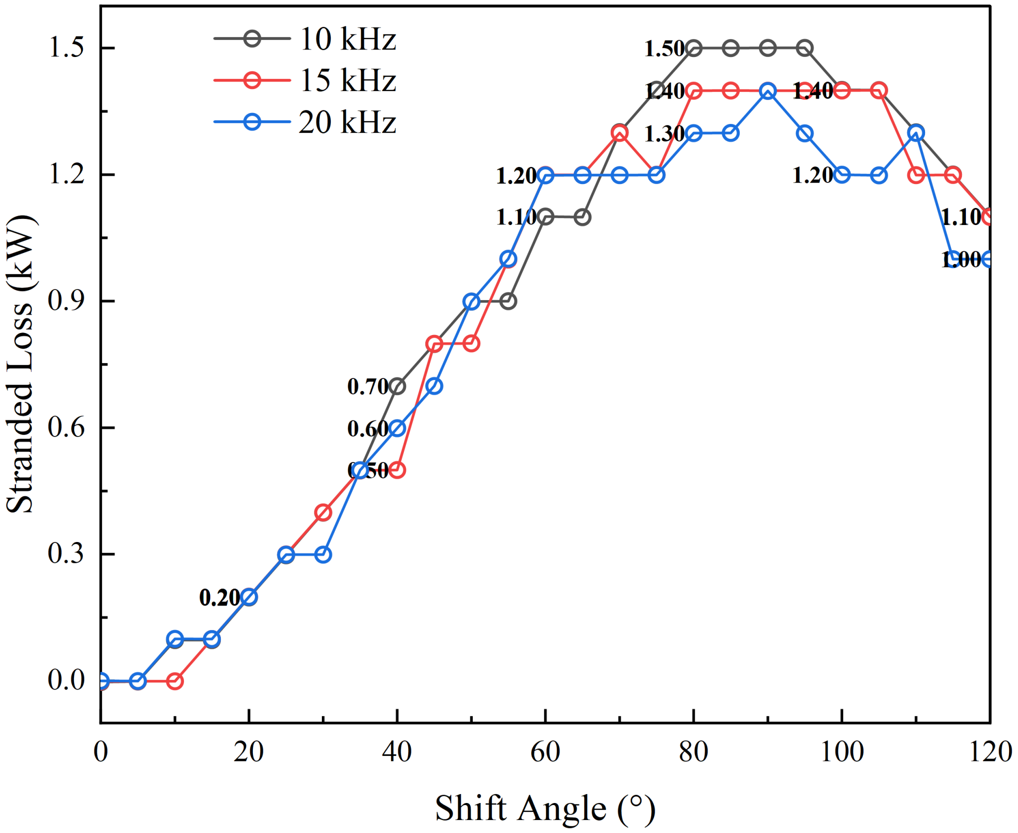

Figure 4.18: Simplorer-based Co-Simulation—Stranded loss vs. shift angle

Similar to solid losses, stranded losses exhibit an upward trend, but with a more pronounced magnitude. This is primarily due to the intensification of the skin and proximity effects within copper conductors as frequency increases. At small phase angles, the PWM waveforms of each phase overlap significantly, resulting in a relatively uniform current distribution within the conductor. However, as the phase angle increases, the peak phase currents rise slightly and the interaction between the local magnetic fields intensifies, causing the current density near the conductor surface to increase[41].

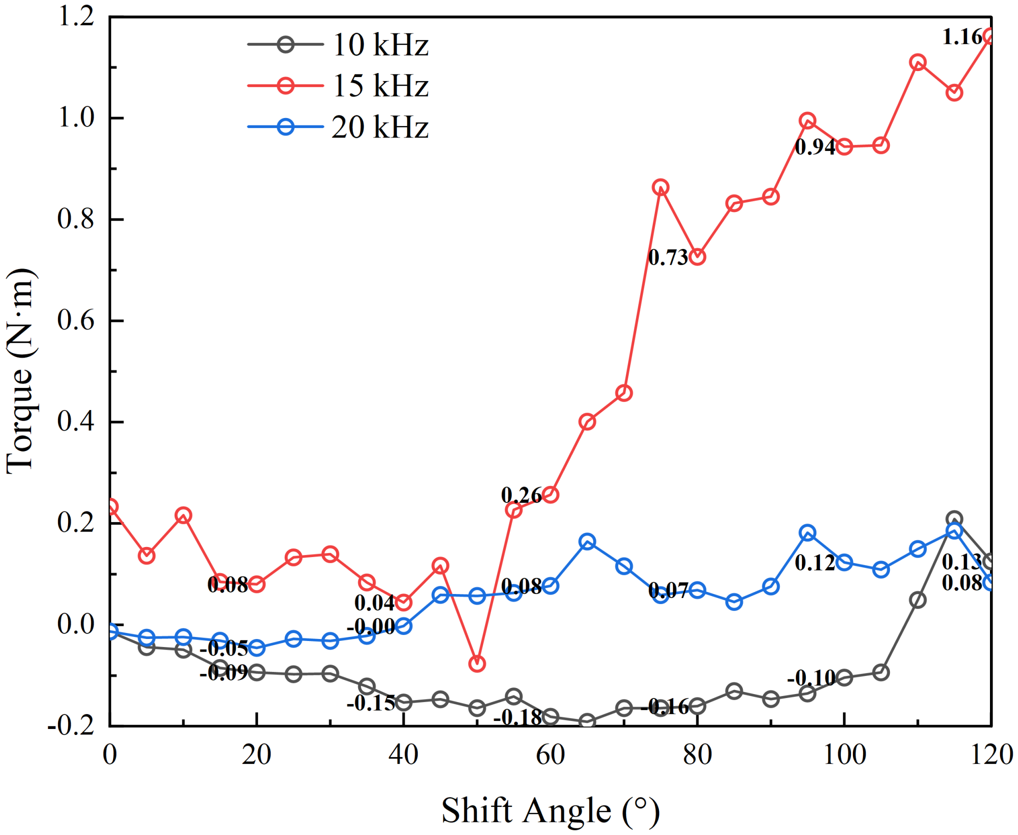

Figure 4.19: Simplorer-based Co-Simulation—Electromagnetic torque vs. shift angle

Overall, electromagnetic torque exhibits an upward trend with increasing phase shift angle, most notably at 15 kHz. There are significant fluctuations at 10 kHz, while the curve becomes smoother at 20 kHz. As the phase shift angle increases, the staggered carrier phase causes the average value of the three-phase voltage composite waveform to rise. This increases the equivalent output power, thereby delivering higher average torque. Conversely, reduced phase shift mitigates harmonic current interference, suppressing electromagnetic torque pulsation and resulting in a more stable torque output[17].

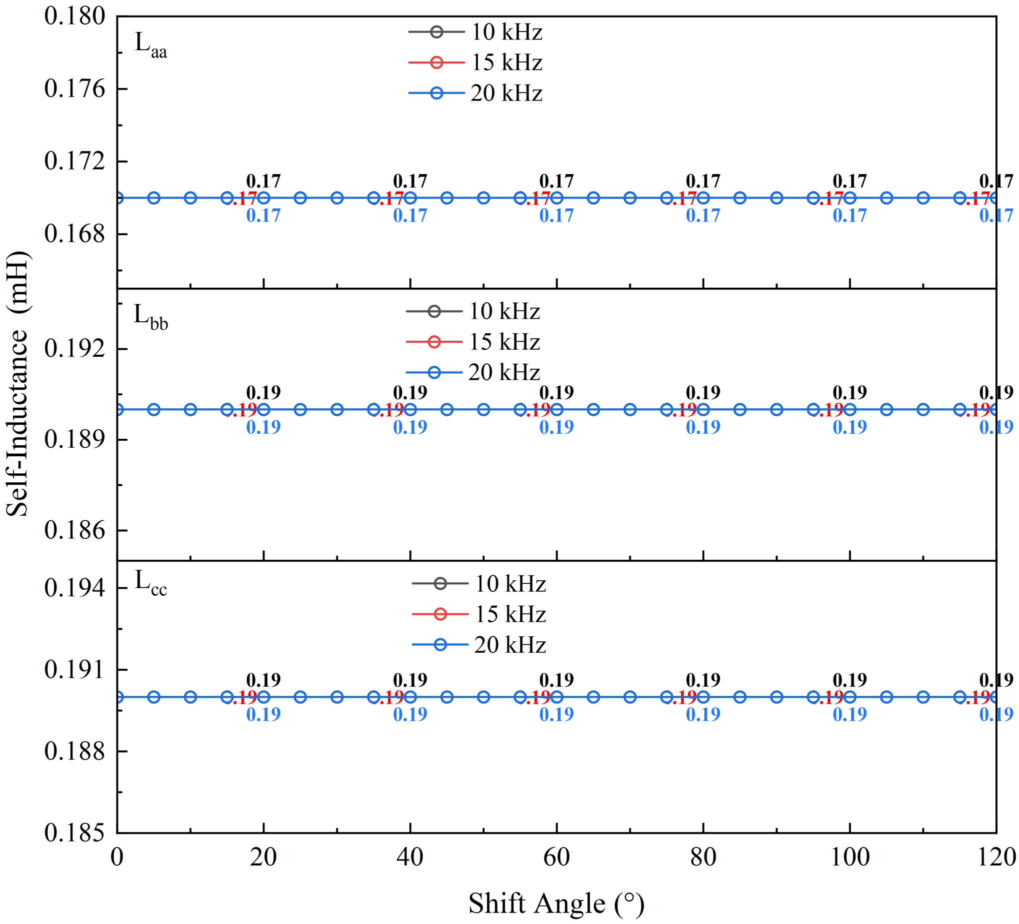

Figure 4.20: Simplorer-based Co-Simulation—Self inductances vs. shift angle

The self-inductances L_{aa}, L_{bb}, and L_{cc} exhibit minimal variation with respect to the phase angle, fluctuating only on the order of 10^{-4}. The three frequency curves completely coincide at this level.

Self-inductance is primarily determined by the stator winding structure and the magnetic circuit of the air gap. Since PWM modulation does not alter the geometric or magnetic reluctance characteristics, its value remains almost constant.

Furthermore, the stability of self-inductance across different frequencies indicates that there is no significant magnetic saturation or numerical coupling error in the system. This result validates the accuracy of the finite element model and physically demonstrates that the motor's inductance parameters maintain steady-state characteristics under PWM phase-shift conditions. Consequently, this stability facilitates precise current control and ensures a consistent dynamic response of the system[42].

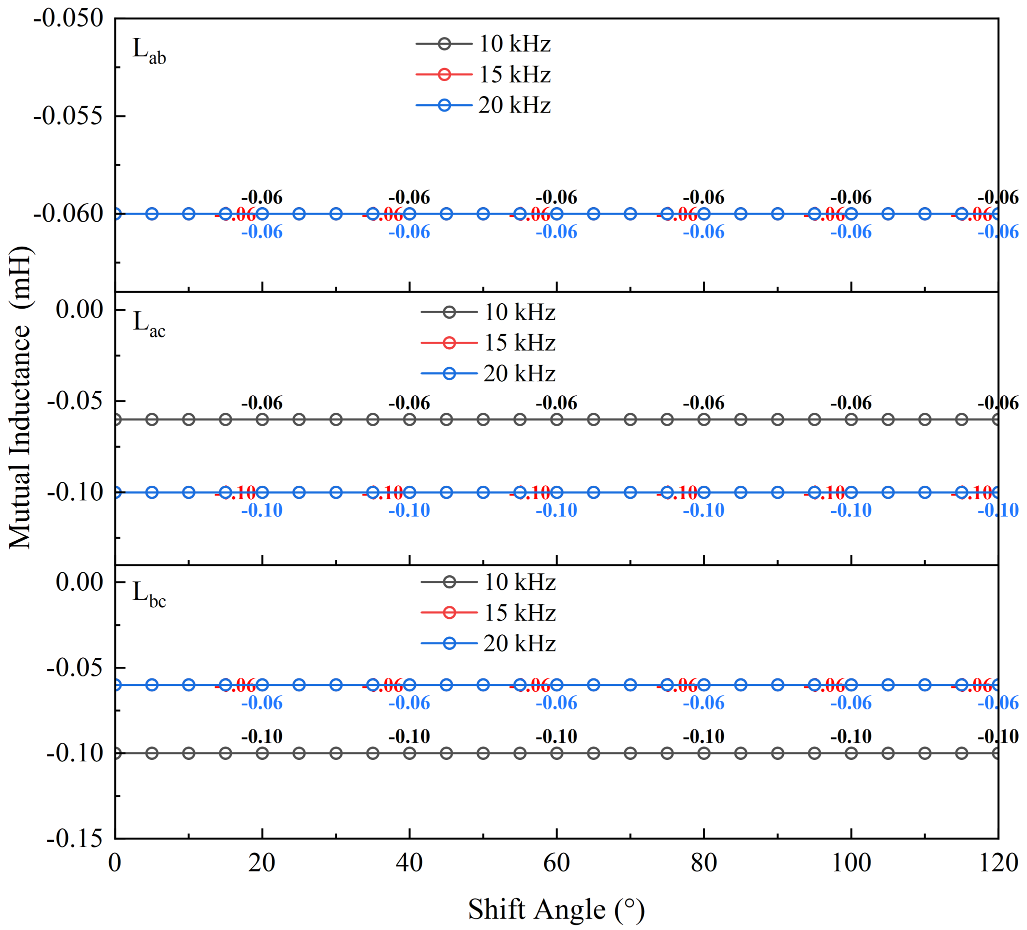

Figure 4.21: Simplorer-based Co-Simulation—Mutual inductances vs. shift angle

The mutual inductances L_{ab}, L_{ac}, and L_{bc} remain nearly constant within the phase shift angle range, stabilising at values of approximately -0.06 mH to -0.10 mH. This indicates that phase-shift modulation does not affect the motor's geometric magnetic coupling characteristics, and that the magnetic circuit structure remains linear across different frequencies and modulation angles.

PWM phase-shift modulation primarily influences the electrical excitation in the time domain rather than altering the spatial distribution of magnetic flux[43].

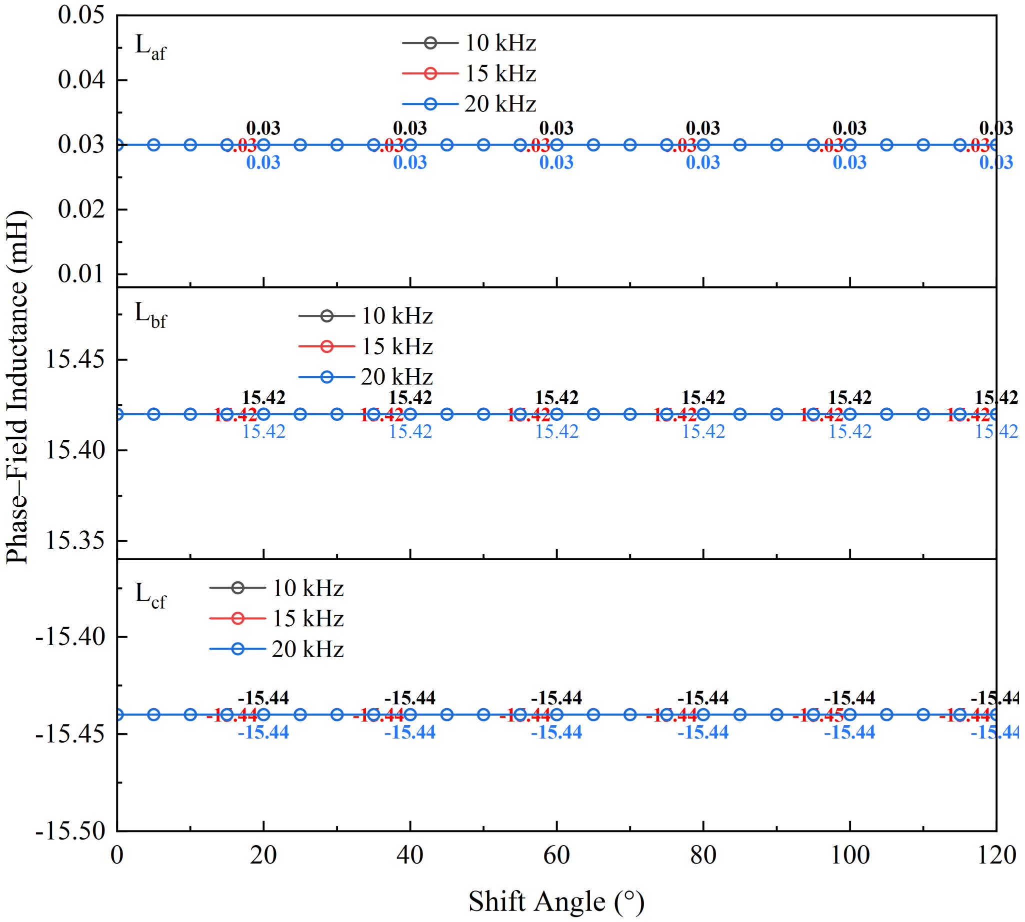

Figure 4.22: Simplorer-based Co-Simulation—Phase—Field inductances vs. shift angle

The mutual inductances between the phase and excitation windings, namely L_{af}, L_{bf}, and L_{cf}, remain stable under varying phase shift angles, with frequency curves that almost completely overlap. This suggests that the magnetic flux in the excitation winding is largely unaffected by PWM modulation.

The excitation field is dominated by DC current, and there is no significant magnetic saturation or nonlinear deviation observed in the magnetic circuit. Minor discrepancies among different frequencies can be attributed to slight phase errors in the numerical solutions of the electromagnetic field, which remain within acceptable limits[44].

4.2.2 Rotor Position

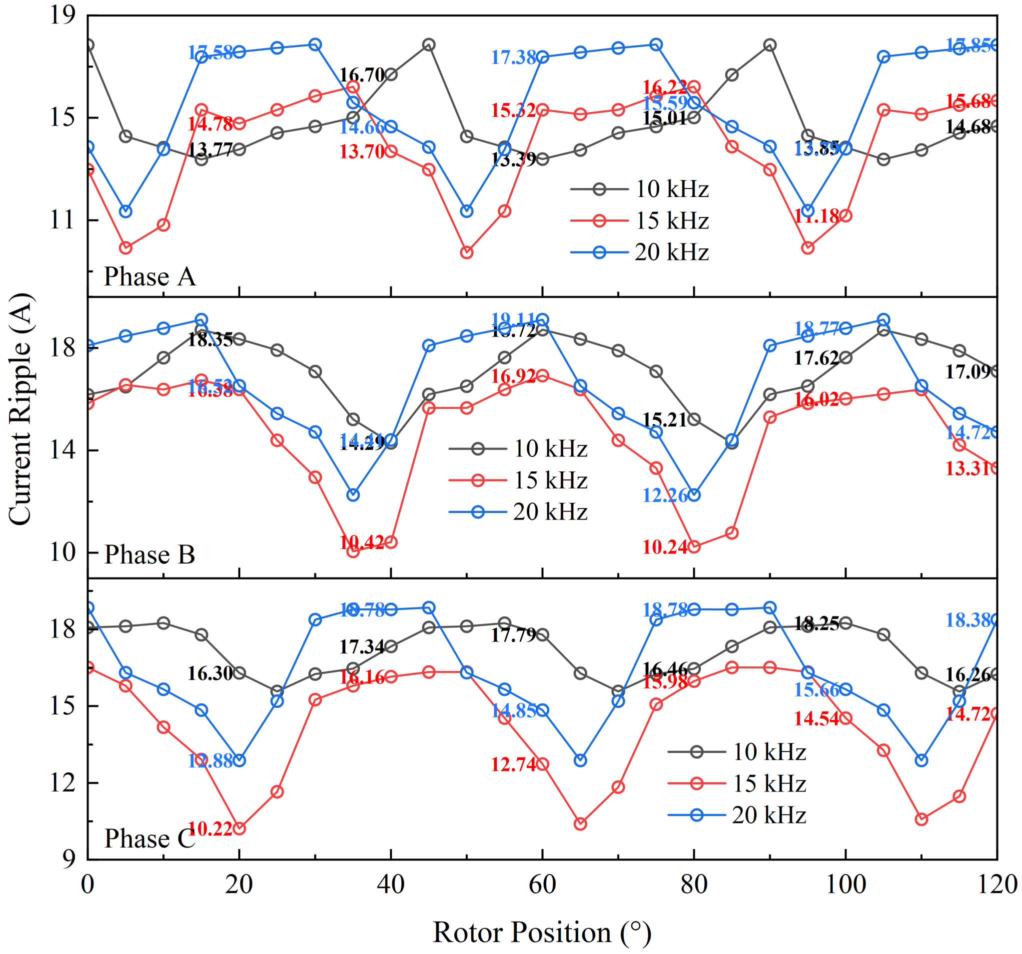

Figure 4.23: Simplorer-based Co-Simulation—Phase current ripple vs. rotor position

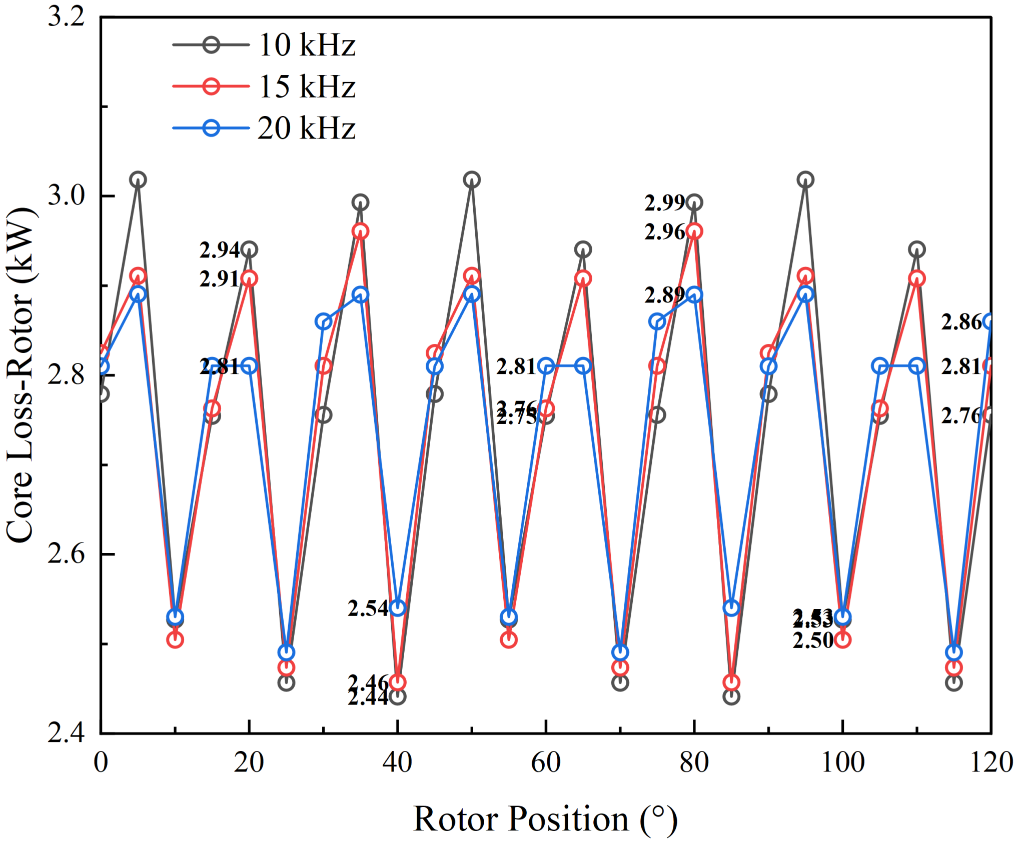

Figure 4.24: Simplorer-based Co-Simulation—Rotor core losses vs. rotor position

Rotor iron loss exhibits distinct periodic fluctuations with rotor position, with peaks and troughs appearing approximately every 20–30°. This reflects the periodic variation in magnetic flux when the rotor teeth engage with the stator slots. When the rotor and stator teeth are aligned, the magnetic flux density increases and iron losses rise; conversely, when the teeth are misaligned, the local magnetic flux weakens and iron losses fall. The curve shapes at all three frequencies are similar, with minimal variation in the average values. This indicates that the losses in the rotor core primarily depend on the spatial distribution of the magnetic field, rather than the PWM frequency. The magnetic field in the rotor region changes relatively slowly, resulting in lower, more stable loss amplitudes[45].

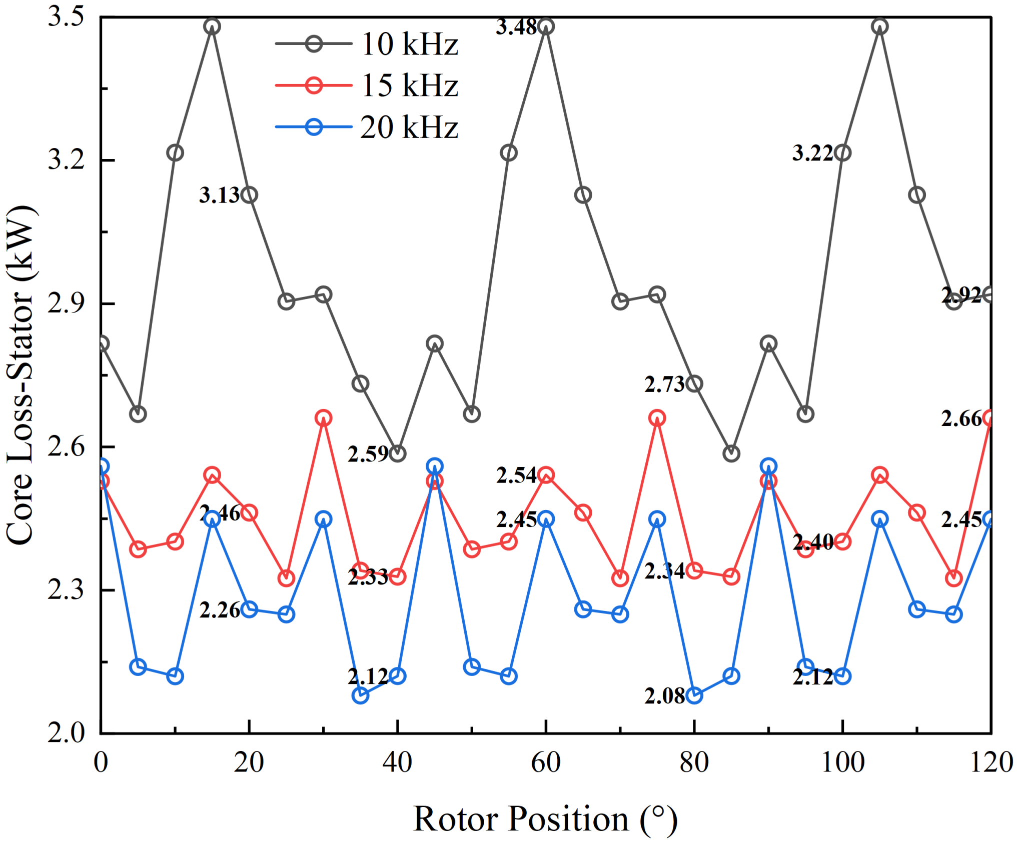

Figure 4.25: Simplorer-based Co-Simulation—Stator core losses vs. rotor position

The amplitude of the fluctuation of stator iron losses is significantly larger than that of the rotor. Its periodic peaks and troughs correspond to the alternating concentration and dispersion of the magnetic flux when the rotor slots pass through the stator teeth[46]. As the rotor position changes, the local magnetic flux density varies periodically, causing corresponding fluctuations in the iron losses of the stator yoke and teeth. While the loss levels exhibit slight differences at different frequencies, the overall trend remains consistent, indicating that stator iron losses are primarily determined by the spatial magnetic field distribution rather than carrier parameters. From a spatial perspective, the stator iron loss curve reflects the non-uniformity of the magnetic flux density within the air gap, which is directly related to the structure of the tooth slots.

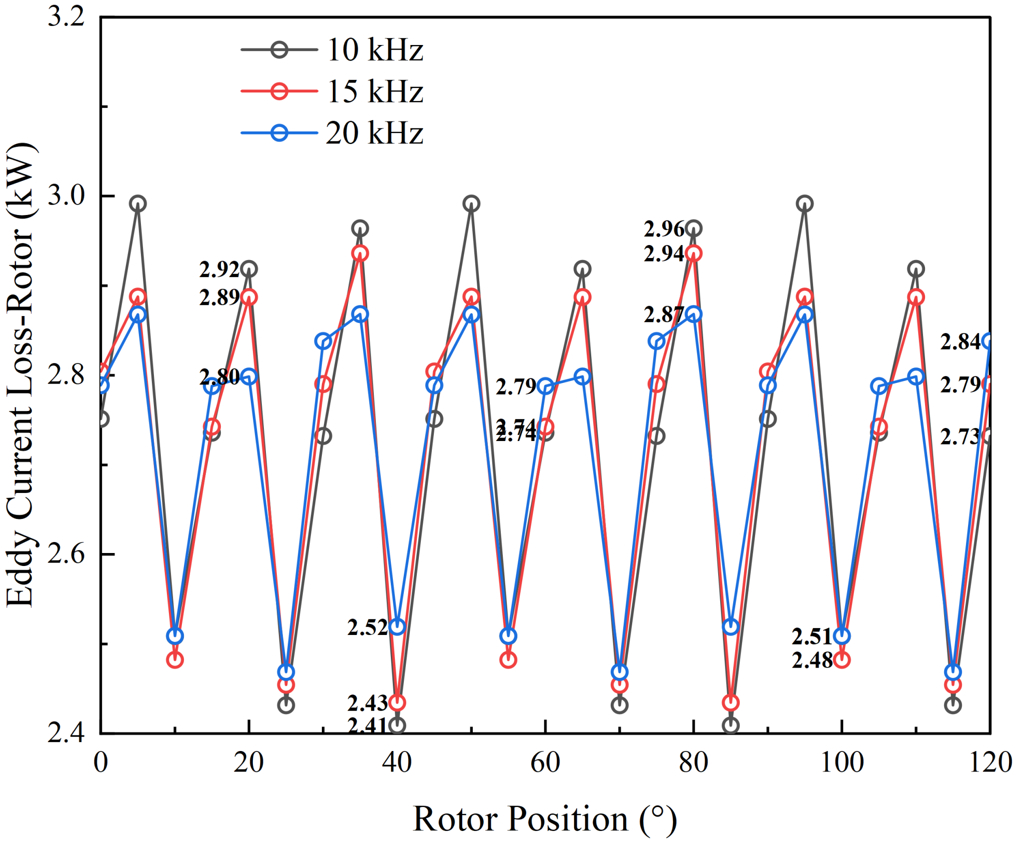

Figure 4.26: Simplorer-based Co-Simulation—Rotor eddy losses vs. rotor position

The eddy current losses in the rotor show periodic fluctuations, with peak positions that are largely consistent with those of the rotor iron losses[47]. These losses fluctuate in line with variations in the rotor slot magnetic field, though their overall amplitude remains relatively small. Due to the thin conductor layer in the rotor and the skin effect that limits the depth of current penetration, eddy currents are primarily confined to the surface region. Consequently, the spatial variation is primarily determined by the distribution of the magnetic flux rather than the frequency[48]. This indicates that energy dissipation within the rotor is dominated by structural periodicity and is only weakly correlated to the form of electrical excitation.

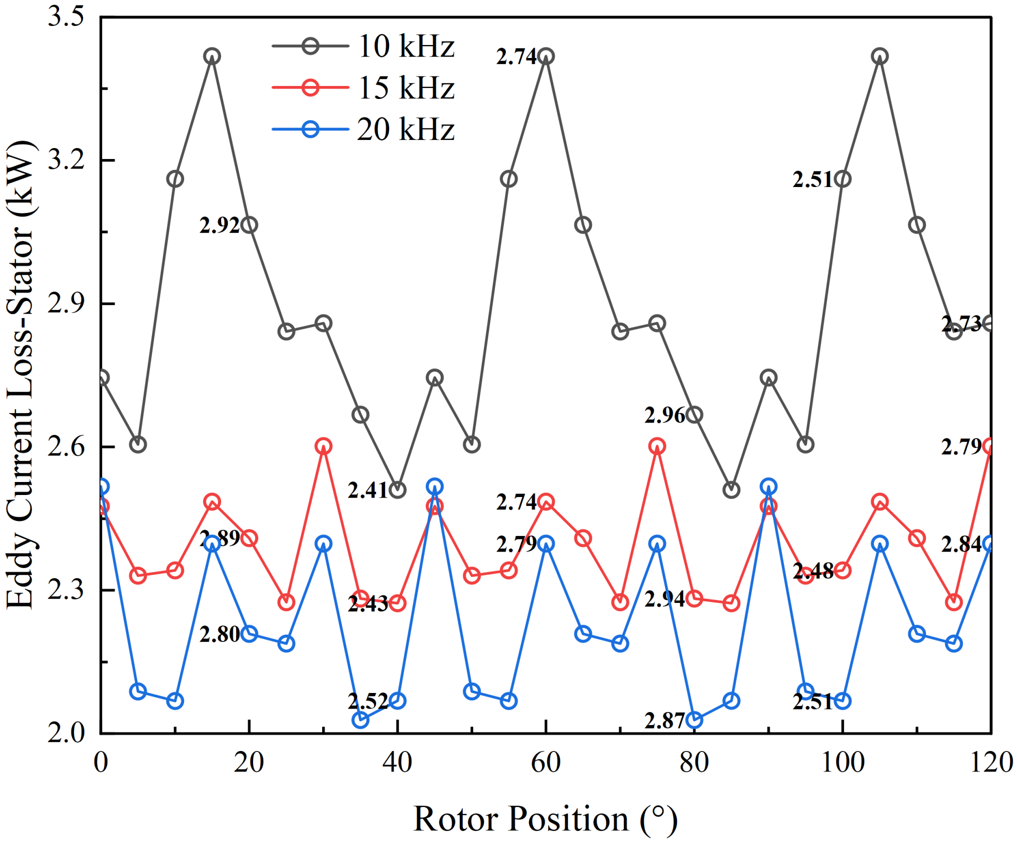

Figure 4.27: Simplorer-based Co-Simulation—Stator eddy losses vs. rotor position

Stator eddy current losses demonstrate spatial periodicity in relation to rotor position, though their amplitude is found to be considerably higher in comparison to that of the rotor portion. When the rotor slots align with the stator teeth, the air gap magnetic flux density increases, thereby enhancing the induced current at the stator tooth tips and consequently raising eddy current losses. In the event of a misalignment of the tooth-slot alignment, the magnetic flux disperses more uniformly, thereby reducing losses. This variation is indicative of the influence of the magnetic field's spatial distribution, with stator eddy current losses being primarily determined by the local rate of change in magnetic flux density. This, in turn, is closely related to the mechanical angle of the rotor[47].

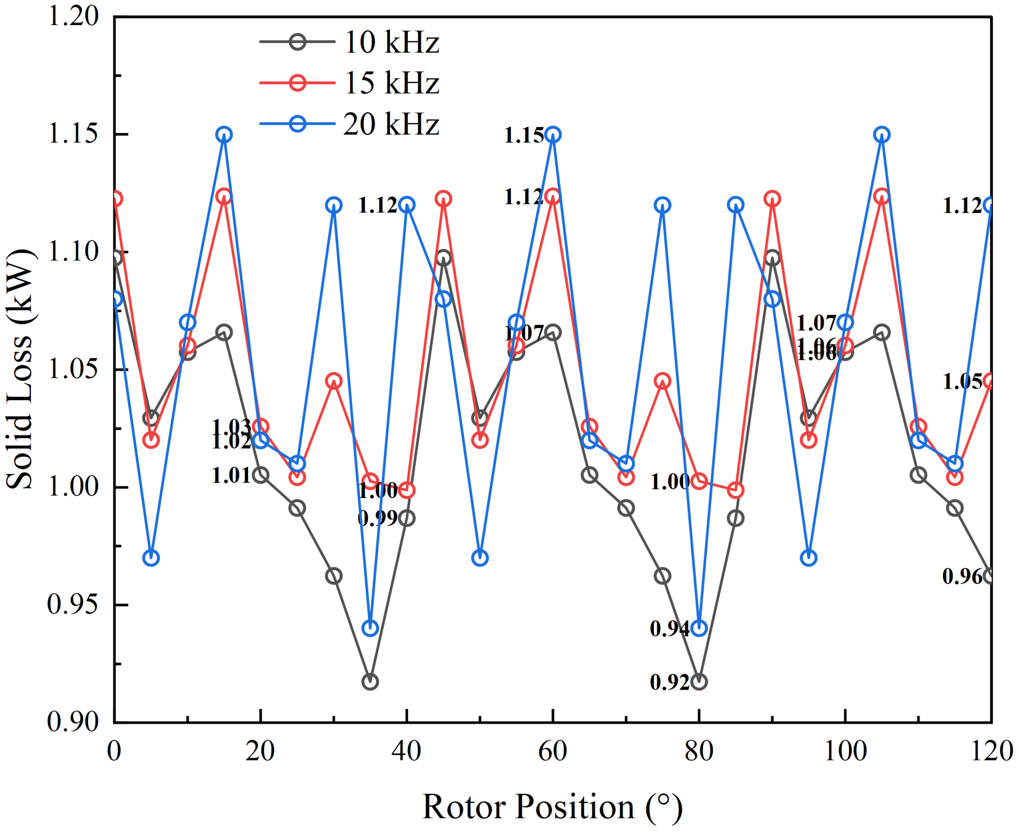

Figure 4.28: Simplorer-based Co-Simulation—Solid loss vs. rotor position

Solid loss varies minimally across the entire rotor position range. This finding suggests that the losses in DC resistance experienced by armature conductors and structural components are largely impervious to spatial variations in magnetic field[49]. It is evident that minor fluctuations arise from induction effects caused by current ripple, coupled with transient magnetic flux. In summary, the solid loss is a stable background loss in this simulation scenario and is not a primary energy component[50].

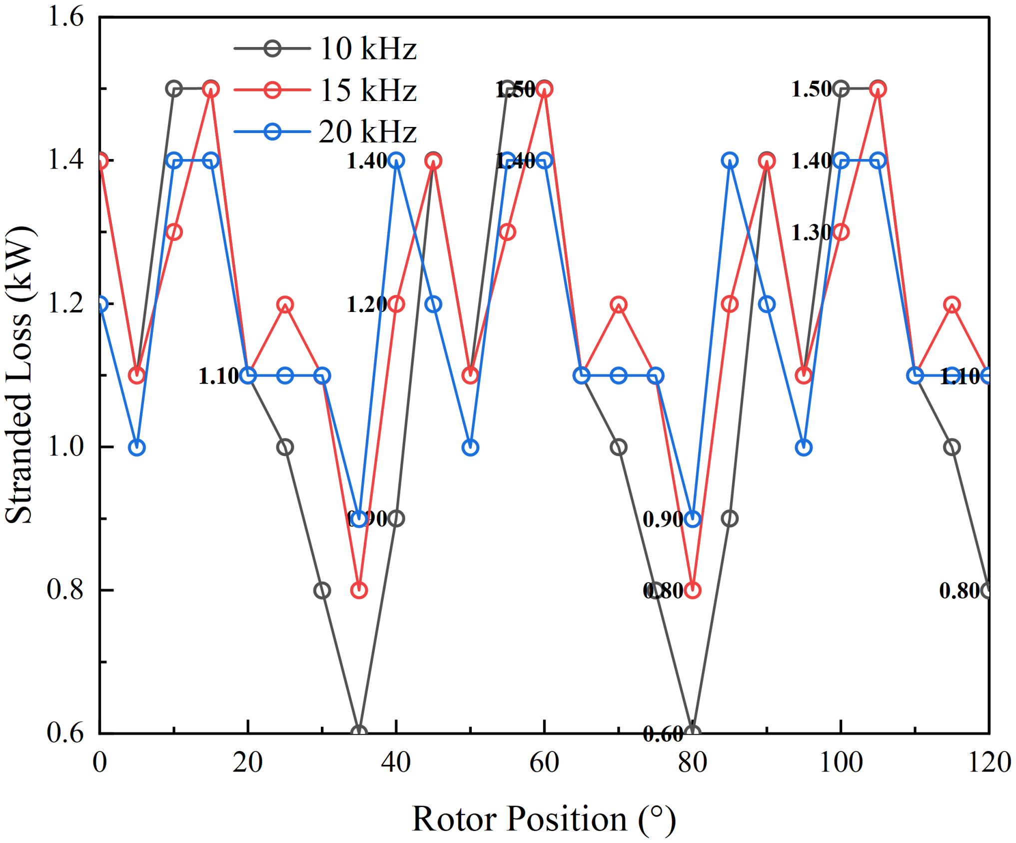

Figure 4.29: Simplorer-based Co-Simulation—Stranded loss vs. rotor position

The stranded loss also varies periodically with rotor position[51]. stranded losses are expected to increase with switching frequency. This is due to the fact that a higher f_s intensifies the non-uniform current distribution within the conductors. However, the results of the simulation indicate that the influence of frequency is less significant than that predicted by theory. The reason for this can be attributed to the fact that the spatial flux distribution and rotor alignment dominate the local current density pattern in the windings, thereby partially compensating for the frequency effect. When the rotor magnetic field is strongly coupled to a given phase, the local eddy current and proximity effects become more pronounced, leading to peaks in the stranded loss curve. Conversely, when the magnetic coupling weakens, these effects diminish. Consequently, the stranded loss variation is indicative of an interplay between frequency-dependent conductor effects and position-dependent magnetic coupling, rather than a purely frequency-driven relationship.

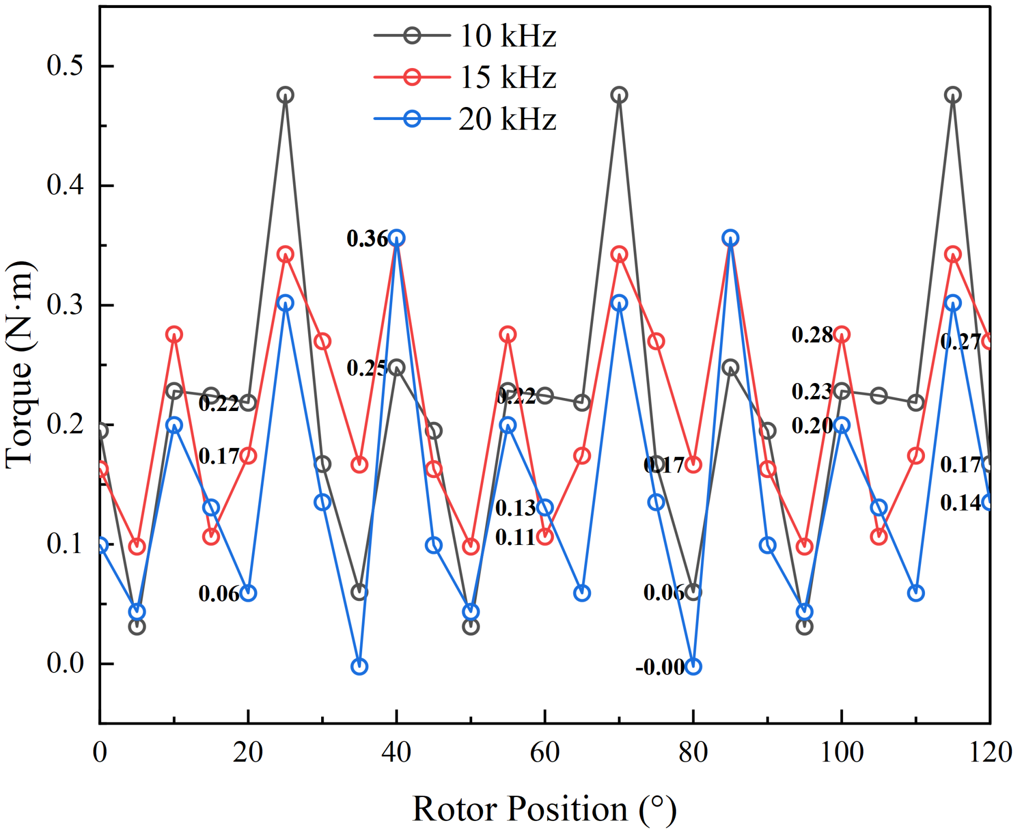

Figure 4.30: Simplorer-based Co-Simulation—Electromagnetic torque vs. rotor position

Electromagnetic torque has been observed to exhibit periodic pulsations along the rotor position, with fluctuations in the cycle being found to be correlated to the motor's slot-pole alignment[52]. When the rotor teeth are aligned with the stator slots, the magnetic pull reaches its peak, resulting in an increase in torque. Conversely, when the rotor teeth are misaligned, the magnetic attraction weakens, leading to a decrease in torque. This fluctuation, known as cogging torque, arises from the motor's inherent structural characteristics and is independent of carrier frequency or PWM modulation. It has been demonstrated that, despite the fact that an increase in frequency can result in a slight smoothing of current distribution, torque pulsation is primarily determined by the geometric magnetic circuit[53].

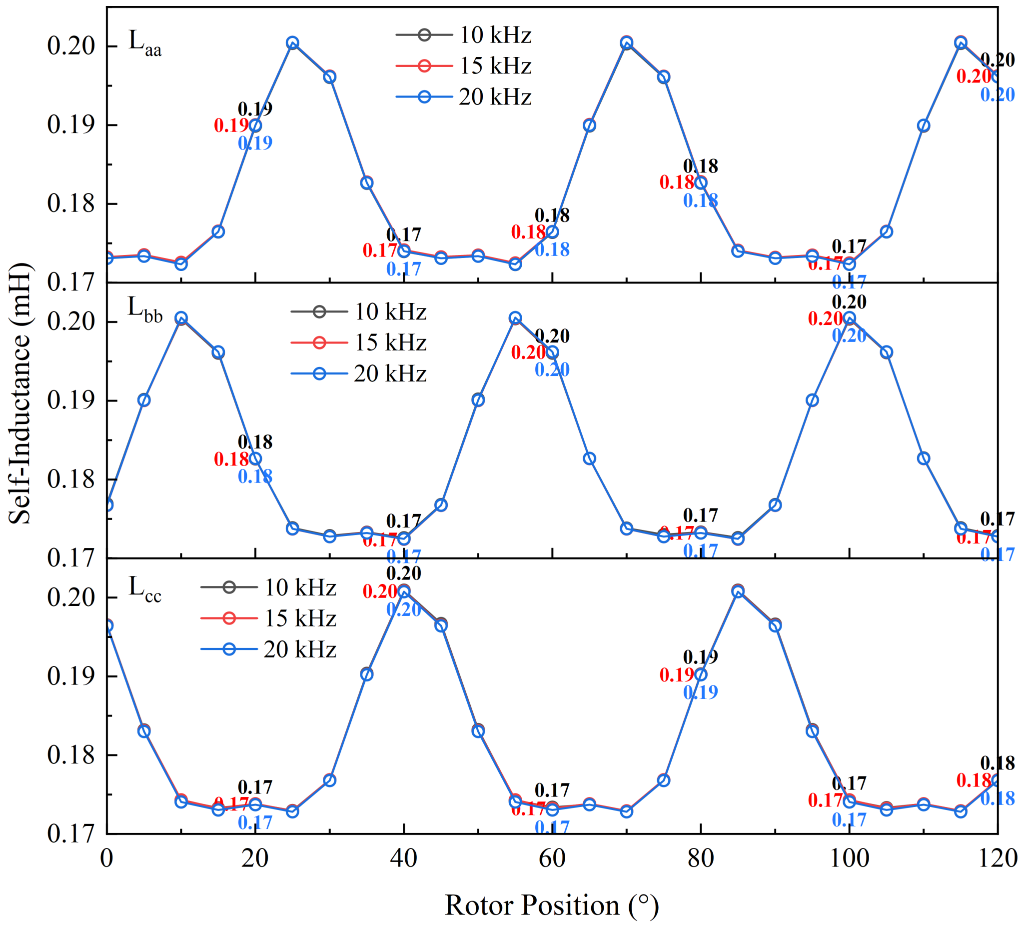

Figure 4.31: Simplorer-based Co-Simulation—Self inductances vs. rotor position

The self-inductances (L_{aa}, L_{bb}, and L_{cc}) exhibit a clear periodic variation with respect to rotor position. As the rotor teeth pass the stator slots, the airgap reluctance changes periodically, causing the self-inductance of each phase to fluctuate between maximum and minimum values. When the rotor teeth align with the stator teeth of a given phase, the magnetic path is reduced and the flux linkage is maximised, resulting in the highest inductance. Conversely, when the rotor teeth move away from alignment, the leakage flux increases and the inductance decreases. It is evident that each phase is shifted by 120° in electrical angle, thereby ensuring the maintenance of a balanced and symmetrical magnetic configuration. The periodic nature of the inductance curves is indicative of the influence of slot–pole geometry on the spatial distribution of magnetic permeance, while the amplitude consistency across frequencies confirms that time-domain modulation has negligible influence on magnetic structure[53].

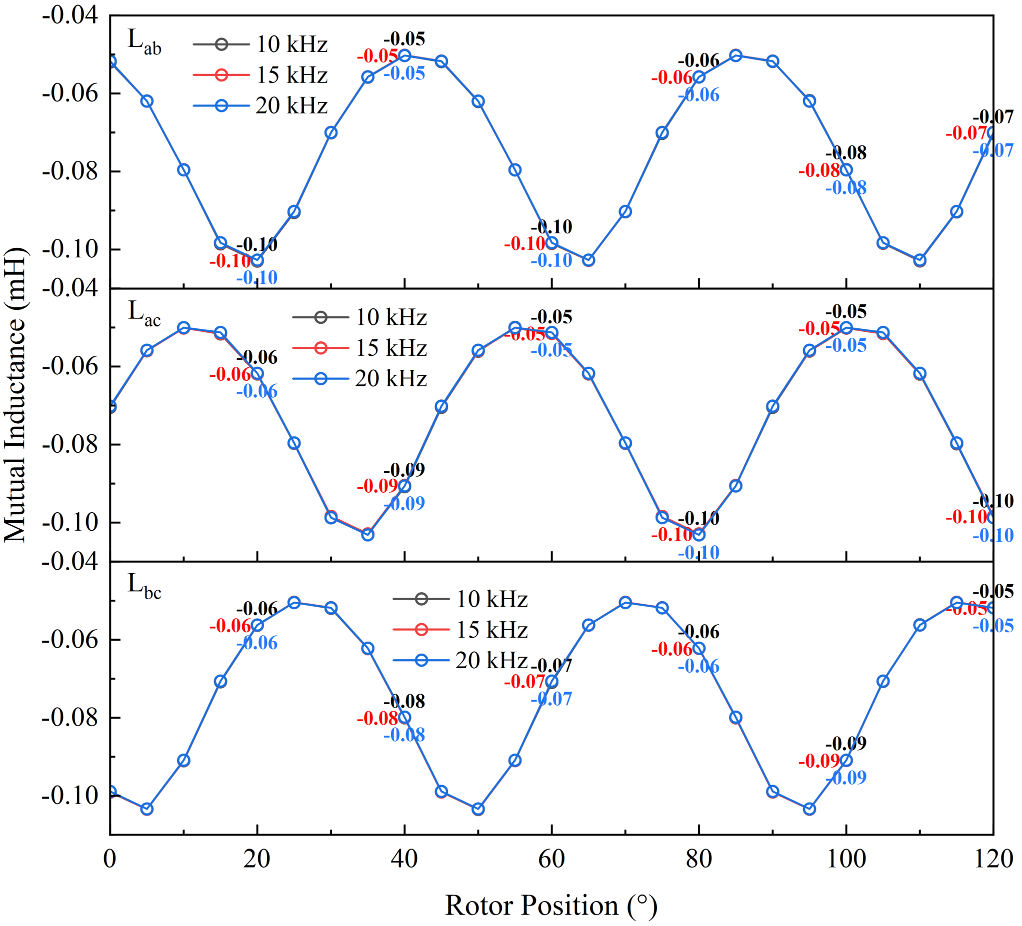

Figure 4.32: Simplorer-based Co-Simulation—Mutual inductances vs. rotor position

The mutual inductances (L_{ab}, L_{ac}, and L_{bc}) also vary periodically with rotor position, but their phase is opposite to that of the self-inductances[52]. When one pair of phases (e.g. A–B) exhibits strong magnetic coupling, the remaining pairs demonstrate relatively weak coupling, thereby ensuring the preservation of magnetic energy equilibrium within the system comprised of three phases. The variation pattern is derived from the alternating magnetic coupling among the stator windings as the rotor position is altered, resulting in a modification of the spatial flux distribution. The overall magnitude of mutual inductance is much smaller than that of the self-inductance, and the curves remain nearly identical for all tested frequencies (10 kHz, 15 kHz, and 20 kHz). This demonstrates that rotor motion primarily affects spatial magnetic coupling, while PWM frequency and carrier phase-shift have minimal effect on the magnetic path geometry[53].

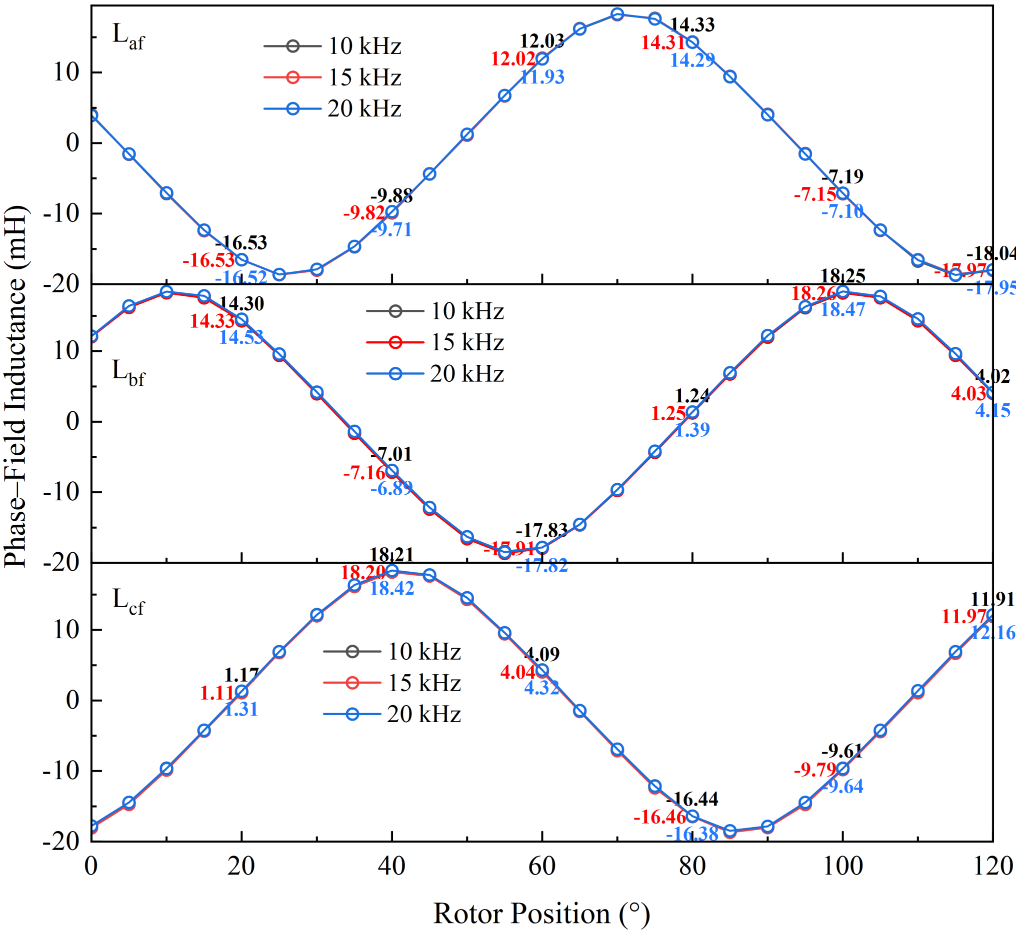

Figure 4.33: Simplorer-based Co-Simulation—Phase—Field inductances vs. rotor position

The phase–field inductances (L_{af}, L_{bf}, and L_{cf}) exhibit smooth periodic variations with rotor position, reflecting the alternating magnetic coupling between the excitation winding and each stator phase[54]. When the rotor magnetic pole is aligned with a phase winding, the coupling is strongest and the corresponding inductance reaches its maximum; as the pole moves away, the coupling weakens and the inductance decreases. The periodicity of these inductances corresponds to the rotor pole pitch and remains stable across different frequencies. This suggests that the magnetic flux linkage between the excitation and armature windings is principally governed by spatial alignment, as opposed to time-domain modulation.

In summary, the overall results of the Simplorer-based co-simulation largely align with theoretical expectations. This is to say that core losses and eddy current losses decrease with increasing frequency, while current ripple and torque ripple exhibit the anticipated modulation trends[55]. However, the influence of switching frequency on several parameters remains indistinct, and quantities such as current ripple and interleaved losses do not exhibit the linear frequency dependence predicted by analytical models[56]. This limitation is primarily attributable to Simplorer's utilisation of a simplified circuit representation and a reduced time resolution, which collectively fail to adequately capture the intricate current waveform distortions induced by high-frequency PWM excitation.

4.3 Simulink-based System Simulation

During the co-simulation stage, the system model was implemented using Simplorer and coupled directly with the Maxwell finite element solver. Although this framework enables bidirectional interaction between circuit dynamics and electromagnetic fields, it also makes the overall simulation highly sensitive to numerical stability. In particular, the presence of high-frequency switching and rapidly varying excitation requires a significantly smaller timestep to maintain accuracy. However, reducing the timestep leads to a drastic increase in computational time, making long-duration co-simulations impractical.

To overcome these limitations, the system-level modelling was migrated from Simplorer to the Simulink environment[55]. Simulink allows more flexible and efficient construction of converter and control models, enabling the generation of realistic, high-resolution, frequency-dependent current waveforms. These waveforms are subsequently imported into the Maxwell model, ensuring accurate electromagnetic excitation while avoiding the instability and excessive computation time associated with full co-simulation.

4.3.1 Shift Angle

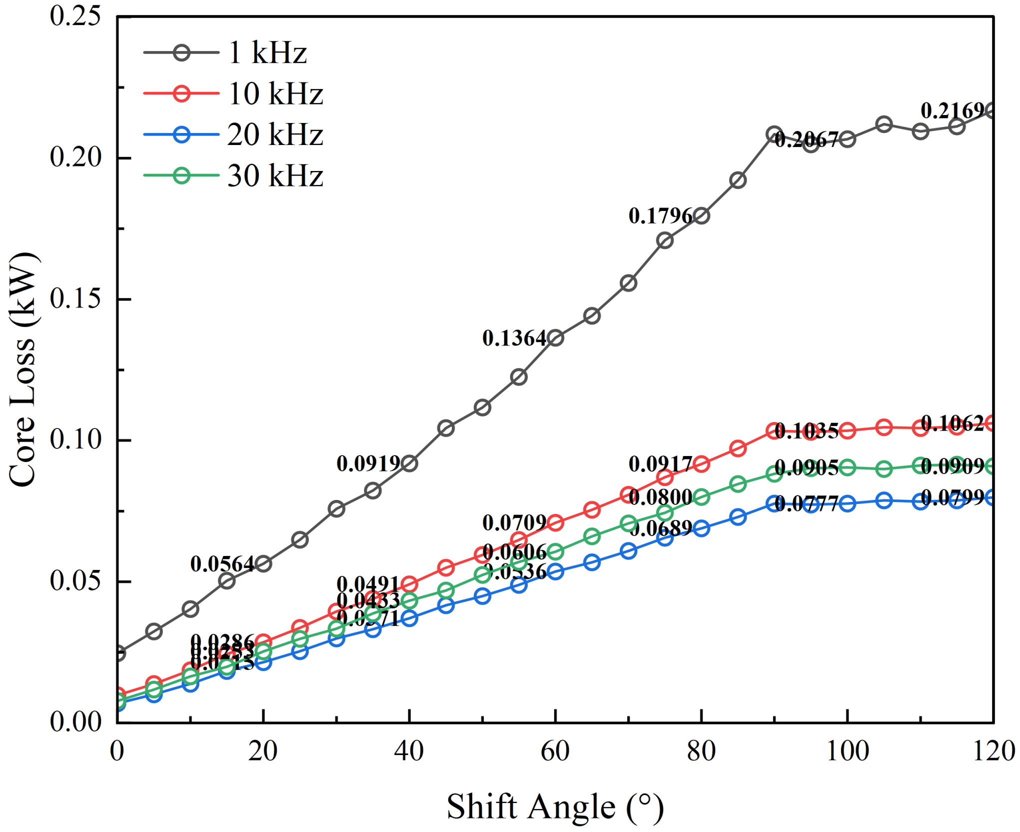

Figure 4.34: Simulink: core losses vs. shift angle

As the results show, stator core loss increases significantly with phase-shift angle, exhibiting approximately linear growth across all frequencies[57]. Compared with the Simplorer-based results, the Simulink–Maxwell co-simulation more clearly reveals the influence of the switching frequency on loss characteristics. At 1 kHz, the core loss is at its maximum, and decreases notably as the carrier frequency increases from 10 kHz to 30 kHz, with smooth, well-separated curves. This consistent trend indicates that the current waveforms generated in Simulink contain realistic PWM harmonic and phase characteristics, enabling the Maxwell model to accurately capture the suppression of magnetic flux variation caused by higher switching frequencies. Therefore, phase-shift modulation at a high frequency effectively reduces core losses, a relationship that is more intuitively demonstrated by the co-simulation model[58].

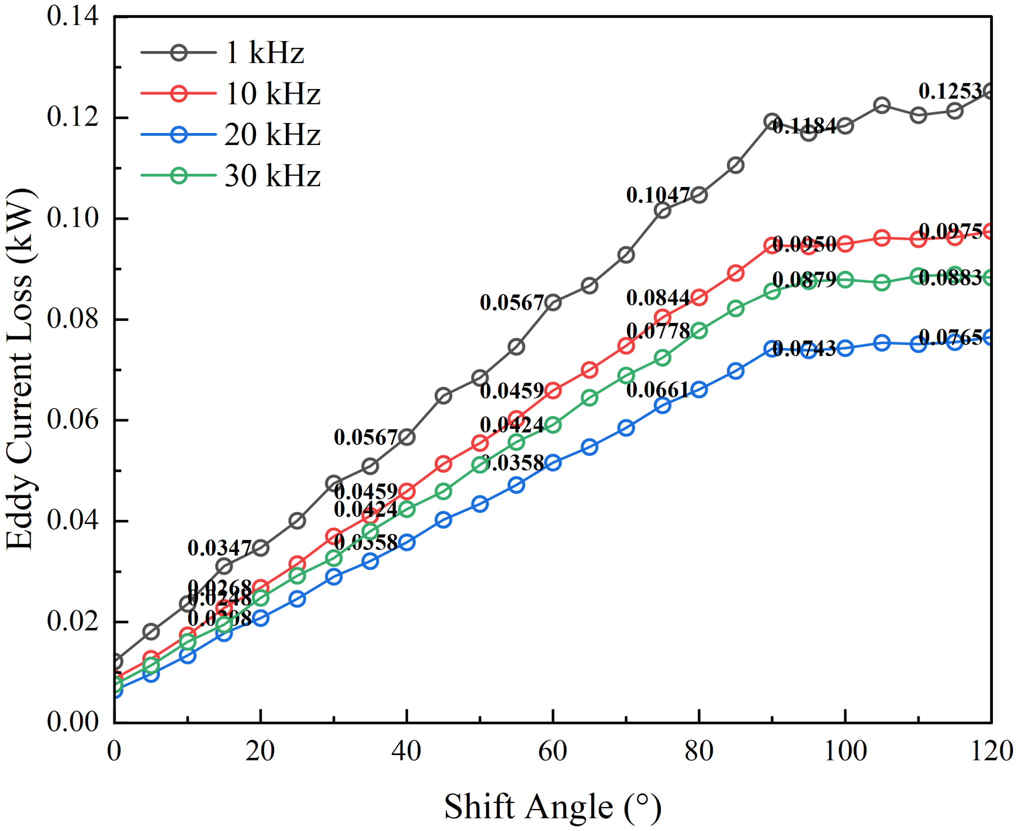

Figure 4.35: Simulink: eddy losses vs. shift angle

The eddy current loss follows a similar trend to the core loss, gradually increasing with the phase-shift angle[59]. At a low frequency of (1 kHz), the eddy current loss is at its highest and shows a steeper slope. At higher frequencies, however, it decreases and tends to flatten out. Compared with the Simplorer-based analysis, the Simulink–Maxwell results more accurately capture frequency-dependent behaviour. Since the Simulink current input incorporates the dynamic features of realistic PWM, the Maxwell solver accurately reflects the attenuation of high-frequency magnetic flux components and the reduction in the number of eddy current paths at higher frequencies. Consequently, the beneficial effect of a higher switching frequency in reducing additional iron losses is clearly evident[60].

–

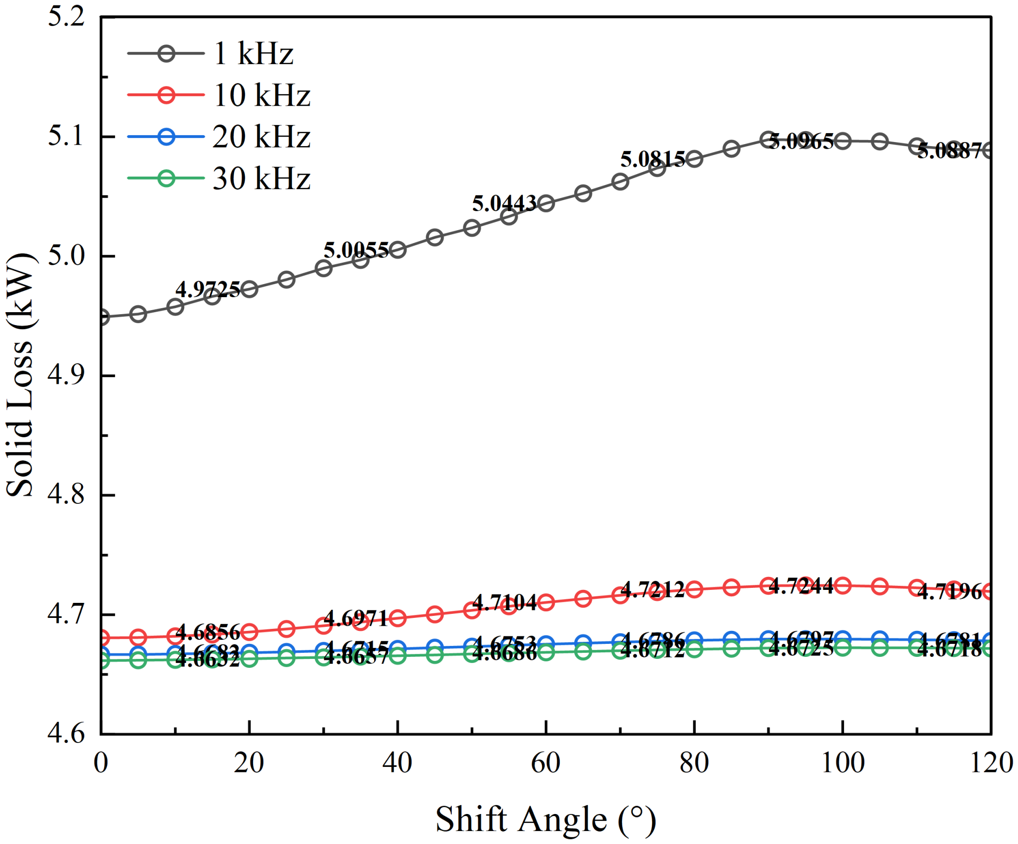

Figure 4.36: Simulink: solid losses vs. shift angle

The solid loss remains almost constant throughout the entire phase-shift range, with minimal variation[61]. The Simulink–Maxwell co-simulation produces more consistent results across different frequencies, with clearly separated yet nearly parallel curves, indicating that the solid conductor loss is primarily determined by DC resistance and is only weakly affected by carrier frequency or phase shifting. The results observed in Simplorer show slight numerical fluctuations. The present results are smooth and physically consistent. This demonstrates that the Simulink-generated current waveforms provide more realistic input for electromagnetic field computation[62]. Consequently, this model can more accurately reflect the stable nature of solid losses, offering a reliable basis for subsequent thermal analysis.

4.3.2 Shift-Angle–Dependent Field Analysis at 10 kHz

As discussed in the previous subsection, the loss–shift-angle curves show that both core loss and eddy-current loss increase almost linearly with the shift angle, whereas the solid loss is only weakly affected. To understand the physical origin of these trends, field plots were generated at four characteristic shift angles (0°, 40°, 80°, and 120°) for the same 10 kHz excitation[57]. For each case, the magnetic flux density magnitude, the corresponding B-vector pattern and the ohmic (eddy-current) loss density are analysed below.

4.3.2.1 Flux-Density Magnitude

Figure 4.37 presents the magnetic flux density distribution for different shift angles. The overall peak *B* remains in the range of 2.7–2.8 T for all cases, confirming that the shift angle variation does not significantly change the global magnetic loading of the machine[32].

At a shift angle of 0°, the three phase currents are synchronised in terms of their ripple components, leading to a highly periodic and symmetric excitation. The flux-density distribution in the teeth and yoke is almost uniform along the circumference, and local saturation is moderate.

When the shift angle is increased to 40° and 80°, the temporal staggering of the phase ripples causes the instantaneous magnetomotive force (MMF) seen by each tooth to vary more irregularly. Although the peak *B* remains similar, the spatial distribution becomes slightly less uniform, with certain teeth experiencing higher local *B* while others are relieved, which is consistent with the gradual increase of core loss observed.

At 120°, the ripple components are maximally phase-shifted and the excitation becomes more evenly spread over time. The flux-density map appears again relatively uniform, but small differences in local saturation levels remain, indicating that the shift angle mainly redistributes the ripple-induced flux rather than changing its magnitude[63].

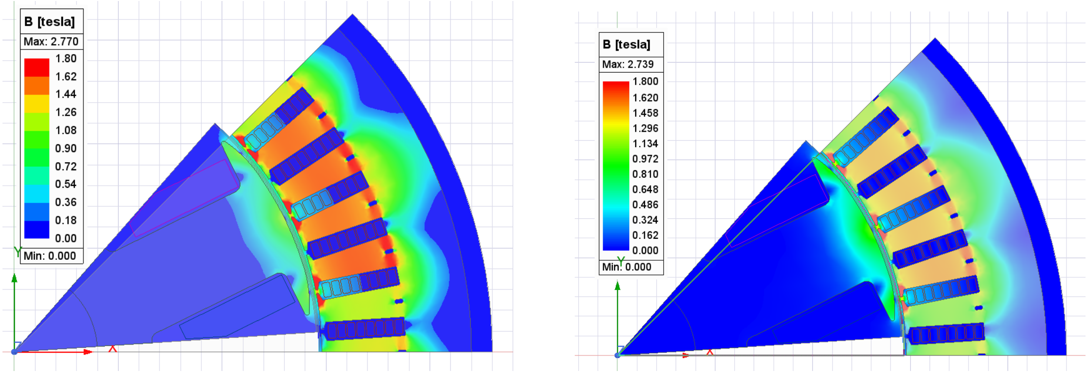

(a) Shift angle = 0° **(b)** Shift angle = 40°

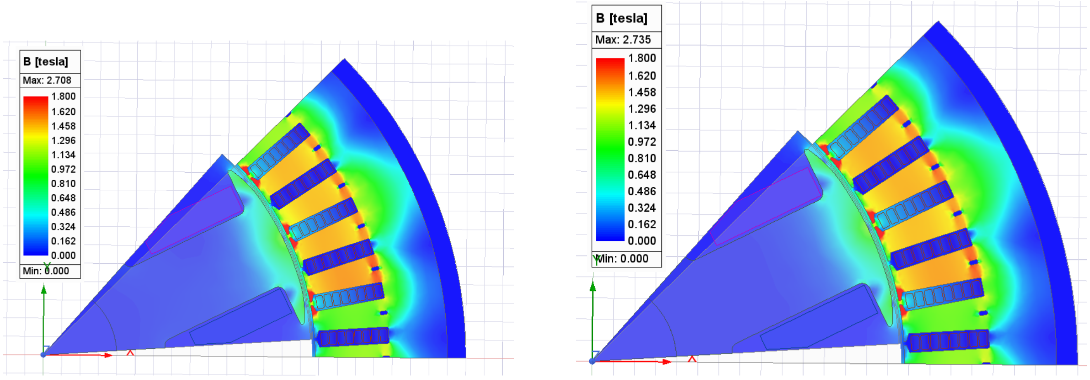

(c) Shift angle = 80° **(d)** Shift angle = 120°

Figure 4.37: Flux-density magnitude distribution at different shift angles (10 kHz).

4.3.2.2 Flux-Line Distribution under Different Shift Angles

Figure 4.38 shows the magnetic vector potential (A) contours for shift angles of 0°, 40°, 80°, and 120° at 10 kHz. All four cases exhibit almost identical flux-line patterns: the main flux loops between the stator teeth and the rotor pole remain unchanged, and the level of saturation in the teeth and yoke appears nearly identical[64]. The maximum A value stays close to 0.013 Wb/m for all shift angles. This behaviour agrees with electromagnetic theory. In this study, only the phase of the PWM carrier is shifted, while the fundamental phase currents remain unchanged. Thus, the average stator MMF and the steady-state air-gap flux density are independent of the shift angle. At any sampling instant, the instantaneous phase currents—and therefore the instantaneous flux distribution—are nearly the same for all cases. This explains why the spatial flux-line distribution is almost unaffected by the shift angle.

Although the spatial flux pattern does not change, the temporal distribution of high-frequency ripple does[58]. With larger shift angles, the ripple currents of different phases are no longer aligned in time. Different teeth reach their peak ripple flux at different instants, extending the total duration of strong $\mathrm{d}B/\mathrm{d}t$ within one switching cycle. Because eddy-current loss is approximately proportional to the time integral of $(\mathrm{d}B/\mathrm{d}t)^2$, this extended excitation results in higher average eddy-current and core losses, the increase in losses with shift angle is dominated by temporal effects rather than spatial changes[59].

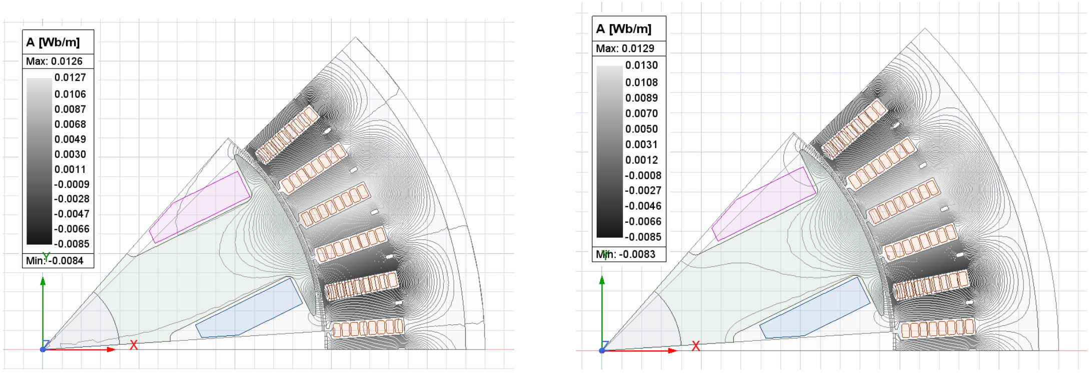

(a) Shift angle = 0°

(b) Shift angle = 40°

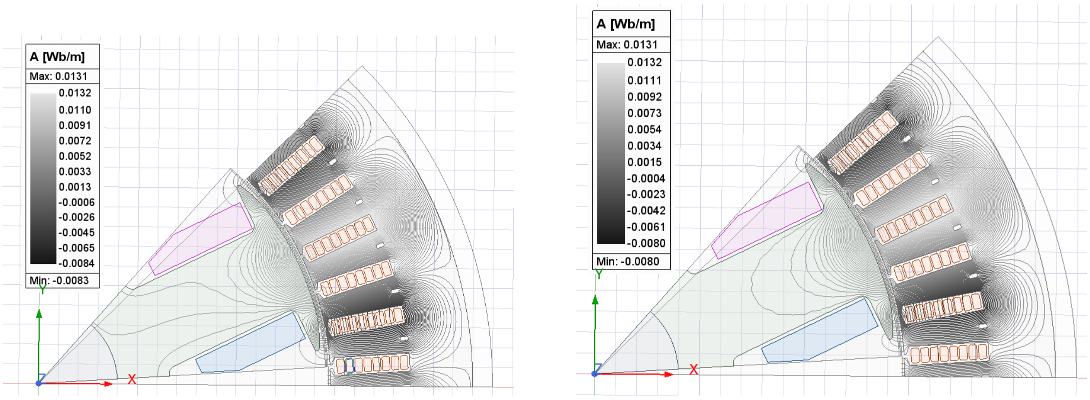

(c) Shift angle = 80°

(d) Shift angle = 120°

Figure 4.38: Flux-line (A-field) distribution at shift angles of 0°, 40°, 80°, and 120° under 10 kHz excitation.

4.3.2.3 Ohmic (Eddy-Current) Loss Density

Figure 4.39 shows the corresponding ohmic (eddy-current) loss density for the four shift angles. These plots are in good agreement with the eddy-current loss curve[60]. At 0°, loss hotspots are concentrated at the tooth tips and slot openings, but they are active only during narrow time intervals when the three-phase ripple components coincide. Consequently, the average eddy-current loss is the lowest among the considered shift angles.

At 40° and 80°, the hotspot pattern remains similar in space, but the effective duty of these hotspots over one period increases because different phases excite the same regions at different instants. This extended "on-time" of local $\mathrm{d}B/\mathrm{d}t$ leads to a higher average eddy-current loss, which explains the nearly linear increase .

At 120°, the excitation of the teeth is almost uniformly distributed over the switching period. The instantaneous hotspot intensity is comparable to the other cases, but the regions with significant eddy-current density are active for the largest fraction of time. This results in one of the highest average eddy-current losses, while the solid loss remains nearly constant with shift angle, because the overall current amplitude and conductor utilisation do not change[61].

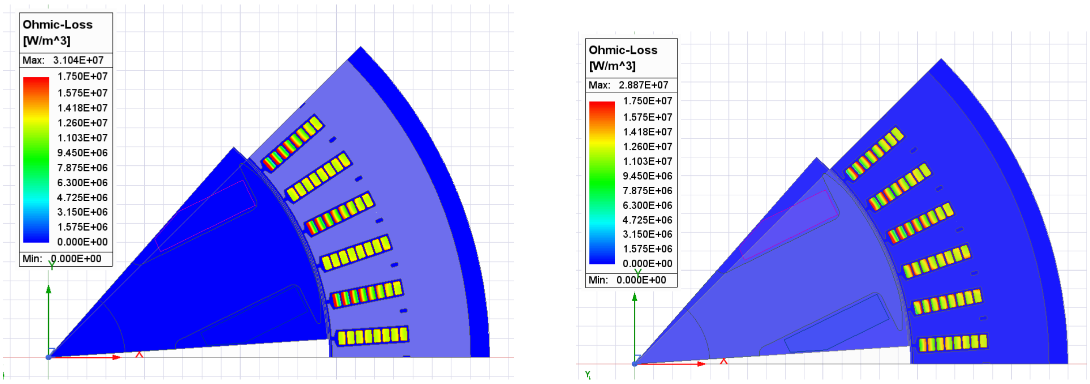

(a) Shift angle = 0° **(b)** Shift angle = 40°

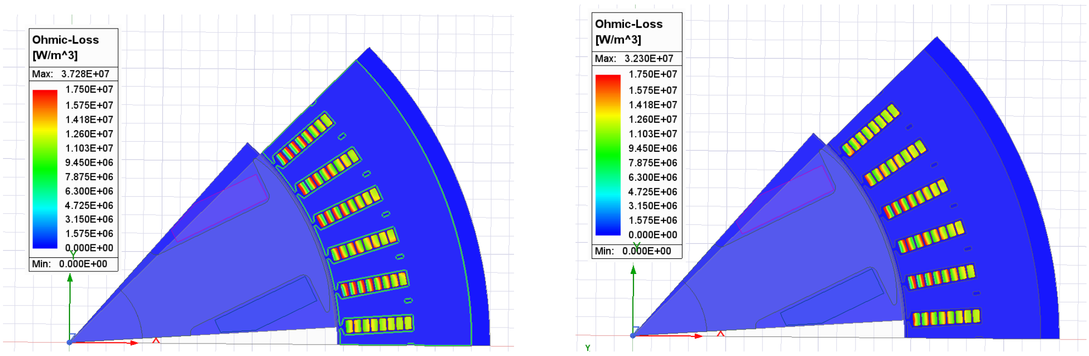

(c) Shift angle = 80° **(d)** Shift angle = 120°

Figure 4.39: Ohmic (eddy-current) loss density at different shift angles (10 kHz).

4.3.2.4 Summary

Overall, the field plots confirm that the shift angle mainly influences losses by changing the temporal distribution of ripple-induced flux rather than the peak flux density[64]. By staggering the phase ripples, higher shift angles reduce instantaneous superposition of the three phases but excite the core for a longer fraction of the switching period. This leads to a monotonic increase in the average core and eddy current losses, while the solid conductor loss remains almost insensitive to the shift angle.

4.3.3 Rotor Position

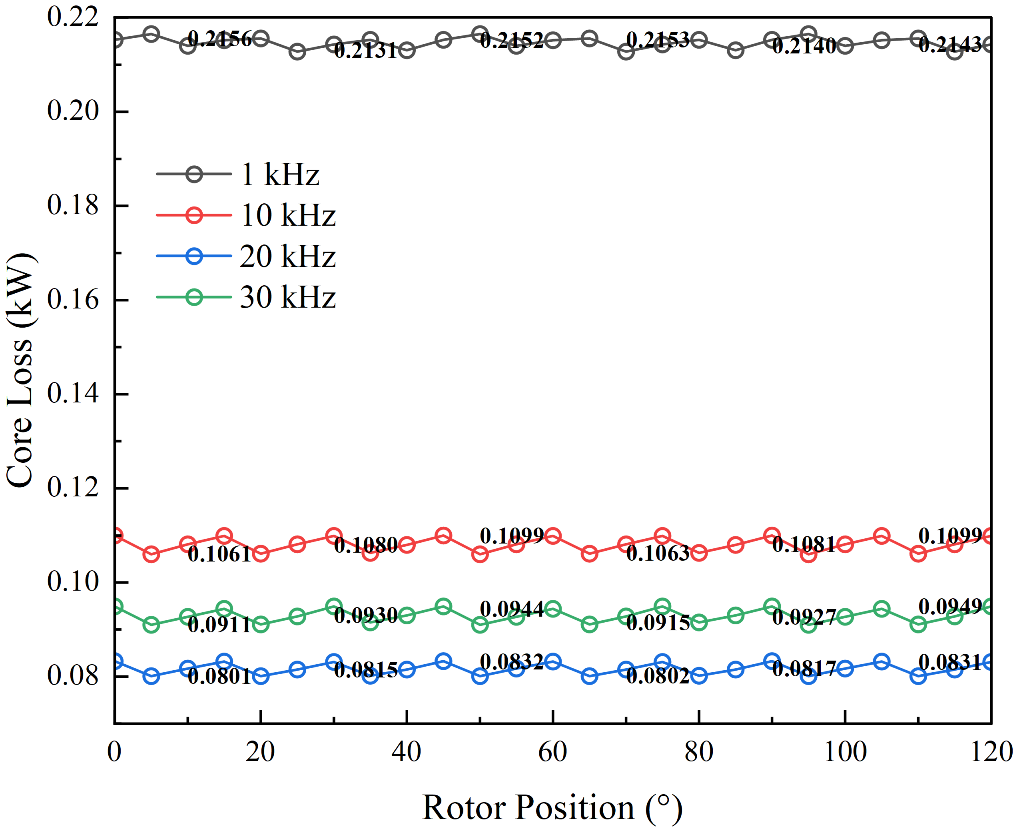

Figure 4.40: Simulink: core losses vs. rotor position

The results show that iron losses vary minimally across the entire rotor position range, displaying only slight periodic fluctuations[55]. In contrast to the negligible frequency effect observed in Simplorer simulations, the combined Simulink–Maxwell simulation reveals a clearer influence of frequency on losses. As the switching frequency increases from 1 kHz to 30 kHz, iron losses decrease significantly and the spacing between the curves becomes more consistent, indicating that high-frequency modulation effectively suppresses pulsations in the magnetic flux density[58]. This shows that current waveforms generated by Simulink more closely resemble actual operating conditions in terms of harmonic suppression and dynamic response. This enables the Maxwell model to accurately capture variation patterns in iron losses corresponding to frequency changes.

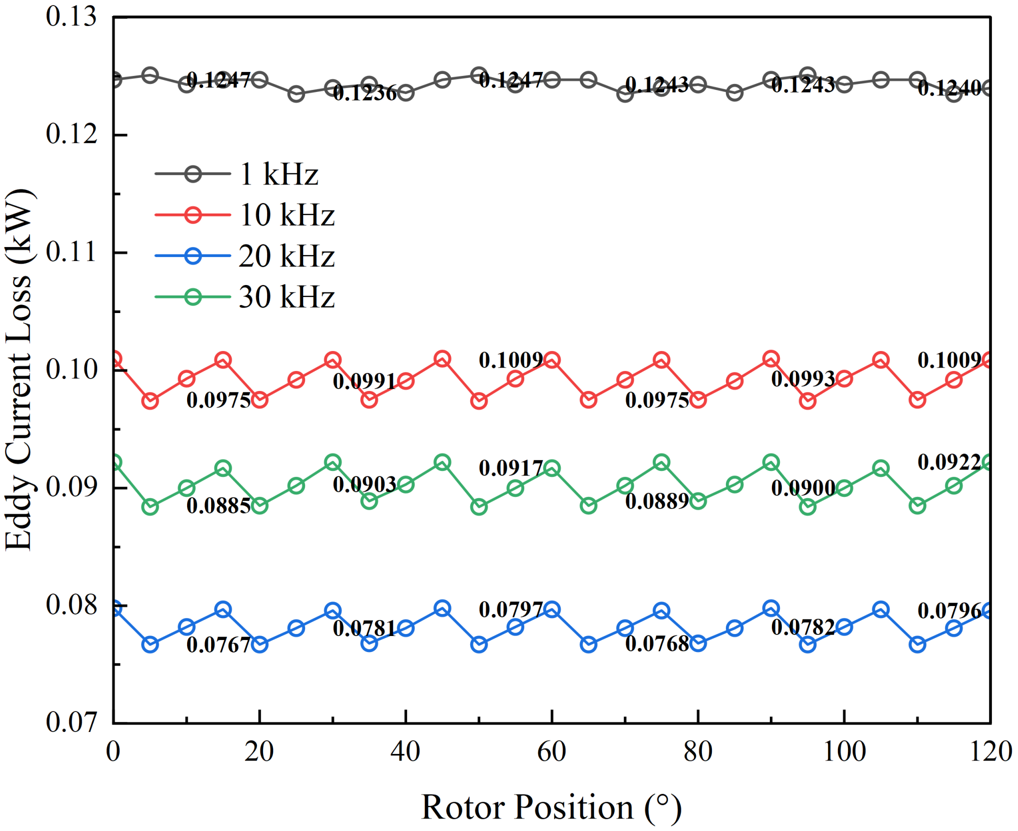

Figure 4.41: Simulink: eddy losses vs. rotor position

In Simplorer simulations, the differences in eddy current losses caused by changes in frequency were not important. However, the results of this Simulink co-simulation showed that it was possible to tell the difference between loss levels at different frequencies[47]. As the frequency goes up, eddy current losses slowly go down. This shows that high-frequency PWM lets you vary the magnetic flux more, which reduces the eddy current loops created in the conductive iron core. This result shows that the Simulink model better describes the current waveform characteristics at high frequencies. This allows Maxwell's field solution to reflect the theoretically expected relationship between frequency and loss[48].

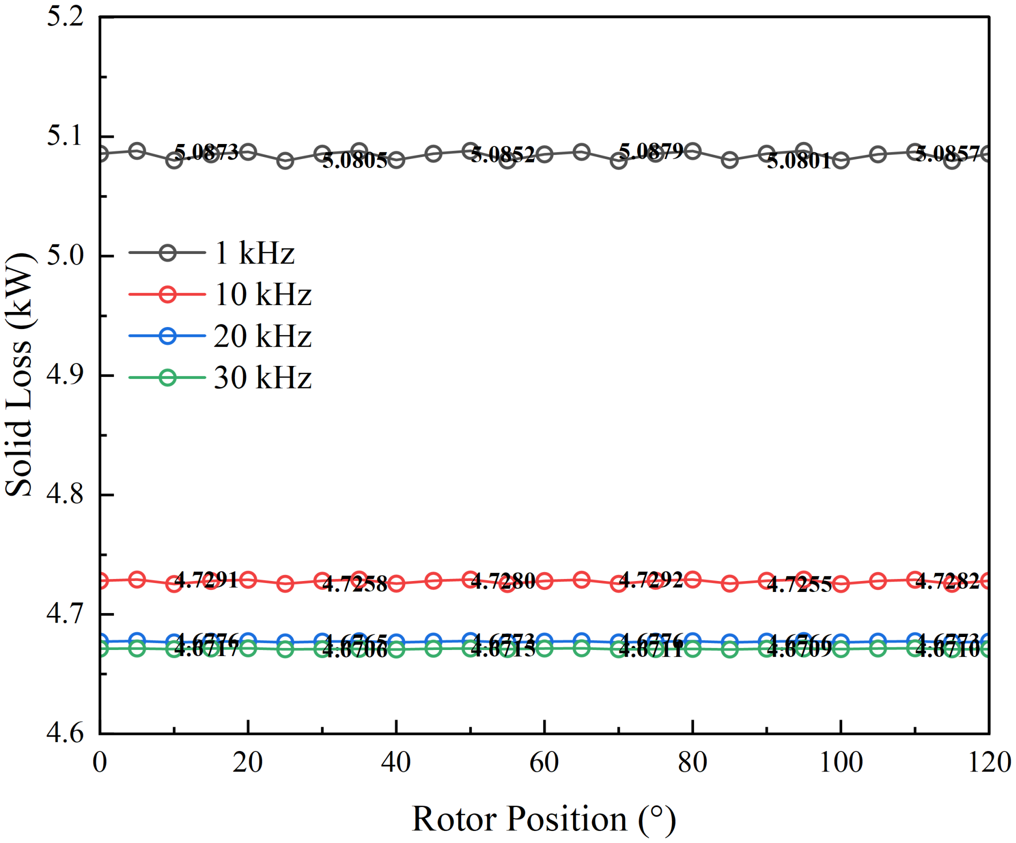

Figure 4.42: Simulink: solid losses vs. rotor position

Solid losses exhibit periodic variations across different rotor positions; however, the trend driven by frequency changes is more pronounced[65]. As the carrier frequency increases from 1 kHz to 30 kHz, solid losses show a slight overall downward trend, which is consistent with the inverse relationship between current ripple and frequency. At higher frequencies, the reduced amplitude of the current ripple decreases transient current stresses in the conductors, leading to a slight decrease in the average copper losses. In contrast to the more fluctuating results of Simplorer simulations, the Simulink–Maxwell coupled simulation exhibits a smoother, more physically plausible frequency dependence, accurately reflecting the actual impact of ripple suppression on solid losses. This further demonstrates that incorporating more precise current waveform modeling significantly improves the reliability and consistency of electromagnetic loss calculations[55].

4.3.4 Rotor Position–Dependent Field Distribution at 10 kHz

To complement the numerical results of core losses and inductances, field plots were generated at three rotor mechanical positions (3.75°, 20° and 40°) under the same 10 kHz excitation[60]. For each rotor position, the magnetic flux density magnitude, Flux-Line Distribution, and the ohmic (eddy current) loss density are shown separately. These visualizations provide further insight into how rotor alignment affects the spatial distribution of the magnetic field and the resulting high-frequency loss mechanisms.

4.3.4.1 Flux-Density Magnitude Distribution

The peak flux density B_{max} remains nearly unchanged among the three positions, indicating that the average magnetic loading is similar[61]. However, the spatial coverage of the high-flux region changes progressively. At 3.75°, the flux is most concentrated around a single tooth, producing a sharper local B^2 peak. At 20°, the high-flux region broadens and begins to spread into adjacent teeth. At 40°, the flux becomes the most uniformly distributed across multiple teeth and a larger portion of the yoke. From a volume-integral point of view, this reduction of flux concentration decreases the effective amount of highly magnetised material, which helps explain why the iron losses gradually decrease across the three sampled positions. Such concentration–spreading–reconcentration patterns naturally repeat with rotor mechanical periodicity, consistent with the periodic nature of the loss curve.

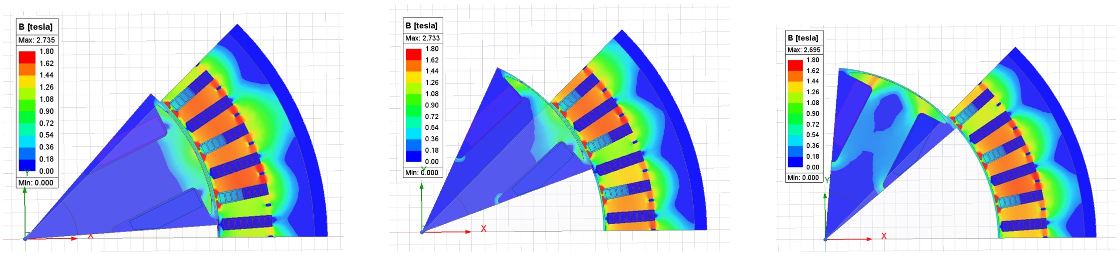

(a) 3.75° **(b)** 20° **(c)** 40°

Figure 4.43: Magnitude of magnetic flux density at rotor positions of 3.75°, 20° and 40°.

4.3.4.2 Flux-Line Distribution under Different Rotor Positions

The flux-line contours further illustrate how the magnetic path reshapes with rotor angle. At 3.75°, the flux lines form tightly packed loops predominantly linked to a single tooth, indicating a more concentrated and asymmetric magnetic path. At 20°, the flux begins to redistribute over neighbouring teeth, and the contour spacing within the teeth and yoke becomes more balanced. At 40°, the flux lines are the smoothest and most evenly spread, with less pronounced crowding near individual tooth tips. This transition from a single-tooth–dominated flux channel to a multi-tooth–shared path is a direct field-level mechanism that explains the progressively reduced core and eddy-current losses in this particular angular segment.

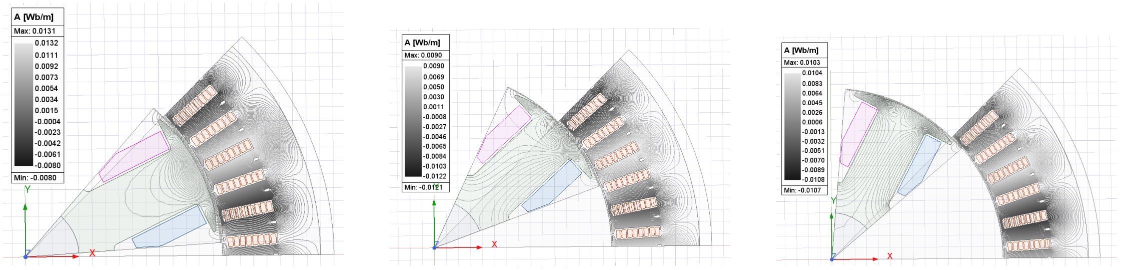

(a) 3.75° **(b)** 20° **(c)** 40°

Figure 4.44: Flux-line (A-field) distribution at rotor positions of 3.75°, 20°, and 40° under 10 kHz excitation.

4.3.4.3 Ohmic Loss Distribution

The ohmic-loss patterns also reflect this trend[32]. At 3.75°, the hotspots appear more localised along the slot edges that experience the strongest magnetic coupling. At 20°, the loss becomes more evenly distributed within the conductors, indicating a reduction in high-frequency perturbation. At 40°, the distribution is the most uniform, with no clearly dominant hotspot, suggesting that the effective AC resistance—determined by skin and proximity effects—has slightly decreased as the magnetic field becomes more evenly spread. As rotor position continues to vary, these hotspots will shift periodically around the stator according to the relative alignment between the rotor pole and stator teeth[47].

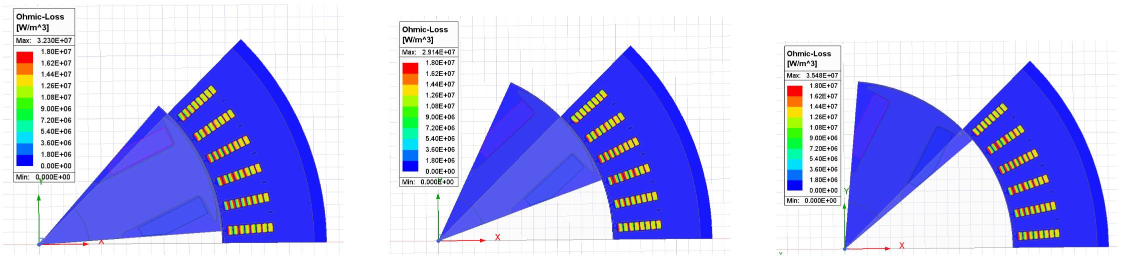

(a) 3.75° **(b)** 20° **(c)** 40°

Figure 4.45: Ohmic-loss density at rotor positions of 3.75°, 20° and 40°. Hotspots correspond to regions with strong spatial variation of flux density.

4.3.4.4 Summary

Overall, although the peak flux density remains almost unchanged, the spatial distribution of flux across the teeth and yoke becomes progressively more uniform from 3.75° to 40°[61]. This reduces both the volume of iron exposed to high B^2 levels and the severity of high-frequency perturbations within the windings. The resulting loss trend—3.75° being the highest, followed by 20° and then 40°—should therefore be understood not as a monotonic function of rotor angle but as a segment of the natural periodic variation produced by the repeated alignment and misalignment between rotor poles and stator teeth.

5

Conclusion

This work presents a comprehensive study of an integrated off-board fast charger that reuses the EESM drive system for DC/DC boost functionality. Three simulation stages were employed to evaluate the electromagnetic and system-level performance:

The system-level co-simulation between ANSYS Maxwell and Simplorer enabled real-time evaluation of the interactions between the converter, control system, and machine model. The results demonstrated that both rotor position and PWM carrier shift angle have measurable yet manageable effects on system performance. It was established that variations in rotor position caused small oscillations in inductance and torque. Furthermore, it was determined that the phase-shift angle significantly influenced current ripple and iron losses. Increasing the shift angle resulted in higher inductance, smoother current profiles, and reduced core losses, thereby enhancing overall stability and energy efficiency.

The system simulation, which was based on the Simulink software, provided further quantification of system-level performance, with a particular focus on the relationship between switching frequency and power losses. It has been demonstrated that higher switching frequencies can lead to a reduction in conduction losses due to a more uniform current flow, although there is a concomitant slight increase in switching losses. The integrated charger exhibited high efficiency across the evaluated frequency range, thereby confirming the suitability of the EESM-based topology for high-power direct current (DC) charging.

In summary, this study confirms the technical feasibility and performance stability of integrating the charging functionality into the EESM traction system. The co-simulation and system analyses demonstrate that proper control of PWM phase shift and excitation can effectively balance ripple, loss, and torque, achieving efficient fast charging without hardware redundancy.

6

Future Work

Although this thesis provides a detailed investigation of the influence of shifting angle and rotor position on the electromagnetic behavior of the studied EESM under electric vehicle charging conditions, several aspects remain open for future research.

First, the present study is conducted on a specific machine geometry with fixed pole and slot numbers. Future work may extend the proposed analysis methodology to machines with different geometric configurations and ratings, in order to evaluate the generality of the observed trends under standstill charging operation.

Second, the current analysis focuses on electromagnetic performance under static operating conditions, where the machine operates at zero speed and functions as a magnetic component during charging. Future studies could further investigate the interaction between shifting angle and high-frequency excitation characteristics, such as switching frequency, current ripple, and harmonic content, to improve loss reduction and magnetic utilization in charging mode[66].

Third, the loss evaluation in this thesis is based on electromagnetic simulation results. Future research may integrate electromagnetic–thermal co-simulation to assess temperature-dependent effects on copper loss, core loss, and material properties, which become increasingly important during prolonged charging processes[67].

In addition, experimental validation represents an important direction for future work. Prototype measurements or laboratory testing under standstill excitation could be used to verify the simulation results and to quantify modeling uncertainties related to material nonlinearity and manufacturing tolerances[68].

Finally, future work may explore control-oriented optimization strategies, where the shifting angle is selected or adapted specifically for charging operation, aiming to achieve an optimal balance between efficiency, loss minimization, and thermal performance[69].

References

[1] S. Dutta and J. Bauman, “An overview of 800 v passenger electric vehicle onboard chargers: Challenges, topologies, and control,” *IEEE Access*, vol. 12, pp. 105 850–105 864, 2024.

[2] S. Semsar, Z. Luo, S. Nie, and P. W. Lehn, “Integrated wireless charging receiver for electric vehicles with dual inverter drives,” *IEEE Transactions on Power Electronics*, vol. 39, no. 1, pp. 1802–1814, 2024.

[3] S. A. Q. Mohammed, S. S. Hakami, M. Kassas, and M. AlMuhaini, “Critical review on powertrain technologies for electric vehicles: Classification, broadly adopted topologies, and future challenges,” *IEEE Access*, vol. 13, pp. 71 755–71 777, 2024.

[4] B. M. Dinh, D. H. Linh, T. X. Hoang, and N. H. Duc, “Electromagnetic performance analysis of electrically excited and interior permanent magnet motor for electric vehicle application,” in *Proceedings of the 6th European Conference on Industrial Engineering and Operations Management.* Lisbon, Portugal: IEOM Society International, 2023.

[5] D. S. P. Kosuri, T. Boddepalli, S. Gokavalasa *et al.*, “Review on converters used in electric vehicles,” *International Journal of Research Publication and Reviews*, vol. 5, no. 1, pp. 440–454, 2024.

[6] S. Hosseinzad and A. Mirzaei, “A comprehensive review of dc-dc converters for ev applications,” *Emirates Journal for Engineering Research*, vol. 28, no. 2, pp. 6–23, 2023.

[7] B. Aljafari, T. Kareri, S. B. Thanikanti *et al.*, “Transformer-less high gain dc–dc converter design and analysis for fuel cell vehicles,” *Scientific Reports*, vol. 14, p. 19221, 2024.

[8] S. Ahmad, R. de Souza, P. Kergus *et al.*, “Robust switching control of dc-dc boost converter for ev charging stations,” in *Texas Power and Energy Conference (TPEC).* College Station, Texas, United States: IEEE, 2023.

[9] H. T. Zhang and Y. J. Zhang, “Recent advances in dc-dc converters for electric vehicles,” in *MATEC Web of Conferences*, 2023, p. 02008.

[10] Y. Cao, “Design and control of electrically excited synchronous machines for vehicle applications,” Ph.D. dissertation, Chalmers University of Technology, Gothenburg, 2022.

[11] F. Birnkammer, J. Szabados, D. Braunisch *et al.*, “Inductive electrically excited synchronous machine for electrical vehicles—design, optimization and measurement,” *Energies*, vol. 16, no. 4, p. 1657, 2023.

[12] R. Manko, M. Zagirnyak, A. Milashevski *et al.*, “Modelling of the electrically excited synchronous machine with the rotary transformer design influence,” *Energies*, vol. 15, no. 8, p. 2832, 2022.

[13] F. Cai, H. Li, and X. Zhang, “Speed sensorless control based on initial rotor position detection for eesm,” *Mathematical Problems in Engineering*, p. 2638858, 2022.

[14] S. Yadav, S. K. Mallik, and A. Mishra, “Advanced lower order harmonic torque suppression by p-pwm in high-performance scalar-controlled im drives,” *Journal of Power Electronics*, vol. 25, pp. 71–81, 2025.

[15] Y. Chen, W. Chen, Y. Wu *et al.*, “Influence of current harmonics on electromagnetic force and vibration noise of electrical machines,” in *IEEE International Conference on Electrical Machines (ICEM).* Torino, Italy: IEEE, 2024, pp. 1–6.

[16] M. Chomat, L. Schreier, and J. Bialek, “Effects of voltage unbalance and harmonics on drive systems with induction motor,” *Journal of Advanced Research in Physics*, vol. 16, no. 6, pp. 381–391, 2022.

[17] J. Tang, “Design and control of electrically excited synchronous machines for vehicle applications,” Ph.D. dissertation, Chalmers University of Technology, Gothenburg, 2021.

[18] S. H. Kim, J. H. Woo, Y. J. Kim, J. Y. Choi, and K. H. Shin, “Improved calculation of core losses of high-speed permanent magnet synchronous motor considering harmonic currents,” *AIP Advances*, vol. 14, no. 1, p. 015322, 2024.

[19] C. Zaghrini, G. Khoury, M. Fadel, R. Ghosn, and F. Khatounian, “On-line loss and global efficiency simulation tool for electric vehicles applications,” in *IECON 2021 – 47th Annual Conference of the IEEE Industrial Electronics Society.* Toronto, Canada: IEEE, 2021, pp. 1–6.

[20] V. Prakht, V. Dmitrievskii, V. Kazakbaev, E. Valeev, and V. Goman, “Traction synchronous motors with rotor field winding: A literature review,” *World Electric Vehicle Journal*, vol. 16, no. 11, p. 633, 2025.

[21] E. Roshandel, A. Mahmoudi, S. Kahourzade, and W. L. Soong, “Losses in efficiency maps of electric vehicles: An overview,” *Energies*, vol. 15, no. 3, p. 780, 2022.

[22] S. Gradev, R. Asp, G. Babro, and T. Thiringer, “Modeling and control of a dual-voltage synchronous machine,” Ph.D. dissertation, Technical University of Munich, Munich, 2021.

[23] P. Ragazzo, “Advanced modelling and design methodology for electric traction motors,” Ph.D. dissertation, Politecnico di Torino, Torino, 2024.

[24] M. J. Hsieh, “Electromagnetic modeling based life cycle assessment of rare-earth-free propulsion electric machines for vehicles,” Ph.D. dissertation, Chalmers University of Technology, Gothenburg, 2025.

[25] A. Latorre, J. Laczynski, and A. Mertens, “Adaptive determination of optimum switching frequency in sic-pwm-based motor drives: A speed-dependent core loss correction approach,” *IEEE Transactions on Power Electronics*, vol. 40, no. 5, pp. 5655–5666, 2025.

[26] M. Hernandez-Reyes, G. Elizondo-Montes, R. Brook *et al.*, “An analytical model for thermal and mechanical analysis of solid rotor induction motors op-

erating under momentary load peaks," *Engineering Science and Technology, an International Journal*, vol. 47, p. 101538, 2023.

[27] L. Boscaglia, H. S. Natesan Sugumar, N. Sharma, and Y. Liu, "Design and verification of an electrically excited synchronous machine rotor with direct oil cooling for truck applications," *IEEE Transactions on Transportation Electrification*, vol. 11, no. 1, pp. 247–259, 2025.

[28] S. Ahmed, Q. Ali, G. J. Sirewal, K. Kumar, and G. Choi, "Hybrid brushless wound-rotor synchronous machine with dual-mode operation for washing machine applications," *Machines*, vol. 13, no. 5, p. 342, 2025.

[29] S. Mesías, A. Hahn, R. de Souza *et al.*, "A bidirectional versatile buck-boost converter for electric vehicle applications," *Sensors*, vol. 21, no. 16, p. 5654, 2021.

[30] V. J. Varshini, A. H. Apsara, and R. G. Nirmala, "A novel integrated three port bidirectional dc-dc converter for energy storage systems in evs," in *2023 9th International Conference on Electrical Energy Systems (ICEES).* Chennai, India: IEEE, 2023, pp. 447–452.

[31] Y. Li, B. Li, B. Bilgin *et al.*, "Control of sic based integrated dc-dc powertrain charger for electric vehicles," in *2020 IEEE Energy Conversion Congress & Exposition (ECCE).* Detroit, MI, USA: IEEE, 2020, pp. 445–450.

[32] G. Volpe, M. Popescu, L. di Leonardo, and S. Xue, "Efficient calculation of pwm ac losses in hairpin windings for synchronous bpm machines," in *2021 IEEE Energy Conversion Congress & Exposition (ECCE).* Vancouver, BC, Canada: IEEE, 2021, pp. 4654–4660.

[33] R. Breda, G. Andrioli, S. Calligaro, and R. Petrella, "Integrated battery modular multilevel converter based drive for electrically excited and hybrid excited synchronous machines," in *2023 IEEE Energy Conversion Congress & Exposition (ECCE).* Nashville, TN, USA: IEEE, 2023, pp. 1753–1760.

[34] B. Ban and S. Stipetić, "Design and optimization of synchronous reluctance machine for actuation of electric multi-purpose vehicle power take-off," in *2020 International Symposium on Power Electronics, Electrical Drives, Automation and Motion (SPEEDAM).* Sorrento, Italy: IEEE, 2020, pp. 19–24.

[35] J. Zhou, Z. Song, X. Xiao, M. Lu, and Y. Chen, "An advanced high-speed permanent magnet synchronous machine utilizing amorphous alloy core with unequal tooth width," *IEEE Transactions on Transportation Electrification*, vol. 9, no. 4, pp. 5468–5481, 2023.

[36] S. Xue, G. Volpe, M. Popescu, and D. Staton, "Efficient calculation of temperature in high frequency high speed pm machines," in *2021 IEEE Energy Conversion Congress & Exposition (ECCE).* Vancouver, BC, Canada: IEEE, 2021, pp. 4646–4653.

[37] G. Andrioli, R. Breda, S. Calligaro, and R. Petrella, "A novel integrated multilevel converter topology for electrically excited synchronous machines," in *2024 IEEE Applied Power Electronics Conference and Exposition (APEC).* Long Beach, CA, USA: IEEE, 2024, pp. 1–8.

[38] H. B. Chung, "Pwm-based sensorless control of an electrically excited synchronous motor," Ph.D. dissertation, Technical University of Munich, Munich, 2021.

[39] B. Schmuelling, M. Steinborn, and T. Menzel, “Pwm loss analysis in electrically excited synchronous machines: implications for loss-optimal operation,” in *2025 IEEE Energy Conversion Congress & Exposition (ECCE).* Nashville, TN, USA: IEEE, 2025, pp. 1–6.

[40] Y. Zheng, Q. Wu, Q. Guo, Q. Zhu, L. Xiong, and L. Liu, “Co-simulation and modeling of pmsm based on ansys software and simulink for evs,” *World Electric Vehicle Journal*, vol. 13, no. 1, p. 4, 2022.

[41] E. Lind and S. Eriksson, “Co-simulation model combining dynamic control and fem for evaluation of pmsm drive cycle performance,” *Results in Engineering*, vol. 27, p. 106149, 2025.

[42] M. Centner and J. Endres, “Performance analysis of high-speed electric machines supplied by pwm inverters based on the harmonic modeling method,” *Energies*, vol. 14, no. 9, p. 2606, 2021.

[43] A. Balamurali, G. Feng, C. Lai, J. Tjong, and N. C. Kar, “Maximum efficiency control of permanent magnet synchronous machines for electric vehicles,” *IEEE Transactions on Transportation Electrification*, vol. 7, no. 4, pp. 2495–2505, 2021.

[44] A. Labak and N. C. Kar, “Self-excited wound rotor synchronous motors for electric vehicles,” *Journal of Advanced Transportation*, vol. 2025, pp. 1–12, 2025.

[45] M. N. F. Nashed, W. A. El-Sobky, A. F. Mohamed *et al.*, “Accurate procedure of iron core loss determination for induction motors considering supply voltage, iron core temperature, rotor parameters, and magnetizing saturation,” *Journal of Engineering*, vol. 2020, no. 10, p. 7613737, 2020.

[46] F. Zhang, G. Du, T. Wang *et al.*, “Magnetic field characteristics and stator core losses of high-speed permanent magnet synchronous motors,” *Energies*, vol. 13, no. 3, p. 535, 2020.

[47] J. S. Choi and J. Yoo, “Why state-of-the-art analytical models for eddy current losses in pm of pmsm are insufficient for variable speed motors,” *e+i Elektrotechnik und Informationstechnik*, vol. 141, no. 2, pp. 158–164, 2024.

[48] T. Long, S. Shao, P. D. Malliband *et al.*, “Analytical modelling and analysis of magnet eddy current loss in magnet-surrounded permanent magnet synchronous machine caused by stator slot effect,” *IET Electric Power Applications*, vol. 19, no. 4, pp. 1–14, 2025.

[49] Z. Wang, J. Feng, J. Shi *et al.*, “Parameter calculation and rotor structure optimization design of solid rotor induction motors,” *Machines*, vol. 12, no. 6, p. 374, 2024.

[50] X. Liu, L. Feng, Y. Wang *et al.*, “Analysis and calculation of the winding loss and rotor loss of solid rotor induction motors for flywheel energy storage system considering the influence of inverter power supply,” *Journal of Energy Storage*, vol. 88, p. 111879, 2025.

[51] M. Mirzaei and A. Binder, “Pwm-induced losses in electrical machines: an impedance-based estimation method,” *IEEE Transactions on Industry Applications*, vol. 57, no. 1, pp. 828–838, 2021.

[52] Y. Chen, Y. Shen, J. Li *et al.*, "Method of estimating initial rotor position for ipmsms using subdivided voltage vectors based on inductance variation," *Journal of Power Electronics*, vol. 20, no. 5, pp. 1195–1204, 2020.

[53] S. Zhang, J. Kang, and S. Mu, "Initial rotor position detection for permanent magnet synchronous motor based on identical width voltage pulse injection," *Proceedings of the CSEE*, vol. 40, no. 19, pp. 6085–6093, 2020.

[54] N. Feeney, K. Haran, and J. Kwon, "Real time core loss estimation for the wound rotor synchronous machine," in *SDEMPED 2023*, 2023, pp. 1–7.

[55] E. El-Kharashi and M. El-Dessouki, "Co-simulation and modeling of pmsm based on ansys software and simulink for evs," *World Electric Vehicle Journal*, vol. 13, no. 1, p. 4, 2021.

[56] H. Aygün and M. Gökdağ, "Analysis of permanent magnet synchronous motor by different control methods with ansys maxwell and simplorer co-simulation," *Balkan Journal of Electrical and Computer Engineering*, vol. 8, no. 1, pp. 21–27, 2020.

[57] M. Jiang, J. Tian, H. H. Goh *et al.*, "Experimental study on the influence of high frequency pwm harmonics on the losses of induction motor," *Energy Reports*, vol. 8, pp. 1388–1395, 2022.

[58] S. Sirimanna, T. Balachandran, and K. Haran, "A review on magnet loss analysis, validation, design considerations, and reduction strategies in permanent magnet synchronous motors," *Energies*, vol. 15, no. 17, p. 6116, 2022.

[59] E. Preci, G. Valente, A. Galassini *et al.*, "Experimental statistical method predicting ac losses in random windings and pwm effect evaluation," *IEEE Transactions on Energy Conversion*, vol. 35, no. 4, pp. 2284–2292, 2020.

[60] Z. Li, P. Wang, L. Liu *et al.*, "Loss calculation and thermal analysis of ultra-high speed permanent magnet motor," *Heliyon*, vol. 8, no. 10, p. e11059, 2022.

[61] C. Zhang, L. Chen, X. Wang *et al.*, "Loss calculation and thermal analysis for high-speed permanent magnet synchronous machines," *IEEE Access*, vol. 8, pp. 146 126–146 137, 2020.

[62] U. R. Muduli, B. Chikondra, and M. J. Akhtar, "Comparison of svpwm techniques under switching loss control for induction motor drive with lc filters," *IEEE Transactions on Industrial Electronics*, vol. 69, no. 11, pp. 11 203–11 213, 2022.

[63] A. Sikora, A. Zielonka, and M. Woźniak, "Minimization of energy losses in the bldc motor for improved control and power supply of the system under static load," *Sensors*, vol. 22, no. 3, p. 1055, 2022.

[64] D. D'Amato, J. Loncarski, V. G. Monopoli *et al.*, "Impact of pwm voltage waveforms in high-speed drives: A survey on high-frequency motor models and partial discharge phenomenon," *Energies*, vol. 15, no. 4, p. 1404, 2022.

[65] G. Liu, Y. Zhang, Y. Wang, and X. Wang, "Analysis of eddy current loss of 120-kw high-speed permanent magnet synchronous motor," *Machines*, vol. 10, no. 5, p. 346, 2022.

[66] K. Sayed, Z. M. Ali, and M. Aldhaifallah, "Phase-shift pwm-controlled dc–dc converter with secondary-side current doubler rectifier for on-board charger application," *Energies*, vol. 13, no. 9, p. 2298, 2020.

[67] K. Cai, J. Xiao, X. Su *et al.*, "Encapsulation process and dynamic characterization of sic half-bridge power module: Electro-thermal co-design and experimental validation," *Micromachines*, vol. 16, no. 7, p. 824, 2025.

[68] P. Resutík, M. Danko, and M. Praženica, "Design and implementation of a teaching model for eesm using a modified automotive starter-generator," *World Electric Vehicle Journal*, vol. 16, no. 9, p. 480, 2025.

[69] E. Balogun, E. Buechler, S. Bhela *et al.*, "Ev-ecosim: A grid-aware co-simulation platform for the design and optimization of electric vehicle charging infrastructure," arXiv preprint arXiv:2401.04705, 2024.

DEPARTMENT OF SOME SUBJECT OR TECHNOLOGY
CHALMERS UNIVERSITY OF TECHNOLOGY
Gothenburg, Sweden
www.chalmers.se

CHALMERS
UNIVERSITY OF TECHNOLOGY